TECHNISCHE UNIVERSITÄT MÜNCHEN

Advanced Technologies in Radiation Therapy

Feasibility and optimization of compact laser-driven beam lines for proton therapy: a treatment planning study

---

KERSTIN MIRIAM HOFMANN

Vollständiger Abdruck der von der Fakultät für Physik der Technischen Universität München zur Erlangung des akademischen Grades eines

Doktors der Naturwissenschaften (Dr. rer. nat.)

genehmigten Dissertation.

Vorsitzender: Univ.-Prof. Dr. Martin Zacharias
Prüfer der Dissertation: 1. Univ.-Prof. Dr. Jan J. Wilkens
2. Univ.-Prof. Dr. Franz Pfeiffer

Die Dissertation wurde am 21.05.2015 bei der Technischen Universität München eingereicht und durch die Fakultät für Physik am 01.07.2015 angenommen.

Physik-Department
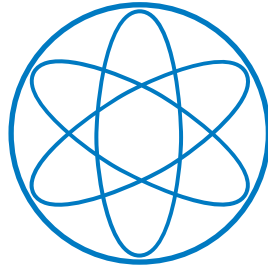
Feasibility and optimization of compact laser-driven beam lines for proton therapy: a treatment planning study

Dissertation

von

Kerstin Miriam Hofmann

- 2015 -

Technische Universität München

Feasibility and optimization of compact laser-driven beam lines for proton therapy: a treatment planning study

Purpose: Laser-acceleration of particles may offer a cost- and space-efficient alternative for future radiation therapy. Laser-driven proton beams are pulsed with very short bunch durations and each bunch contains a high number of particles with a broad energy spectrum. Due to the extremely different properties of these beams compared to conventional proton beams for radiotherapy new beam line designs have to be investigated. The presented work aims to analyze the required beam line elements and optimize the composition of a laser-driven beam line in terms of compactness and efficiency. Furthermore, the feasibility and limitations of laser-driven proton therapy are investigated. With a treatment planning study it was examined under which conditions good treatment plans can be produced and how many laser shots it would take to deliver them.

Methods: To find an optimal beam line solution, optional and mandatory beam line elements that cope with potential beam properties are discussed. Additionally, a published compact gantry design based on pulsed magnets is presented for which all producible spectra have been simulated. These were fed into a treatment planning system which can handle broad energy proton spectra. Multiple treatment plans were calculated by varying the proton number contained in the spectrum coming from the laser as well as by altering the beam width. All generated plans are evaluated in terms of dosimetric quality and required delivery time considering a 10 Hz laser system. Proton plans with only full laser shots are compared to an intensity modulation from shot to shot. Moreover, the influence on the plan quality by shot-to-shot fluctuations was investigated.

Results: An optimal beam line composition was developed relying on potential bunch properties of future laser-accelerated beams. For an optimal use of the advantages of laser-driven proton therapy, the beam line must be very compact to be contained in a small treatment head of an optical gantry. Then, heavy bending magnets can be avoided and the gantry would be very light, compact and flexible. The treatment planning study showed that high quality laser-driven proton plans can be generated and that broad spectra do not necessarily impair the dosimetric quality. However, depending on the size of the tumor the delivery of such a plan may take 16 min or longer when delivering only full laser shots. By introducing an intensity modulation from shot to shot, the treatment times could be reduced to approximately 6 min. For all cases the proton number per bunch must stay within a certain range to yield clinically relevant plan qualities since a too high proton number delivers too much dose within one shot. However, when the proton number is low, a high shot number is required to deliver the dose leading to a long treatment time. When including shot-to-shot proton number fluctuations, the impact on the dose depends on the number of laser shots per treatment plan. For many laser shots, a compensation effect could be observed. However, for plans with a lower shot number, even small fluctuations lead to unacceptable deviations in the dose distribution.

Conclusion: The final beam line and its involved elements depend strongly on the beam provided by the laser system. Therefore, these can only be found as soon as therapy relevant bunches are produced and their properties are known. Having a dedicated beam line, high quality proton plans can be generated considering some restrictions. To keep the delivery times of the proton plans comparable to conventional proton plans a device is required in the beam line to modulate the bunch intensity from shot to shot. From the laser acceleration point of view, the proton number per bunch must be kept under control as well as the reproducibility of the bunches. Complying with these restrictions, laser-driven proton therapy can be comparable to state-of-the-art proton therapy.

Contents

1

Introduction

1.1 Radiation therapy with protons

Besides chemotherapy and surgery, radiotherapy is one major modality for treating cancer patients. At present radiation therapy is mainly performed with photons (or electrons) because of the wide distribution of the associated treatment machines. These machines, called linacs (linear accelerators), fit in one room and irradiate the patient from many directions to achieve a high dose inside the tumor. Since the photon (or electron) depth dose profiles have their maximum close to the skin of the patient and decrease in depth, a high dose is deposited in the normal tissue lying in front of the tumor and, depending on the depth, the region behind the tumor is receiving an additional, significant dose as well. Compared to this, proton beams offer a beneficial dose deposition for radiotherapy of deep-seated, solid tumors. When traveling through matter, protons deposit a relatively low dose in the entrance region but close to the end of their range the dose rises to a peak, the so-called Bragg peak. Even more, the depth of this peak can be located within the tumor, i.e. the range can be adapted by varying the initial energy of the protons. Therefore, a large amount of dose can be deposited inside the tumor thus potentially sparing the surrounding organ at risk better than with photon or electron treatments [1, 2]. Additionally, protons have an increased relative biological effectiveness (RBE), resulting in more severe cell damage for the same amount of deposited dose compared to photon irradiation [3]. This RBE increase arises from the slightly increased density of ionizations along one proton track and is even more pronounced for heavier ions than protons.

Unfortunately, there are only few facilities worldwide that can offer proton (or ion) therapy because of the high costs and the large space which is needed to install and operate such a facility. The first hospital-based proton treatment center was installed in the late 1980s at the Loma Linda University Medical Center, where treatment started in 1990 [4]. To this day, only 34 centers are operating worldwide[1]. In Germany, there are four facilities treating patients, three of them are proton facilities (Rinecker Proton Therapy Center, Munich; Westdeutsches Protonenthera-

---

[1]www.klinikum.uni-heidelberg.de/Therapy-centers-in-the-world.113000.0.html

piezentrum, Essen and Charité, Berlin), and one of them can also deliver helium ions, carbon ions or oxygen ions to patients (Heidelberger Ionenstrahl-Therapiezentrum, Heidelberg). These centers are large and expensive because they require a well-shielded, relatively large proton (or ion) acceleration unit which is usually a synchrotron or a cyclotron. Furthermore, a beam line is needed to transport the particles from the accelerator to the treatment rooms and further to the patients. In the ideal case a gantry is installed at the end of the beam line to offer many degrees of freedom for the proton delivery by rotating the beam (by up to 360°) around the patient (such as the linacs for photon or electron therapy do). To realize this, large and heavy bending magnets need to be installed inside the gantry, guiding the particles of relatively high masses with sub-millimeter precision to the patient. This is essential to ensure an accurate treatment, especially for high quality intensity modulated proton therapy (IMPT) where narrow pencil beams are placed at specified spots inside the tumor [5].

Since proton therapy is available only at such a limited amount of centers, only few cancer patients can benefit from this type of radiation therapy. Therefore, researchers investigate new, smaller proton acceleration units and smaller gantry realizations to keep the costs low and to bring proton therapy to more clinical centers. However, these new machines must offer the same high quality standards (high dosimetric quality and short treatment times) as the proton facilities currently in operation. Thus, in order to bring a novel system for proton therapy into the clinics further studies need to investigate not only the feasibility to built the new facility but also whether the resulting treatment quality can be comparable to state-of-the-art proton therapy.

1.2 Novel accelerators

Accelerating protons on smaller scales (compared to conventional synchrotrons or cyclotrons) can be accomplished by different innovations. Besides laser-driven accelerators, which are described in more detail in chapter 2.1, two other novel accelerators are explained briefly in this section, constituting only two examples of new designs or realizations for medical applications. Other innovations and detailed explanations on how to reduce the accelerator sizes are given by Smith [6] and by Schippers *et al.* [7].

One straight-forward idea is to use superconducting magnets for a cyclotron. Here, higher magnetic fields are achieved which lead to smaller proton circuits and, therefore, decrease the diameter of the cyclotron from above 5 m to about 3.5 m. Such superconducting cyclotrons are utilized and installed in the commercially available treatment facilities by the company IBA (Ion Beam Applications)[2], for instance. Since the weight can be reduced as well, such compact accelerators can even be

---

[2]http://www.iba-protontherapy.com/proton-solutions

mounted directly onto the gantry as has been done with a 9 T superconducting synchrocyclotron by Still River Systems, now Mevion Medical Systems (see [8] and references within). Their single room proton beam therapy unit is currently under installation in five cancer centers or hospitals and already in clinical operation at the S. Lee Kling Proton Therapy Center at Barnes-Jewish Hospital in St. Louis, MO[3].

Another new concept is the dielectric wall accelerator, which is a linear particle accelerator with very high electric field gradients [9]. By stacking insulator and conducting material successively around an insulator wall and by using high voltage switches, an external alternating power supply can generate very high electric fields at the insulator wall of the beam pipe. These fields travel along the pipe and accelerate the injected protons with much higher accelerating gradients (about 100 MeV/m) than conventional linear accelerators (1-2 MeV/m). Therefore, 200 MeV protons would require only a 2 m acceleration wave guide which can be relatively compact and which could possibly be installed inside a treatment room. This concept, however, is still in the early research stadium and has not been installed clinically so far.

Both of the mentioned accelerators can be built much smaller than conventional synchrotron or cyclotrons. However, another promise of the novel designs is the option to use a gantry of reduced scale. This is conceivable for laser-driven accelerators. These are completely different compared to the previously mentioned accelerators since no protons need to be injected and no external electromagnetic field needs to be applied. In this approach, a high power laser is focused onto a thin target. This generates a plasma and a subsequent electric field inside and behind the target accelerating protons of the target material. So far the experimentally accelerated protons have not reached therapeutic energies of about 250 MeV. Some other challenges have to be overcome as well like increasing the repetition rate and the reproducibility of the generated proton bunches. Therefore, such systems are far away from being utilized for proton therapy. However, with developing laser technology and further investigations, this type of acceleration could represent a very small high energy proton source for therapy purposes. Even more, it offers the opportunity to simplify and reduce the size of the gantry by guiding the laser instead of the protons inside an optical gantry design.

---

[3]http://www.mevion.com/s250-map

1.3 Purpose and outline of thesis

Purpose of thesis

At the current early research stage of laser acceleration of protons, the final bunch properties of therapy-relevant proton beams can only be estimated roughly. It seems conceivable that a high number of protons with a broad energy spectrum is accelerated in bunches of ultra-short durations, leaving the target with a divergence. Therefore, the beam line for laser-driven proton therapy has to be tailored to these specific properties and conventional proton therapy beam lines cannot be utilized without modification. Hence, the first purpose of this thesis is to analyze and identify required beam line elements tailored to different possible bunch properties. This analysis aims at optimizing the whole beam line to be as compact and as simple as possible and to estimate the feasibility of an optical gantry design, where the laser is guided with mirrors to a compact particle beam line at the exit of the gantry. A laser-driven proton therapy unit with such an optical gantry may not only enable a more compact and less expensive proton facility in the future but also offer an advantage in the field of tumor motion management which this thesis points out for the first time.

The second purpose of this work focuses on the application of laser-driven beams and aims at investigating the feasibility of a theoretical compact beam line concept in terms of achievable treatment plan quality. As a worst case scenario, the laser-generated energy spectrum is assumed to be very broad and exponentially decaying from which the beam line is able to filter desired smaller parts for therapy. The study relies on real patient data and a treatment planning system designed for laser-driven protons. It examines for the first time not only the plan quality but also the associated machine parameters, such as the required laser shots and the manageable number of protons contained per bunch. In this investigation, a substantial parameter is the delivery time of one treatment fraction as this strongly restricts the bunch properties leading to acceptable dose distributions. In order to study a wide range of possibilities, the proton number per bunch is varied within the beam line from shot to shot by blocking parts of the beam (intensity modulation) or by actively changing the lateral beam size for the dose delivery. Additionally, the impact on the dose distribution from random shot-to-shot fluctuations in the proton number is examined. Therewith, the feasibility of laser-driven proton therapy can be estimated for future systems similar to the system under consideration, thus providing a feedback for further research in laser-driven acceleration of protons concerning crucial parameters and their possible ranges.

Outline of thesis

The thesis is structured as follows:

Chapter 1 introduces the reader to radiation therapy with protons and describes the need for more compact proton facilities. Novel accelerator innovations are mentioned briefly and the outline of the thesis is given.

In **chapter 2**, the theory of laser acceleration of protons is explained in more detail. New types of dose delivery schemes which are tailored to the properties of laser-driven protons are presented, and promises and challenges related to laser-driven proton therapy are discussed.

Beam line elements which have been discussed previously (cf. [10]) are analyzed and brought together in **chapter 3**. An optimal composition of these elements is investigated depending on potential proton bunch properties. Additionally, a published compact gantry design is introduced which forms the basis for the treatment planning study in chapter 5. The content of section 3.1 was already published in 2012 [11].

In **chapter 4**, the existing treatment planning system (TPS), which can calculate proton plans for broad energy spectra is presented. In the course of this thesis, an automated evaluation of treatment plans was included in the TPS which is introduced in this chapter as well. Moreover, two studies dealing with the high fluences per generated proton bunch and their divergency are summarized. These studies improved the treatment plan quality for broad lateral beams and validated the approximation of utilizing parallel beams within the TPS.

In **chapter 5** the methods and materials as well as the results of the planning studies are presented. The dosimetric qualities of the calculated plans and the required delivery times are evaluated for three different types of studies. A dose delivery with only full laser shots is compared to an intensity modulation from shot to shot. Furthermore, the impact on the dose is investigated for shots underlying proton number fluctuations. All studies aim at finding orders of magnitude for certain crucial parameters and, therewith, examine the feasibility of the system under investigation. A compact version of this chapter was submitted for publication in March 2015.

Chapter 6 discusses the feasibility of laser-driven proton therapy in general and states possible perspectives for laser-driven proton therapy in future.

In **chapter 7**, the whole thesis and its findings are summarized.

Radiation therapy with laser-driven protons

The following chapter introduces proton acceleration using lasers, describes how the produced bunches can be delivered to a patient and discusses the promises and challenges for laser-driven proton therapy. Few important laser parameters are stated which influence the acceleration, however the required laser systems are not explained in this thesis. It shall only be mentioned that current state-of-the-art laser systems operate at intensities of approximately $10^{21} \, \text{W/cm}^2$ and can yield energies of around 10 J per pulse in about 35 fs. These lasers already demonstrated the possibility of ion acceleration (see chapter 2.1) but must possibly be further improved to be suitable for proton therapy.

2.1 Proton acceleration

Acceleration of protons or ions can be performed when a high intense laser impinges upon a thin solid target. Since the first experiments in 2000 (e.g. [12, 13]) different types of acceleration scenarios have been studied (some only in theory others also experimentally), however all regimes rely on the relatively inefficient "indirect ion acceleration". This means, the laser energy is transferred to the electrons in the target which subsequently accelerate the ions via charge separation. A "direct ion acceleration" would be much more efficient in terms of energy conversion but is theoretically only possible for intensities above $10^{24} \, \text{W/cm}^2$. In such a "direct acceleration" the ions would be accelerated by the laser and not by the charge separation. The accelerated ions are mainly protons due to their high charge-to-mass ratio, even if metallic foils are utilized. In these cases, the protons originate from contaminant layers of water vapor or hydrocarbons.

In this section, the physical processes contributing to laser proton acceleration are mentioned and two important acceleration regimes are explained, namely target normal sheath acceleration (TNSA) and radiation pressure acceleration (RPA). Detailed explanations can be found in the reviews by Macchi *et al.*, Ledingham *et al.* and Borghesi [14, 15, 16] and in the PhD theses by Schollmeier and Henig [17, 18], where most of the following content was taken from. Note that there is no clear line between two acceleration regimes and nearly all processes are present in every regime, just to a different extend. This may clarify some findings in literature. An-

other issue which may cause confusion is the nomenclature concerning this research field which hopefully may be cleared up here as well.

Plasma generation. When an intense laser hits a target, either the prepulse arriving some nanoseconds before the main laser pulse, or the rising edge of the main pulse produces a plasma at the surface of the target. Such a plasma is formed via multiphoton ionization, tunneling ionization or similar processes releasing the electrons from the atoms. In most cases, the plasma is overdense, i.e. the electron density is larger than the critical plasma density and the laser cannot penetrate the plasma (nor the target). Therefore, the energy of the laser has to be converted into kinetic energy of the electrons in the thin region at the plasma boundary by laser-plasma interactions.

Electron heating. The laser is exciting the electrons of the plasma causing their oscillation due to the Lorentz force:

$$\overrightarrow{F}_{Lorentz} = -e[\overrightarrow{E} + (\overrightarrow{v} \times \overrightarrow{B})]$$

In this formula, $\overrightarrow{E}$ and $\overrightarrow{B}$ represent the electric and magnetic field of the laser pulse and $\overrightarrow{v}$ symbolizes the velocity of the electrons. However, this oscillation does not lead to a net energy gain after the laser pulse has passed. The so called heating of the electrons occurs via many different physical processes depending on the laser intensity and the incidence of the laser. For lower intensities ($< 10^{15} \, \text{W/cm}^2$) an important process is the resonance absorption, however, for high intensities, the Brunel heating or the jxB heating gets more important. For laser intensities larger than $10^{18} \, \text{W/cm}^2$ (currently utilized lasers), this jxB, or vxB heating is the dominant process since the electron velocities become relativistic. For lower intensities, the Lorentz force can be approximated by the electric part only, but for relativistic conditions the magnetic component (vxB) plays an important role. The electrons do not only oscillate in the electromagnetic field, but are pushed predominantly in z-direction (for $\overrightarrow{e_z}$ being normal to the target surface). This electron driving process is called magnetic Lorentz force or rather ponderomotive force in literature, which is identical to the jxB or vxB heating. The non-relativistic ponderomotive force can be calculated from the Lorentz force by using a Taylor expansion leading to

$$\overrightarrow{F}_{ponderomotive} = -\frac{e^2}{4m_e w_L^2} \overrightarrow{\nabla} E^2. \tag{2.1}$$

In this, ω_L is the laser angular frequency and E the electric field of the laser. The relativistic ponderomotive force is more complex and needs to be solved numerically. Equation 2.1 indicates that the electron acceleration points to lower intensities ($I \sim E^2$), i.e. away from the central axis for bell-shaped laser profiles.
In general, all previously mentioned heating mechanisms are present in the plasma simultaneously and give rise to a thermal electron energy spectrum with a maximum electron temperature as high as the ponderomotive potential energy:

$$\Phi_{ponderomotive} = m_e c^2 (\overline{\gamma} - 1) \tag{2.2}$$

with the cycle-averaged relativistic Lorentz factor $\overline{\gamma} = \sqrt{1 + a_0^2/2}$ and the dimensionless laser field amplitude $a_0 = \sqrt{\frac{I_L[W/cm^2]\lambda_L^2[\mu m^2]}{1.37 \cdot 10^{18} W \mu m^2/cm^2}}$.

$$\Rightarrow k_B \cdot T_{e,pond} \approx 0.511 MeV \cdot (\sqrt{1 + a_0^2/2} - 1)$$

$$\hat{=} \quad 0.1 - 10 MeV \text{ for } I_L = 10^{18} - 10^{21} W/cm^2$$

Electron transport through the target and charge separation. Since the velocity of the electrons is very high, the cross section for collisions is small. Therefore, the electrons can travel through the thin target (typically micrometer or less) with nearly no target interaction. On the contrary, the ions of the target have not gained energy from the laser and, hence, remain at their initial locations. The electrons penetrating the foil build up a charge separation with the remaining positive ions leading to strong electro-static fields which in turn accelerate target protons (ions). Since the charge separation and, hence, the electro-static field only persists as long as the electromagnetic field of the laser, the protons are accelerated in bunches of extremely short durations ($\sim 1 ns$). The amount of protons contained in one bunch depends (amongst other things) on the accelerating field produced within the target and is therefore not assessable. Currently, it is expected that very high fluences are generated per bunch.

Certainly, the generated bunch not only consists of protons but also of the co-moving electrons and heavier ions (depending on the target composition). These can be distinguished by a simple Thomson spectrometer, for instance.

TNSA

When utilizing targets of a few micrometer and laser intensities in the order of 10^{18}-10^{21} W/cm^2 the electrons are accelerated predominantly as explained above. They travel through the target and exit the target at the rear side. (Front side acceleration is also possible but even less efficient.) There, an electron cloud or sheath is accumulated which builds up a quasi-static charge separation field (in the order of $\sim$TV/m) pulling protons from the target into the vacuum and accelerating them in normal direction. This so called target normal sheath acceleration is depicted in figure 2.1 and explained in detail by Wilks *et al.* and Tajima *et al.* [19, 20].
The first experiments carried out in the field of laser-accelerated protons were performed in the TNSA regime and nowadays it is the most studied and best understood regime. The produced proton bunches typically have broad energy spectra and large divergence. The broadness of the energy spectrum originates from the thermal energy distribution of the hot electrons and the non-uniform acceleration of the protons. Since the sheath at the target's rear side is bell-shaped and accumulates in time, the acceleration time and strength varies for each proton leading to a broad energy distribution within the bunch. This shape of the sheath and the
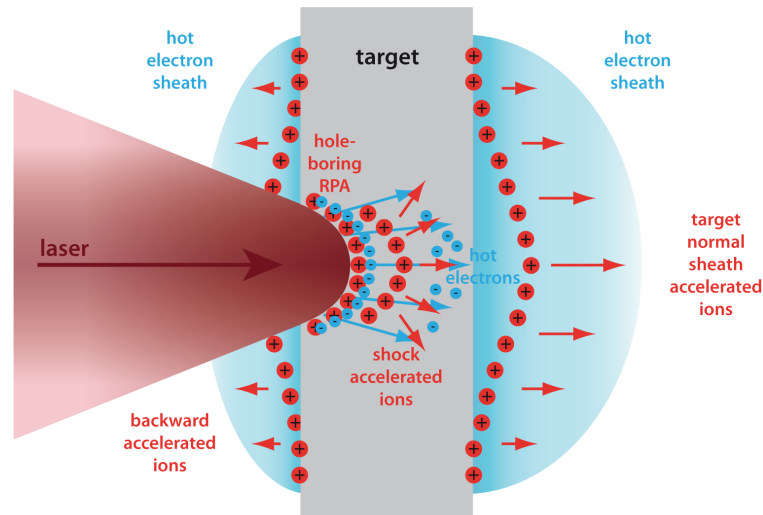
Figure 2.1: Schematic overview of ion acceleration using an impinging laser (taken from [18]). Hot electrons are produced within the target and exit the rear (and the front) side. This electron sheath accelerates the ions in the target normal sheath (TNSA) acceleration regime. The laser may also push an electron layer and bore a hole into the target which can accelerate ions to higher energies in the hole boring radiation pressure acceleration regime (RPA).

fact that the acceleration takes place normal to the sheath surface explains the large emission angles (half angles of up to 10°-20°) for the TNSA experiments. Another issue are the currently low cut-off energies and the few protons close to these energies. For instance, 58 MeV have been reported for a TNSA measurement [13] which represents the order of magnitude of the currently achieved cut-off energies. However, simulations predict a scaling of the proton energy with the square root of the laser intensity ($E \sim \sqrt{I_L \cdot \lambda_L^2}$, [21]) since the electron temperature scales with the ponderomotive potential (see equation 2.2). Thus, it is expected to create higher energies using TNSA in future.

RPA

For much higher intensities ($>10^{23}\,\mathrm{W/cm^2}$) and a laser pulse with high contrast the radiation pressure becomes relevant and dominates over the previously mentioned electron heating mechanisms. When utilizing circular polarized light which suppresses some electron heating processes, lower laser intensities can cause RPA acceleration as well [22].

For targets with thicknesses of some micrometer, the laser, i.e. the radiation pressure, pushes a layer of electrons like a snow plow and drills a channel through the plasma (sketched in figure 2.1). Therefore, this sub-group of RPA is referred to as hole boring regime (but also as laser piston regime). The electron layer pulls ions

behind it due to the charge separation leading to a shock traveling through the target. Cold ions can be reflected by that shock and reach high energies (up to twice the velocity of the propagating shock).

When the target is much thinner (in the order of nanometer or less) the same scenario takes place, however, the laser can penetrate the whole target, i.e. the hole which is bored exceeds the target. Therefore, all electrons and all ions are accelerated coherently or rather the target is accelerated as a whole. This regime is referred to as light-sail. The laser can accelerate the ions to much higher energies since they are not shielded in a plasma background anymore.

Simulations of this regime have already been carried out in 2004 by Esirkepov *et al.* [23] promising narrower energy spectra centered on higher energies with lower divergence. Due to the lack (or reduced amount) of hot electrons and the coherent acceleration of the whole foil, the energy spectra in RPA are theoretically even quasi-monoenergetic. Experimentally, it is not easy to maintain the integrity of the target until the high intensity pulse can interact with it and therefore only few experiments have been carried out in the RPA regime to confirm the simulations [24, 25].

Since RPA has not demonstrated to yield high and quasi-monoenergetic energies yet, many other investigations are performed aiming mostly for higher proton energies. Examples are mass-limited targets to concentrate the hot electron population to very small volumes or gas targets to explore laser interactions with underdense plasmas. The highest proton energy ever reached via laser-acceleration was 160 MeV published by Hegelich *et al.* [26]. This experiment was performed in the break-out afterburner regime (BOA) where the target becomes relativistically transparent so that the laser can interact with the whole target utilizing moderate laser intensities [27]. BOA can be seen as a hybrid mechanism between TNSA and RPA.

2.2 Dose delivery methods

In clinical routine, two dose delivery methods are utilized in the operating proton facilities, namely passive scattering or active scanning.

In figure 2.2 the treatment head, or nozzle, for passive scattering is shown schematically. When a monoenergetic beam approaches from the left, the energy is decreased and spread by a range-shifter modulation wheel. This modulation is necessary since the very narrow Bragg peak must be enlarged to form a so called spread-out Bragg peak (SOBP) bringing a broader dose profile into the target. Depending on the material thickness and the rotation velocity of the wheel, a patient specific width of the SOBP can be obtained. Subsequently, the beam is spread by two scatterers to broaden the beam laterally and enable a homogeneous fluence profile (shown at the bottom of figure 2.2). A collimator adapts the beam laterally to the target, whereas a compensator conforms the dose to the distal edge of the target. Obviously these
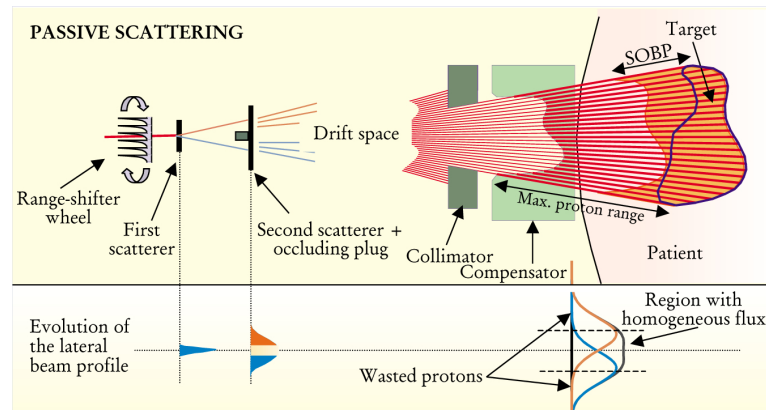
Figure 2.2: Principle of passive scattering technique. A range-shifter wheel performs a spread-out Bragg peak (SOBP) before the beam is broadened by two scatterers. With a collimator and a compensator the high dose region can be conformed laterally and distally to the target. Due to the fixed width of the SOBP the proximal edge is not irradiated conformally. This sketch is taken from Goitein *et al.* [28].

devices depend strongly on the tumor shape, and therefore, need to be produced for each patient individually.

To avoid blocking of protons with the collimator and especially to conform the dose also to the proximal edge of the tumor, active scanning techniques are favorable. This delivery requires changing of the proton energy performed by the accelerator, and consists of a very simple nozzle design as sketched in figure 2.3. This beam of variable and narrow energy is deflected by sweeping magnets to predefined spots inside the target, where the dose is deposited in and restricted to a very small area (Bragg peak). The single spots can be weighted individually, i.e. any amount of protons can be delivered to any spot, which corresponds to an intensity modulated proton therapy (IMPT).

When dealing with laser-accelerated beams there are, in principle, more options than the two mentioned above [10, 11]. In figure 2.4 different dose delivery methods are sketched for one beam direction and a water equivalent patient. In each sketch areas are pointed out, so called clusters, in the tumor which are irradiated at once, i.e. with one single proton bunch.

Figure 2.4a) illustrates the spot-based delivery for laser-driven protons which is similar to the explained active scanning technique for conventional accelerators. The intensity modulation of the spots is performed by delivering any desired number of laser shots to one spot. This allows for the most flexible dose delivery with many degrees of freedom.
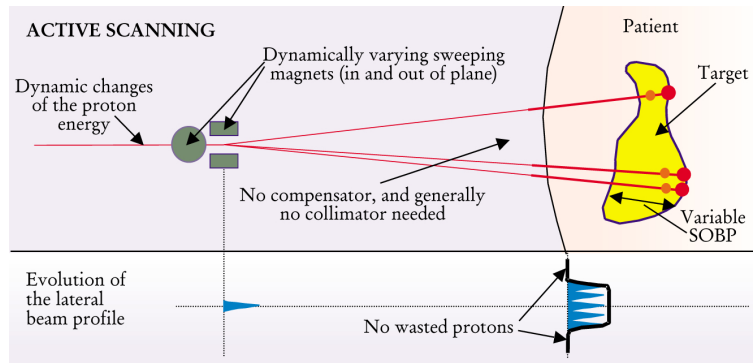
Figure 2.3: Principle of active scanning technique. Two orthogonally arranged pairs of magnets can scan the narrow Bragg peak over the whole target to deliver any desired amount of dose to predefined spots within the target. This sketch is taken from Goitein *et al.* [28].

Figure 2.4b) represents the lateral-layer-based delivery. This is a reasonable, efficient delivery if the fluence per bunch is very high or if the number of shots is limited due to a small repetition rate of the whole system. In this scheme, the quasi-monoenergetic beam is spread laterally to cover a part of, or even a whole layer in the tumor. This increases the irradiated area within the tumor which spreads the fluence and may decrease the required laser shots.

In contrast to this, the axial-layer-based delivery is shown in figure 2.4c). This concept arose from the fact that laser-accelerated beams occur with a broad spectrum anyway. Thus, the spectrum can be used without any modifications or can be modulated in any user-defined way, for example by producing a SOBP. In this method, the narrow beam with the broad spectrum is scanned over the target and delivers a certain dose in a cluster of arbitrary axial length.

Another conceivable delivery method would be a combination of both clustering methods, called the partial-volume-based delivery, depicted in figure 2.4d). This method combines the two layer-based clustering schemes, i.e. broad energy spectra are, in addition, spread laterally. This may lead to even faster treatments due to the big cluster sizes.

Going from partial volumes to the whole target volume, it is also possible to irradiate the whole tumor within each laser shot. This technique is very similar to the conventional passive scattering method and illustrated in figure 2.4e) for the sake of completeness.

All of these techniques, except of the target-volume-based method allow a superposition of partial volumes or partial layers with different numbers of particles. Therewith, one can achieve an intensity modulation offering the opportunity to perform laser-driven intensity modulated proton therapy.
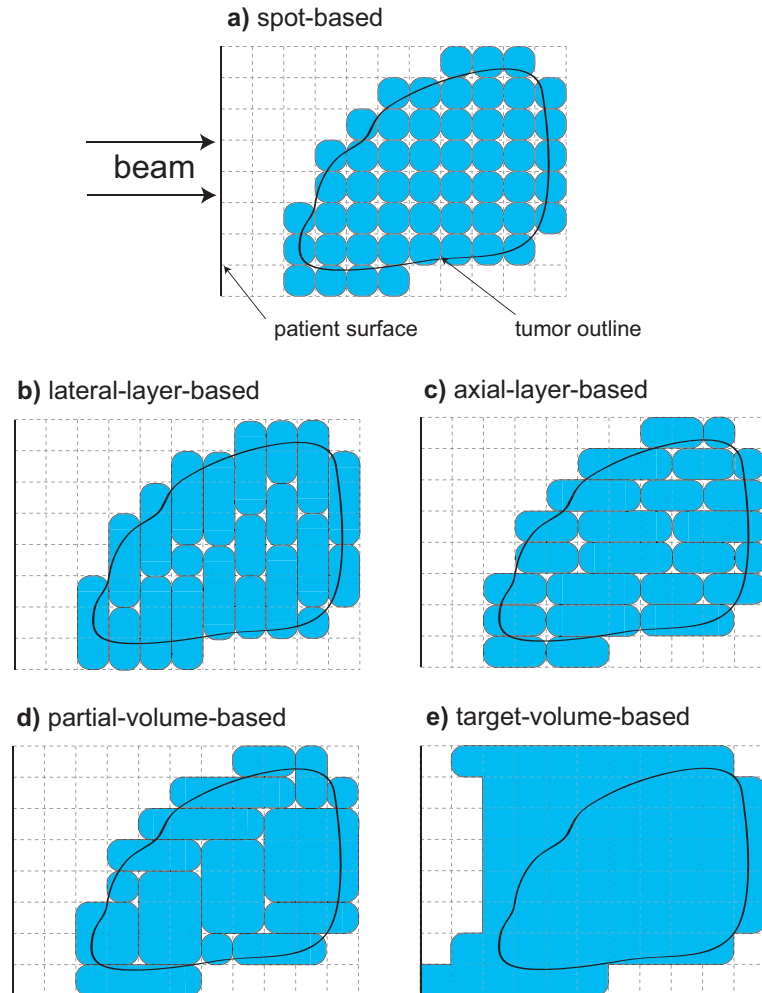
Figure 2.4: Sketch of five different dose delivery schemes for laser-driven protons [10]. The delivery schemes are shown for one beam direction and a water equivalent patient. Each enclosed area (cluster) is irradiated simultaneously within one laser shot. Going from a)-e) the bunch is spread over a wider area to irradiate a larger portion of the target. Intensity modulated proton therapy can be performed by superimposing any cluster sizes with different amounts of particles for the scenarios a)-d).

Note, that figure 2.4 illustrates the clusters for a water equivalent patient. When dealing with variable electron densities inside the patient one lateral layer/cluster irradiated with one energy not necessarily connects spots in the same physiological depth and therefore not forms a straight line as in figure 2.4b). Instead, spots of the same water equivalent depth are clustered which may have different physiological depths and deforms the layer. This of course holds also for the partial-volume-based delivery where the whole volume may be distorted.

2.3 Promises and challenges

Despite the extremely different properties of laser-driven protons compared to conventionally accelerated protons the idea to use laser proton acceleration for cancer treatment is intensively discussed since 2002 [29, 30] and is still an ongoing topic of interest. In the last decade, the three main pillars of laser-driven proton therapy were reduced size, reduced costs and increased dose rates. These promises and hopes are discussed here as well as the main challenges and limitations which occur in comparison with the state-of-the-art technology (cf. Linz *et al.* [31]). These challenges originate either from the laser-target-system itself, from the nowadays experimentally possible energy spectra of the bunches or from the required beam line guiding the proton beam to the patient.

Promises

The greatest promise of laser-accelerated proton therapy is the small size and, therefore, cost efficient facility for cancer treatment with protons or ions. Currently installed ion therapy facilities are of large size like the Heidelberg Ion Therapy Facility, shown in figure 2.5 and, hence, are very expensive (in the order of 95M Euro [32]). Especially the accelerating part takes a lot of space as a synchrotron or cyclotron needs to be installed close to the therapy room(s). Figure 2.5 shows the world wide first ion gantry which is able to rotate, for instance carbon or oxygen ions, around a fixed room isocenter. This gantry is certainly larger (diameter: 13 m [33]) than a proton gantry (diameter PSI gantry 2: 7.5 m [34]), however, even these "small" proton gantries are still far larger than photon gantries (diameter: $\sim$2 m). Having a table top laser within the treatment room or even mounted on the gantry could one day decrease the size of such a facility significantly and bring proton therapy gantries or even gantries for higher charged particles into conventional photon linac bunkers. As a result, these facilities might become less expensive (one order of magnitude less, i.e. 10M Euro [35]) and proton or ion therapy can be offered to more patients. However, it is important to mention that the state-of-the-art technology is far away from this promise. Currently utilized pumped laser systems are not that compact and are based on very sensitive optical components which are moreover quite expensive. Therefore, the advantage of the size and the costs still needs to be demonstrated in future.

Figure 2.5: Design of the Heidelberg Ion Therapy Facility (HIT) including the synchrotron, the beam line, two fixed beam line irradiation rooms and the gantry irradiation room. The HIT-Gantry can guide heavy ions up to oxygen and rotate around 360° for beam delivery. (Taken from `www.klinikum.uni-heidelberg.de/Das-HIT.117970.0.html`.)

The next promise is the increased dose rate due to the extremely short bunch lengths of some nanoseconds. For instance, Bin *et al.* measured a maximum dose of 7 Gy per shot which corresponds to a peak dose rate of $7 \cdot 10^9$ Gy/s [36]. However, different cell experiments demonstrated a relative biological effectiveness (RBE) similar to the one of conventional protons [36, 37, 38]. Therefore, the high dose rates do not seem to improve DNA damage at least in the cell lines.

Another promise highlighted in this thesis is barely discussed in literature. Due to the possibility to deliver high doses in short times laser-driven proton therapy provides advantages in future adaptive radiotherapy treatments like gating or tumor tracking. These motion adapting techniques are under investigation in conventional particle therapy as well, since target movements introduce high uncertainties in external radiotherapy [39]. In a gating scenario, high doses can be delivered in one single gating period. This could shorten the delivery time for one gated treatment fraction noticeable because only few or even only one gating period is needed to deliver the complete desired dose. For tumor tracking these advantages persist. One could even argue that almost no tracking is needed when the whole dose is delivered in a time in which the tumor nearly does not move [11].
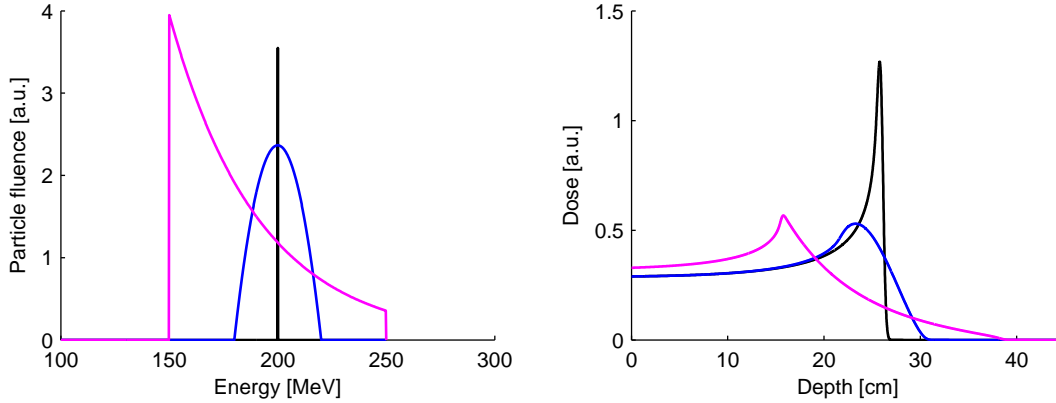
Figure 2.6: Comparison of three different proton energy spectra and their corresponding depth dose distribution in water. Monoenergetic protons (black) result in the so called Bragg Peak.

Challenges

The challenges that remain to utilize laser acceleration of protons for radiotherapy depend strongly on the laser and the target. The two first important issues besides the generated proton bunches and their guidance to the patient are the currently low reproducibility and the low repetition rate of the laser-target-system.

The poor reproducibility originates from the difficulty to bring the same laser pulse on exactly the same target composition in each single shot. Even if the laser could be focused perfectly and the time structure of the pulse would be the same in every shot (which is tough to fulfill) the laser energy fluctuates from shot to shot. Furthermore, the target components, especially at the surface are not the same for each shot (because mostly the target has to be changed after one shot). These fluctuations result in slightly different interactions happening inside the target leading to different output spectra of the single bunches. The repetition rate in which the bunches are produced depends strongly on the stability of the pump laser. The high power laser system has to be re-charged by the pump laser to be fired again. This leads to repetition rates of some shots per hour up to about 1 Hz nowadays. However in clinical routine, repetition rates of about 10 Hz are probably required to keep the treatment times acceptable for the patients (see chapter 5). Both issues can hopefully be addressed with new generations of lasers in future.

Since quasi-monoenergetic proton spectra are still in the early research stadium, TNSA is utilized as a reference also because it provides the best reproducible proton spectra at the moment. However, this requires the cut-off energies to be raised to at least 250 MeV which corresponds to a range of about 40 cm in water allowing even the treatment of deep-seated tumors. Besides the maximum energy, the broad

energy spectrum of the proton bunches is a big challenge. As illustrated in figure 2.6 an exponentially decaying energy spectrum yields a very broad dose deposition in water which barely resembles a perfect Bragg peak (as for monoenergetic protons). With such a dose distribution the good quality of proton therapy treatment plans is imperiled as a conformal dose deposition inside the target is nearly impossible. Figure 2.6 shows as well that a broad parabolic energy spectrum also leads to a smeared Bragg peak, however with a much better depth dose distribution than the exponentially decaying spectrum. With such a moderate broad spectrum and the previously introduced new dose delivery schemes (chapter 2.2) developed for broader spectra good quality proton therapy might be possible, which still has to be proofed (see chapter 5) and leads to the last big challenge: A beam line being able to handle laser-driven protons.

The required beam lines must be able to collect, modify and transport the beam to the patient. Certainly, the beam line design depends strongly on the final spectrum properties but constitutes a challenge for all currently conceivable scenarios. Due to the broad energy spectra with large divergence the guidance of the beam is completely different compared to conventional proton beam lines. The bunch must be captured at the entrance of the beam line and be re-focused during the transport repeatedly. As stated above the very broad energy spectra have to be modified in such a way that a smaller part of the whole initial spectrum exits the beam line. The high fluence represents another problem. For a long time the major opinion was that too few protons are contained in one bunch so that one therapy fraction would need many laser shots. Nowadays there exist some calculations on basic estimations of how many protons are required and how many are contained in one bunch but no real patient based or treatment planning based studies were performed up to now (cf. [20, 31, 40]). However, it is more likely that too many protons are produced per bunch such that the beam line must be able to reduce the amount of protons. The filtering of protons with the desired energy and the reduction of protons to keep the fluence per shot acceptable require a good shielding inside the beam line. In this context, TNSA represents a worst case scenario where an extremely large part of the whole bunch needs to be dumped for every laser shot. The produced secondary radiation must be shielded such that the patient does not get an extra exposure of radiation. Additionally, the high fluence arriving in very short times demands special beam diagnostics as discussed by Bolton *et al.* [41]. Such a beam monitoring is especially needed if the reproducibility of the bunches is low. A detailed discussion about the required beam line elements as well as two possible designs are given in chapter 3. However, the poor reproducibility and the low repetition rate cannot be intercepted by the beam line but must be improved at the stage of the laser. The orders of required reproducibilities and repetition rates are explored in chapter 5.

3

Beam line designs for laser-driven proton therapy

Since the first proposal to use laser-accelerated protons for therapy, very flexible optical gantry designs have been published which guide the laser light inside the gantry to the target very close to the patient [29, 35]. However, Ma *et al.* were the first to include a "beam selection system" into the treatment head preparing the beam for treatment. Such a beam selection is essential to utilize laser-driven protons for radiotherapy because the beam has to be modified while it is transported to the patient. The most important modification is the selection of desired parts of the energy spectrum from the anticipated non-monoenergetic produced spectrum at the target. Nearly all proposed energy selection systems rely on a spectrometer-like system consisting of four static magnetic dipole fields [42, 43]. Only few other systems focus on different approaches, like quadrupoles with a subsequent collimator or a laser triggered micro-lens [44]. The spectrometer-like energy selection also referred to as chicane is easy to build and control, however, secondary radiation is produced when dumping the undesired part of the proton bunches. Depending on the incoming energy spectrum, this can make the beam line very inefficient and heavy due to the required shielding material.

In this chapter two beam line concepts are presented. While the first one is using the chicane selection system with static magnetic fields, the second one utilizes pulsed magnetic quadrupole fields for energy selection. For the first design a detailed analysis was performed to optimize the composition of the beam line tailored to some potential spectrum properties. The second part introduces a published beam line composition for which a particle transport simulation was performed. Both concepts were not meant to compete with each other but rather offer two different possibilities for future laser-driven proton therapy, both with their own advantages. The final design at the end strongly depends on the final produced proton spectrum at the target, anyway.
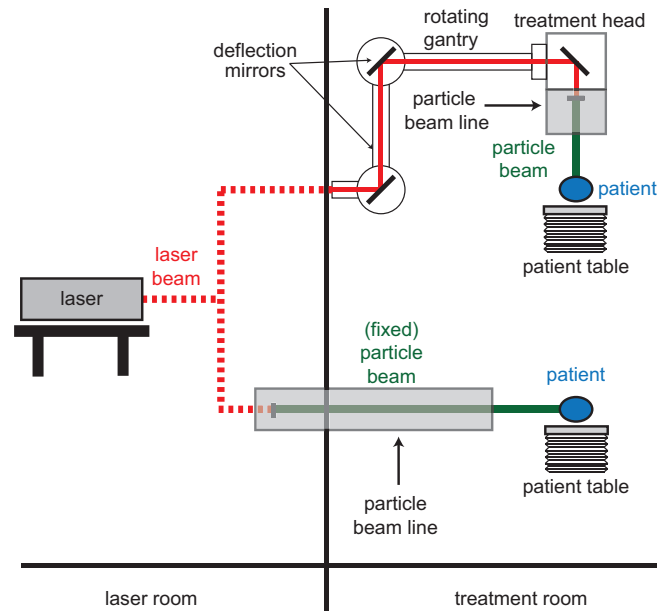
Figure 3.1: General layout of two laser-driven particle therapy units. The upper beam line shows a compact optical gantry guiding the laser beam to the treatment head where all required beam line elements are stored in a compact particle beam line. The lower one is a fixed horizontal beam line which offers more space for the beam line elements. Both beam lines are fed by one table top laser in the adjacent room.

3.1 Beam lines based on static magnetic fields

The main advantage of laser-driven proton facilities is their (potential) compactness. Figure 3.1 shows an exemplary sketch of two different treatment scenarios operating with a table top laser. One design delivers the treatment with a fixed horizontal beam line, whereas the other uses a flexible optical gantry. This figure could as well be interpreted as a two-room facility with one gantry and one fixed beam treatment room. In this scenario, the laser is installed in the adjacent room and the beam is transported to the room where the patient is ready for treatment, similar to a conventional multi-room proton facility. One could also imagine the laser to be installed within the treatment room or even mounted on the gantry for a single-room facility and a compact laser.

 Figure 3.1 does not only illustrate the compactness of the facility, but also the idea of a very compact and flexible optical gantry approach. In this gantry, the laser is deflected by mirrors and guided to the treatment head at the very end of the gantry. This concept avoids heavy bending magnets to deflect the protons inside the gantry, but demands a very compact particle beam line which must fit into the treatment head. Compared to a gantry, a fixed beam line design offers more space for all required beam line elements, however is limited by the degrees of freedom concerning the beam angles for delivery.

The required space and whether a compact beam line can be installed within the treatment head of an optical gantry depends on the beam line elements that have to be included. All potentially utilized elements can be grouped into three categories, namely beam transport, beam shaping and patient safety elements. The whole particle beam line can be optimized by only utilizing the essential elements tailored to the beam properties and the desired delivery scheme (introduced in chapter 2.2).

Beam transport

Once particles are accelerated by the laser, the produced divergent beam must be guided to the patient. Depending on the opening angle the bunches can be directly fed into the beam line or must be captured at the entrance of it. With special targets small divergences can be obtained directly [45] or by generating electrostatic focusing fields [46] to avoid additional collecting devices. With larger divergence the beam has to be captured before guiding it through the beam line. This is a demanding task for broad energy spectra, especially with the condition to be efficient in collecting a high number of particles. A possible solution could be the use of pulsed solenoids to capture the protons [47, 48]. To avoid further diverging of the beam which would be undesirable especially in the spot-based and axial-layer-based delivery, the beam could be focused with quadrupoles [49]. The quadrupole doublets or triplets have to be installed several times within the beam line to keep the diameter of the bunch small until the beam exits the treatment nozzle. Certainly, this task is not easy to fulfill since many energies have to be re-focused for broader spectra. The more monoenergetic the spectrum is, the easier is the focusing within the beam line.

Before exiting the treatment head scanning magnets can be used to deflect the beam to different spots or clusters which will be necessary for any intensity modulated proton therapy technique. In the case of using the optical gantry, this scanning can also be accomplished by simple movements of certain parts of the gantry, which is called gantry scanning [10, 11]. This flexibility is possible since the laser is directed with mirrors inside the gantry, permitting an easy elongation or rotation by just adjusting the mirrors, rather than the bending magnets. Possible variations are shown in figure 3.2, where 3.2a) illustrates a normal gantry movement by a rotation of the whole system and figure 3.2b)-e) depict additional movements only achievable with an optical gantry. More precisely, figure 3.2b) and 3.2c) represent a feasible tilt of either the front gantry arm or the treatment head by a tilt of the respective mirror (moving part is highlighted in green). Figure 3.2d) shows an elongation (or shortening) of the gantry arm. Besides the rotation of the whole gantry a rotation of the treatment head around the laser beam axis is also possible as indicated in figure 3.2e). Whether this gantry scanning could be used will depend on the additionally required beam line elements and the final flexibility of the optical gantry (which may be restricted due to a heavy treatment head, for instance).
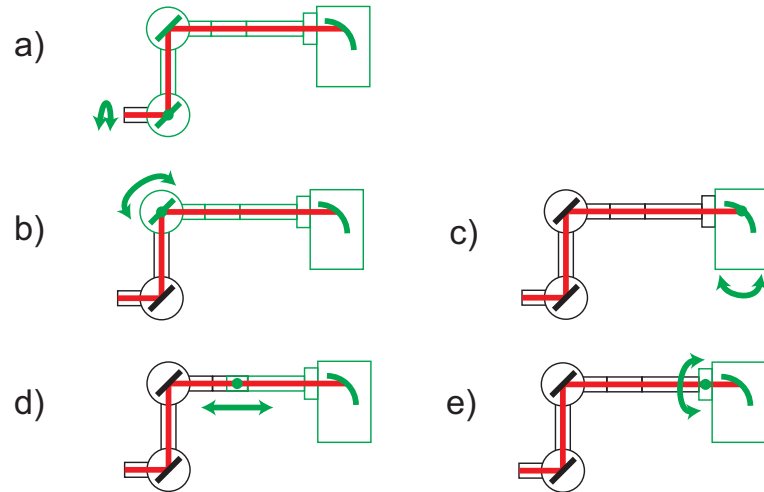
Figure 3.2: Gantry scanning possibilities with a flexible optical gantry (adapted from [10]). Black parts do not move, while green parts can move. a) shows a normal gantry movement whereas b) and c) demonstrate a tilt with different mirrors. In d) an elongation is illustrated and e) represents a rotation of the treatment head around the laser beam axis.

With the so far introduced beam line elements, the proton bunches can be captured and fed into the beam line after being accelerated by the laser. The beam can be transported through the beam line towards the patient allowing for scanning of the beam over the target to deliver the planned dose. However, on its way through the beam line, the beam must be modified or shaped additionally to meet the requirements for high quality proton treatment.

Beam shaping

To shape the beam individually for each patient, some beam elements equal to those of a conventional particle therapy beam line can be used like scatter foils, energy degraders (or range shifters) and collimators. Such a collimator would ideally be a multileaf collimator like those utilized in photon therapy or a circular collimator with an adjustable diameter. Besides these conventional components, specific ones are required tailored to laser-accelerated protons. Tailored to laser-driven protons elements are needed to deal with broad energy spectra, high fluences/high proton numbers per bunch and many ion species contained within the bunch. The extremely short time structure of the proton bunches does not play an important role in the beam shaping, however can be regarded as an advantage as discussed in section 3.2.

Energy Selection System (ESS). As the energy spectrum of the bunch is broad (even for RPA spectra it is broader than monoenergetic), an ESS will certainly be essential. Such a system as proposed by Fourkal *et al.* [42] is illustrated in figure 3.3. This ESS consists of four static dipole magnets with specifically arranged magnetic field orientations (see figure 3.3). Additionally, two variable beam blocker pairs, i.e. collimators need to be installed, one in the center of the ESS and another one at the exit of the ESS. The magnetic fields force the protons to separate in the central plane depending on their energy. Electrons, if contained in the arriving bunch will be deflected in the opposite direction, i.e. in downwards direction, and could be blocked, if necessary. Two proton trajectories are depicted in figure 3.3. The upper trajectory exemplarily represents lower energy protons which are deflected more by the magnetic field than higher energy protons following the lower trajectory. Due to the separation in energy, the central collimator can filter certain protons with selectable energies by varying the position and aperture size. Depending on the settings a monoenergetic beam or a small part of the incoming spectrum exits the ESS at the second beam blocker.
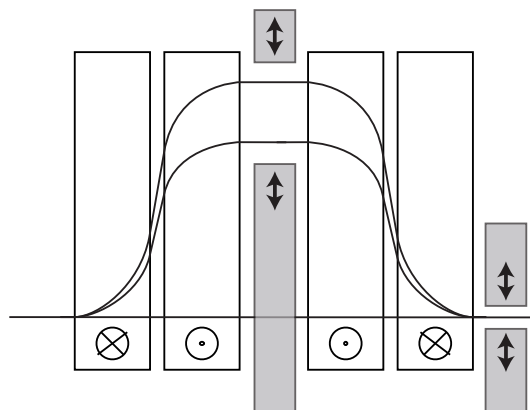

Figure 3.3: Schematic diagram of an energy selection system (ESS) using static magnetic dipole fields. Protons coming from the left are deflected by the magnetic fields and follow different trajectories depending on their energy (lower energies are deflected more and follow trajectories similar to the upper one whereas higher energies stay closer to the original path and follow trajectories similar to the lower one). Therefore, the protons separate in the central plane depending on their energy and the first, central beam blocker can select desired energies. These selected energies exit the ESS at the second beam blocker on the right. This figure was adapted from Schell [10].

Energy Modulation System (EMS). In order to modulate the energy spectrum, one can additionally add scattering material in the central part of the ESS like a wedge for example (as illustrated figure 3.4). Then, protons with different energies
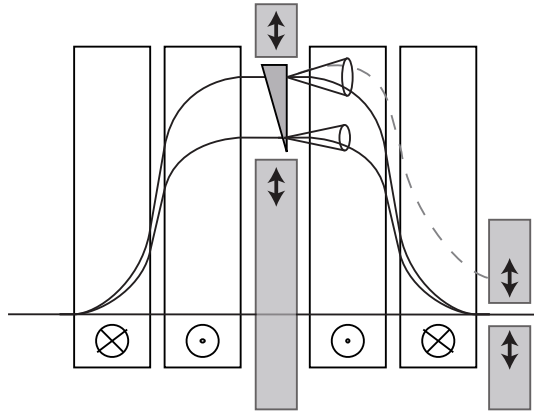
Figure 3.4: Schematic diagram of an energy modulation system (EMS). The EMS is based on an energy selection system (shown in figure 3.3) with an additional scattering material (wedge) included in the central plane of the device. The wedge scatters protons with lower energies more than those with higher energies. Therefore, different amounts of protons can exit the second beam blocker for different energies which allows for modulating the whole energy spectrum of the bunch. This figure was adapted from Schell [10, 50].

transit different thicknesses of scattering material and, hence, exit this material with energy dependent scattering angles. Protons which are deflected too far from the optimal trajectory cannot exit through the second beam blocker at the end of the ESS (like the dashed trajectory in figure 3.4). This allows to control the number of protons per energy bin and, therefore, modulating the depth dose distribution of the proton bunch (e.g. to produce a SOBP within one proton bunch [50]). Conventional modulator wheels cannot be utilized within a single bunch (due to the bunch duration in the order of a nanosecond), but could be employed in a scenario with a certain number of shots for each step of the modulator wheel.

Particle Selection System (PSS). If the bunch consists of a mixture of positive ions a PSS will be required since treatment is commonly performed with only one ion species. An ESS can be expanded to a PSS by including electric fields to select particles with a desired charge per energy ratio. If a monoenergetic beam will be selected by the ESS, one electrode constitutes the simplest way to realize a PSS as shown in figure 3.5. Since the positive ions are deflected in the electric field, the downstream system has to be bent slightly to ensure that the required particles are guided to the exit of the PSS. This system can, for example, be adjusted to just supply protons if the laser-driven beam consists of a mixture of particles. Of course, if the transport of a broad energy spectra is required, the PSS gets more complicated.
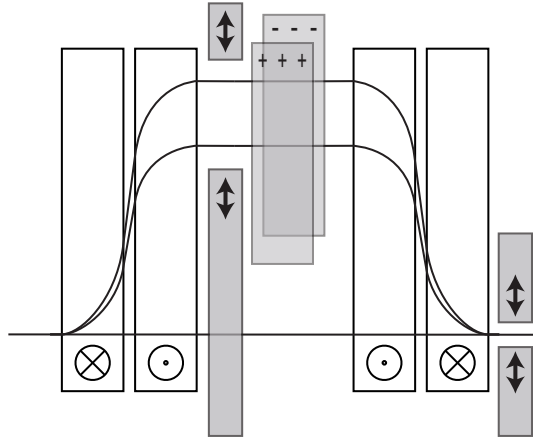
Figure 3.5: Schematic diagram of a particle selection system (PSS). The PSS is based on an energy selection system (shown in figure 3.3) with an additional electric field to select particles with the desired charge per energy ratio. To ensure that the desired ions exit the PSS, the downstream system has to be bent such that the second beam blocker lets only the desired particles pass. This figure was adapted from Schell [10].

Fluence Selection System (FSS). Depending on the number of protons contained in one bunch, a further element could be needed to regulate the fluence. This could be useful in case of very high particle numbers per bunch or if a spatial shape of the beam is explicitly wanted (like e.g. in the lateral-layer-based delivery). Even if the fluence would not be too high, the desired proton number to be delivered to one spot or cluster must not be an integer multiple of the proton number contained in one shot. In such a scenario, a FSS could modulated the fluence from shot to shot to exactly reproduce the desired and planned amount of dose for the certain spot or cluster. One implementation of a FSS could spread the beam using a scattering foil and blocking the undesired part of the broad beam by a (multileaf) collimator, as illustrated in figure 3.6. In the case of having a broader beam guided through the whole beam line or a capturing solenoid at the entrance of the beam line (where the bunch is broad due to the divergence) a single collimator could also undertake the task of a FSS. This, however, is only possible if the protons should exit the nozzle with a small diameter and not in the case of the lateral-layer-based or the partial-volume-based delivery where a broadening of the beam is explicitly wanted.

Until now only elements related to the beam shape and transport to the patient has been discussed. To ensure a correct treatment additional patient safety elements have to be considered.
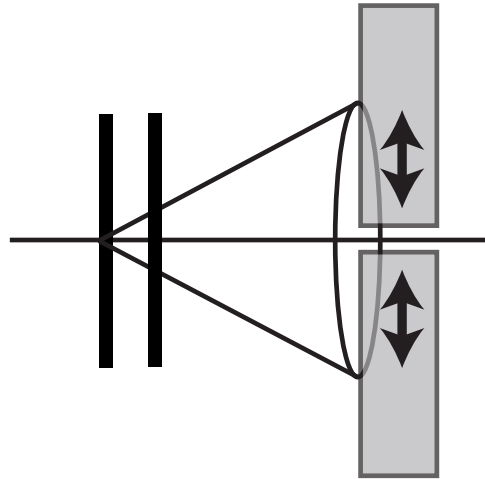
Figure 3.6: Schematic diagram of a fluence selection system (FSS). The beam is
spread laterally by two scatter foils and the desired amount of protons
can be selected by a certain opening of the subsequent collimator/beam
blocker. This figure was adapted from Schell [10].

Patient safety

Since these beam lines are utilized to treat cancer patients, safety elements are
strongly required to ensure a safe and correct treatment. Therefore, detectors to
monitor the beam in real-time are necessary which can measure the total fluence,
the beam position and potentially the energy spectrum of the bunch. Conventional
ion beam detectors usually do not have to deal with broad spectra nor with such high
proton numbers arriving over timescales of some nanoseconds. Hence, dedicated de-
tectors have to be investigated for laser-driven protons. But again, the requirements
of the detectors depend on the produced beam and on the reliability of the beam
exiting the beam line. Maybe, the energy must not be measured for each single
shot if, for instance only the cut-off energy of the spectrum is fluctuating. In this
scenario, the ESS would block this part of the initial spectrum anyway and the fil-
tered spectra are not fluctuating from shot to shot. Schell *et al.* proved furthermore
that only the proton number variations (and not the exact spectrum shape) result
in remarkable dose deviations when utilizing an exponentially decaying, TNSA-like
proton spectrum [51]. Therefore, the final spectrum and the beam line reliability will
show what the future detectors must provide. Furthermore, (very) fast beam block-
ers or similar devices have to be included to stop the beam if a detector measured
an inconsistency compared to the planned delivery. Since the bunches are extremely
short and repetition rates of about 10 Hz will probably required in clinical routine,
such beam stoppers might be challenging.
Another essential safety element is the shielding material to avoid exposure of the
patient by secondary radiation. This secondary radiation is produced when blocking

undesired parts of the initial proton spectrum (whether it is done in the ESS or the FSS or in other parts of the beam line). The thickness of the blocking material will depend on the laser-generated incoming spectrum and also on how efficient the protons can be used for therapy. For instance, the layer-based or partial-volume-based deliveries constitute an advantage since less protons need to be dumped, i.e. more protons are actually used for the treatment. In general, less shielding is expected when the initial spectrum is as narrow as possible and if the ESS would not be represented by a chicane design. Faby *et al.* have shown that such a setup is not the optimal solution for an exponentially decaying, broad proton spectrum and recommend to use an alternative ESS design [52].

Optimization of beam line composition

Having presented all potential beam line elements above an optimal composition has to be found to enable a correct, safe and high quality treatment with the least amount of devices. Besides the mandatory patient safety elements and some type of beam scanning (either with sweeping magnets or the gantry scanning), certain beam line elements must be included in the final composition depending on the beam properties and/or the delivery method. A mixture of initial particles, a high fluence and different options for the energy spectrum are considered to be such properties. The options are broad or narrow spectrum shapes with either a fixed or variable maximal energy. The considered delivery methods that allow IMPT are the spot-based, the lateral-layer-based, the axial-layer-based and the partial-volume-based delivery (for explanations see chapter 2.2). Table 3.1 gives an overview which devices must be incorporated in the beam line "independent of beam properties" (upper part) or "dependent of beam properties" (lower part).

For all delivery methods except the lateral-layer-based one, focusing devices are required to keep the diameter of the beam small when exiting the beam line. This is necessary for every spot and every axial layer and may be necessary for some small partial volumes. For the lateral-layer-based delivery, however, the beam is spread anyway and therefore a focusing device is not essential. To spread the beam laterally, a FSS is required for the lateral-layer-based and the partial-volume-based delivery independent of the beam properties to cover a wider area within the target. However, a FSS must be included for the spot-based and axial-layer-based delivery as well if the fluence per shot is very high and needs to be down-regulated during delivery. When the beam consists of several particles, a PSS could choose just protons for the patient treatment, and therefore the PSS is listed in the row of "mixture of particles" independent on the delivery scheme (i.e. in each column). For every delivery scenario all four possible energy spectrum configurations are listed in table 3.1. It is clear, that in the case of broad energy spectra an ESS is needed, independent whether the maximal energy is fixed or variable. For fixed and narrow energy spectra an energy degrader (Deg) is needed to adjust the range in the patient. When the energy is fixed but with a broad spectrum, the ESS takes the function of the degrader and, therefore, no additional degrader is needed. Depending on the delivery

Table 3.1: Required elements for a laser-driven beam line depending on the dose delivery schemes (columns). For each delivery method the required elements are given dependent or independent of the beam properties. This table only includes optional beam line elements. Mandatory devices (e.g. for patient safety) which are needed in any case are not listed here.

|	spot-based				lateral-layer-based				axial-layer-based				partial-volume-based			
maximal energy:	fix	variable	variable	fix	fix	variable	variable	fix	fix	variable	variable	fix	fix	variable	variable	fix
energy spectrum:	broad	broad	narrow	narrow	broad	broad	narrow	narrow	broad	broad	narrow	narrow	broad	broad	narrow	narrow
needed independent of beam properties																
focusing	←				←				←				←			
mixture of particles	PSS				PSS				PSS				PSS			
fluence very high	FSS				FSS				FSS				FSS			
needed dependent of beam properties																
	ESS	ESS	-	-	ESS	ESS	-	-	ESS	ESS	-	-	ESS	ESS	-	-
	-	-	-	-	-	-	-	-	EMS optional	EMS optional	EMS	EMS	EMS optional	EMS optional	EMS	EMS
	-	-	-	Deg	-	-	-	Deg	-	-	-	Deg	-	-	-	Deg
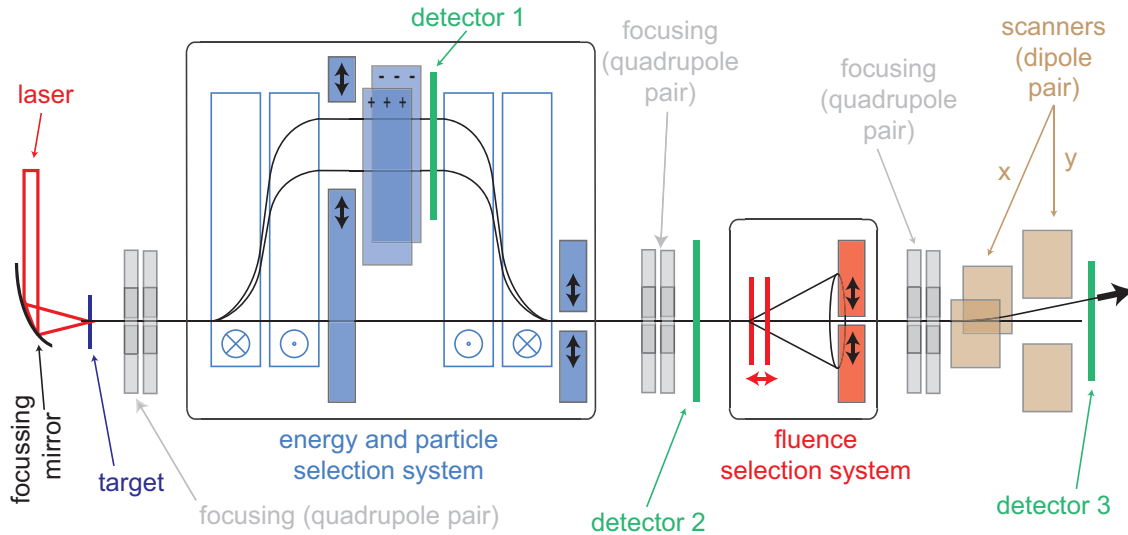
Figure 3.7: Simple assembly of beam line elements that are required in a laser-driven proton therapy unit. This beam line composition can deal with broad energy spectra, high fluences and a mixture of particles per bunch. Quadrupole doublets focus the beam on its way through the beam line and detectors are installed to monitor the beam. Two dipole pairs can scan the beam over the target when exiting the beam line. This figure was adapted from Schell [10].

an EMS is either required or optional. Note that table 3.1 was adapted from the table previously published [11] since this chapter only addresses intensity modulated proton therapy (which excludes the target-volume-based delivery method).

Table 3.1 demonstrates the range of possible variations in the beam line. Going from left to right (i.e. from spot-based delivery to partial-volume-based delivery), more and more elements are required in the composition. An important factor is the initial energy spectrum, as mentioned often before, which strongly influences the required beam line. This stresses that the final beam line setup is highly dependent both on the beam properties but also on the desired dose delivery method.

One example of a final beam line (or treatment head for a gantry design) is represented in figure 3.7. This beam line is designed for an axial-layer-based treatment delivery but could be also utilized for any other intensity modulated delivery scheme. The incoming bunches are assumed to arrive with a small divergence (hence no capturing device is installed) but with a broad energy spectrum containing a high fluence and other ions than just protons. Utilizing table 3.1 this beam line contains an energy selection system with an incorporated particle selection system and an additional fluence selection system. Moreover, focusing elements and detectors are included repeatedly. At the exit of the beam line, the beam can be scanned

over the target with scanning magnets. This example contains already a lot of devices and it would be disputable whether all these devices could be stored within a treatment head of a compact optical gantry. This cannot be answered until the laser-accelerated proton bunch and its properties are understood well enough and one would start to build the appropriate gantry.

3.2 Beam lines based on pulsed magnetic fields

Masood *et al.* have developed a completely different beam line design for laser-driven proton therapy [53]. They investigated a compact proton gantry based on pulsed magnetic fields and performed a particle tracking simulation guiding a TNSA spectrum through the beam line. A schematic diagram is given in figure 3.8 where the laser enters the gantry from the left, is deflected by a parabolic mirror and impinges the target at the exit of the laser-target-chamber. The produced protons are captured by a pulsed solenoid with variable field strength. This solenoid pre-selects a desired nominal energy E_{nom} by collimating protons having energies close to the nominal energy and guiding them to an optimal trajectory inside the first bending magnet. The bending magnet is a 90° pulsed sector magnet that guides the protons into the Integrated Shot-to-shot Energy Selection System (ISESS) consisting of two apertures and a pulsed quadrupole triplet. The first aperture filters a coarse part of the spectrum whereas the fine-tuning is performed with the quadrupole triplet acting as a chromatic focusing lens (cf. [53]). Protons with a bandwidth $\Delta E/E_{nom}$ around E_{nom} can pass the second aperture at the end of the ISESS. The passing bandwidth depends directly on the aperture radius of this second collimator. By passing two other quadrupole triplets and another 90° pulsed sector magnet the beam is re-focused and guided to the patient (or to the water phantom like in figure 3.8). The last quadrupole triplet can actively shape the field size of the bunch exiting the beam line to have a diameter of 1-6 cm at isocenter. Note, that the quadrupole triplets re-focus the divergent bunch repeatedly to keep the diameter of the beam small. This is necessary since the solenoid captures the (very divergent) initial bunch but cannot eliminate the divergence completely. The filtered protons still have a divergence (much smaller than the initial divergence) and, therefore, also exit the beam line with an opening angle. This was taken into account when stating the field sizes at the isocenter.

This compact gantry can rotate around the iso-line, i.e. the entering laser beam axis and, therefore, is able to deliver the protons from 360° to the patient. Figure 3.8 sketches the different energies of the initial spectrum at different positions within the beam line in a color code. In this example, an energy of around 150 MeV (light green) is selected with the ISESS.
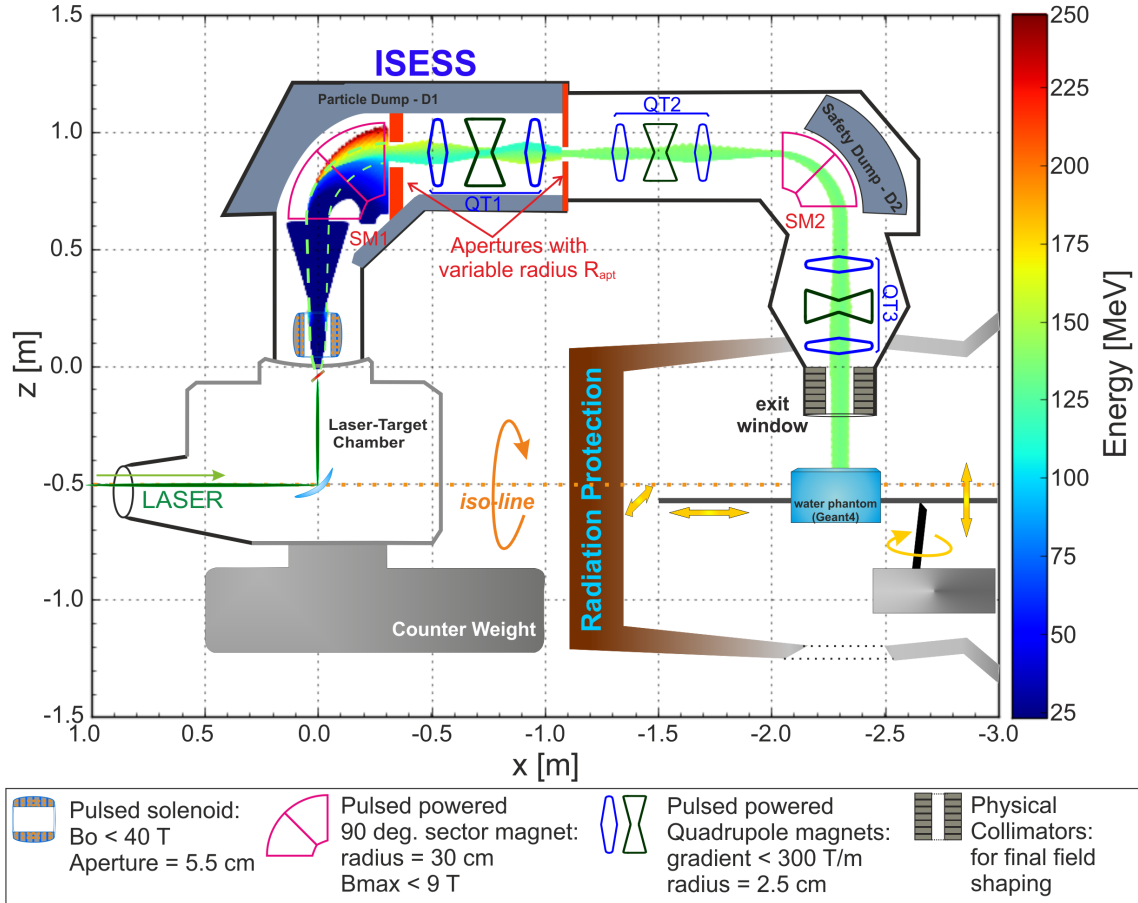
Figure 3.8: Sketch of a compact gantry for laser-driven protons utilizing pulsed magnets [53]. With this design a broad energy spectrum (energies shown in color like in the energy legend) can be guided to the patient and a desired energy can be filtered with the Integrated Shot-to-shot Energy Selection System (ISESS). The utilized devices are illustrated at the bottom of the picture.

The great advantage of utilizing pulsed powered magnets are the high magnetic fields that can be obtained. These high fields last only for very short times (microseconds), however, long enough to bend the extremely short bunches (nanoseconds). Comparing the two time scales, the magnetic fields can be considered as constant during the transit of a proton bunch. Thus, the time characteristics of the laser-driven bunches can be utilized as an advantage in this beam line design. When having higher magnetic fields, high energy particles can be deflected with much smaller bending radii and therefore the gantry can be kept very compact with an diameter of only about 3 m. Furthermore, pulsed magnets with air-cores are much lighter compared to iron-core magnets, allowing a fairly light gantry design.
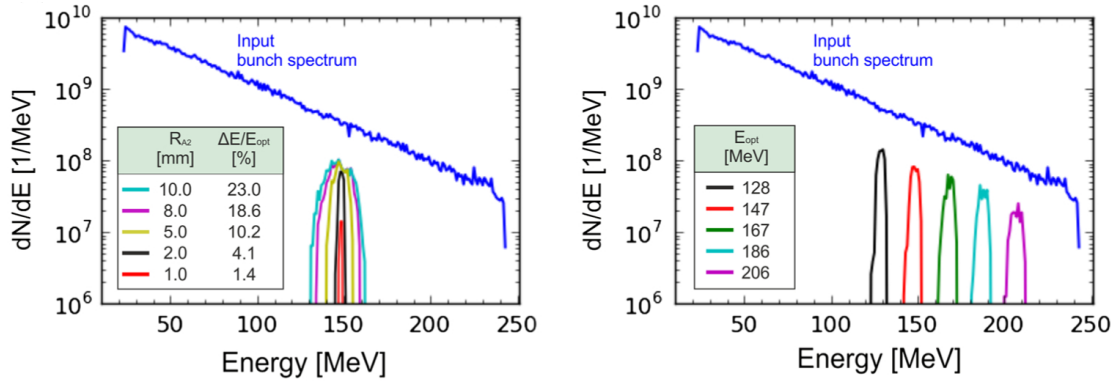
Figure 3.9: Simulation results for the pulsed gantry design showing the input TNSA spectrum as well as potential filtered spectra. On the left five spectra with different bandwidths $\Delta E/E_{opt}$ are shown for a fixed nominal energy depending on the radius of the second aperture at the ISESS. On the right five spectra with different nominal energies are illustrated (for a fixed aperture radius). This figure was taken from Masood [53].

Masood conducted a complete particle transport simulation for this beam line and, therefore, the exact shapes of all possible filtered spectra are known (under the assumption of the initial laser-produced energy spectrum) [53]. In Figure 3.9 the utilized input spectrum is shown with some simulated filtered spectra. On the left side different bandwidths for a nominal energy of 150 MeV are illustrated whereas on the right side several spectra with different nominal energies are shown. All potential producible spectra obtained with this simulation have been used to perform the treatment planning study in chapter 5 investigating the feasibility of this gantry design and laser-driven proton therapy in general.

4

A treatment planning system for laser-driven proton therapy

This chapter introduces the Matlab based research treatment planning system (TPS) LAP-CERR (Laser-Accelerated Particle CERR) utilized for the planning study in chapter 5. It is based on the open source software CERR (A Computational Environment for Radiotherapy Research, [54]) originally developed for photon dose calculations which was expanded to calculate dose distributions for protons with broad energy spectra [10]. The general tools of LAP-CERR are presented as well as specific implementations tailored to laser-driven bunch properties. Besides treatment planning with laser-driven protons, LAP-CERR can furthermore calculate carbon ion treatment plans and deal with biological uncertainties [55], however, only the tools that are relevant for this thesis are explained below. At first a basic summary of the important tools is given followed by a detailed description of the planning process with LAP-CERR. In the second part of this chapter the handling of broad energy spectra is explained and two studies are presented that were carried out during this thesis addressing the high fluence per bunch and the divergency. It should be mentioned that although proton plans are usually expressed in RBE-weighted dose, in the following the term 'dose' refers to the physical dose to leave out changes of the relative biological effectiveness (RBE) within the patient.

4.1 General tools of the planning system

LAP-CERR is an inverse treatment planning system which can generate intensity modulated proton therapy (IMPT) plans for real patient data sets. One can import patient computed tomography (CT) images together with structure sets contoured in other treatment planning systems. However, the delineation of volumes of interest (VOIs) can also be performed within LAP-CERR. These VOIs are mainly the planning target volume (PTV) or target where the dose is delivered to and the organs at risk (OARs) to be spared. Since a 3D CT stack is divided into small elements called voxels all discussed TPS tools are voxel based as well. This means the dose to each voxel is optimized separately to either receive a dose close to the prescribed dose (for a PTV voxel) or as low as possible dose (for an OAR voxel or the normal

tissue voxels). Therefore, a voxel based dose calculation is required computing the so called influence matrix (explained in detail in section 4.1.2). With a simple pencil beam algorithm the dose-to-water is determined for each voxel within the patient depending on various potential beam configurations. The total 3D dose distribution is optimized to meet the user defined prescriptions as good as possible. For laser-driven proton plans the software package Mosek (www.mosek.com) is utilized for this optimization relying on a quadratic cost function (see explanation below). The generated proton plans can be analyzed by evaluating typical parameters like maximum, minimum and mean doses of certain VOIs as well as by evaluating dose-volume-histograms (DVHs). Most recently, the tumor coverage, the conformation and the homogeneity of the PTV or other clinically relevant parameters like $D_{2\%}$ and $D_{98\%}$ or $D_{min}(1cm^3)$ or $D_{max}(1cm^3)$ representing dose values close to the absolute minimum and maximum within the target can be obtained. The definitions of the mentioned criteria can be found in section 4.1.4.

In this context, it should be mentioned that both, the dose calculation and the dose optimization implemented in LAP-CERR, are in some aspects qualitatively different compared to commercial planning software tools for radiotherapy. One the one hand, the proton dose calculation only considers the tissue densities, i.e. CT Hounsfield units, along the central pencil beam axis which causes errors in the dose calculation for significant tissue density variations in the off-axis region of the pencil beam [56]. However, these errors are small and irrelevant when the tissues are relatively similar, i.e. when avoiding CTs with very dense tissue (e.g. bones) close to air cavities (e.g. lungs). On the other hand, the utilized optimizer only allows for specific constraint types, for instance, a prescribed dose constraint or hard constraints. Hard constraints imply that the optimization runs until the certain constraints are fulfilled, i.e. hard constraints are always met. However, for the optimization of laser-driven proton plans only prescribed dose constraints are utilized. This means, the dose is optimized to exactly the given dose value independent if the achieved dose is lower or higher. Typical maximum or minimum dose constraints to the whole VOI or even dose constraints for a given percentage of a volume ($V_{xGy} = y\%$) cannot be realized with the implemented solver (see section 4.1.3). This makes the choice of appropriate penalty factors difficult, especially since no on-line changing of constraints or penalty factors is possible as in conventional planning systems. Anyway, good plan qualities can be achieved with LAP-CERR by carefully choosing the penalty factors by trail and error. Moreover, Schell showed in his PhD thesis that the dose calculations produced with LAP-CERR compare well with Monte Carlo generated dose distributions [10]. Therefore, this TPS can be utilized with clear conscience for research purposes.

At the beginning of the planning process the user has to define some settings and provide required data before starting the dose calculation and optimization. At first, the source data needs to be fed into the TPS, i.e. all possible beam configurations have to be included into the database. Since LAP-CERR is a research TPS any reasonable input can be utilized ranging from one to several beam options.

For laser-driven proton therapy these different configurations need to include the exact energy spectrum shape and its contained particle number per bunch. Other database requirements like pre-calculated depth dose distributions or lateral spread distributions are already included. Then, the patient data needs to be loaded and the required VOIs need to be defined including the prescribed dose for the PTV. Different VOIs or especially OARs can by assigned with different importances by choosing appropriate penalty factors for the optimization. Afterwards, the user has to define at least one beam angle for irradiation (more may improve quality but elongate calculation time). These angles stay constant throughout the whole planning process as in conventional planning systems. Different beam directions later on count as different beam configurations when calculating the dose for every possible combination. Last, one of the IMPT delivery scheme presented in chapter 2.2 has to be chosen for planning. Then, the dose calculation can be started.

4.1.1 Raytracing and spot placing

For all possible delivery methods in LAP-CERR spots are placed inside the PTV where the dose is delivered to later on. This is done for every beam separately and always refers to the projected target to the isocenter plane in beams eye view (view from the source to the isocenter in beam direction). Such a projected plane is illustrated in figure 4.1a) where the center of mass (COM) of the target lies in the isocenter (as always in LAP-CERR). In this plane intersection points are placed around the isocenter with the spot distances Δx and Δy (see figure 4.1a)). These distances do not depend on the depth in the PTV but are fixed and only depend on the beam width at patient entrance (see section 4.2.2).

Now, a raytracing is performed in beam direction from the source through the points of intersection. Along each ray the radiological depth (or water equivalent depth) d_{rad} of each point is computed [57]. By considering all crossed voxels and their Hounsfield units, i.e. electron densities, the relative stopping powers can be obtained by a conversion table (in the database of the TPS). With these stopping powers S_{rel} the radiological depth d_{rad} can be calculated for each geometrical depth d_{geo}:

$$d_{rad} = \int_0^{d_{geo}} S_{rel}(x)dx$$

These rays or pencil beams intersect the whole CT stack and the spots are placed along the pencil beams inside the target starting at the largest radiological depth at the most distal edge of the target. This is sketched in figure 4.1b). The spots have a predefined water equivalent distance Δz and are placed with this distance until the proximal edge of the tumor is reached (must not be reached exactly). Note that the spots are placed on a radiological grid and not a geometrical grid. Both grids are only identical in a water phantom like in figure 4.1.
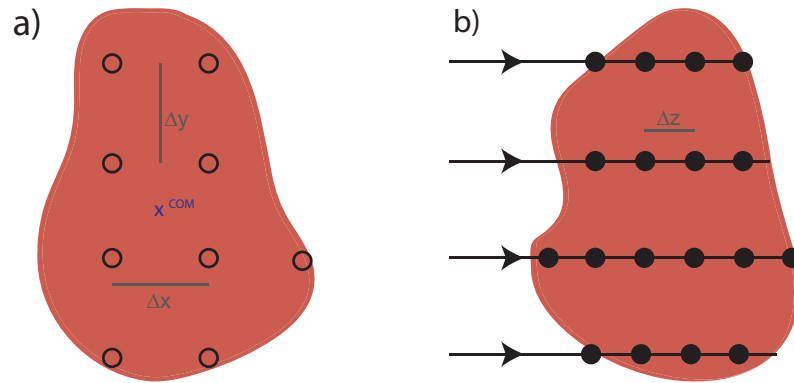
Figure 4.1: Schematic explanation how the spots are placed inside the target volume. a) shows the target projected to the isocenter plane in beams eye view (with the center of mass (COM) lying on top of the isocenter). Intersection points are set with a lateral distance Δx and Δy where the pencil beams cross the isocenter plane. b) depicts the target in the y-z plane. The pencil beams penetrating the target from the left are illustrated as well as the spots which are placed along the pencil beams with a radiological spot distance of Δz.

The lateral distances as well as the distance in depth between the spots have to be chosen reasonable since with too few spots too far away from each other the dose cannot be deposited homogeneously within the target. However, with too many spots too close to each other, many spots get irrelevant during the optimization anyway but the computation time will be long. Considering this trade-off the values for the lateral spot distances Δx and Δy are chosen beam width dependent as explained in section 4.2.2 and the distance in depth Δz is set to 0.5 cm which proved to be a good value for proton plans.

4.1.2 Dose calculation

For each possible beam configuration the 3D dose has to be computed. This is done with a pencil beam algorithm consisting of two parts. The first part is the depth dose distribution along the central axis (CAX) of the pencil beam D_{CAX}. This depth dose can be calculated via Monte Carlo simulations for instance, but can also be approximated by a formula developed by Bortfeld [58]. This implemented approximation only depends on the radiological depth $D_{CAX}(d_{rad})$. The depth dose distribution of the central axis represents the dose of one pencil beam integrated over the whole lateral extension of the beam (leading to the commonly known Bragg peak for monoenergetic beams). Figure 4.2a) shows a schematic diagram of the central axis of a pencil beam and the involved voxels. To calculate the 3D dose of one pencil beam, the second part of the pencil beam algorithm spreads the dose deposited in a certain depth d_{rad} on the central axis to the off-axis region in the same depth. This

lateral spread can be approximated by a Gaussian distribution due to the Multiple Coulomb scattering predominating the scattering process inside tissue. The lateral spread $L(x, y, d_{rad})$ depends on the displacements from the central axis x and y, the water equivalent depth d_{rad} and the beam width in this depth $\sigma_{x/y}$:

$$L(x, y, d_{rad}) = \frac{1}{\sqrt{2\pi\sigma_x^2(d_{rad})}} \cdot exp(-\frac{x^2}{2\sigma_x^2(d_{rad})}) \cdot \frac{1}{\sqrt{2\pi\sigma_y^2(d_{rad})}} \cdot exp(-\frac{y^2}{2\sigma_y^2(d_{rad})})$$

The width of the beam at a certain radiological depth can be calculated with the initial width of the finite pencil beam at patient entrance $\sigma_{0,x/y}$ and the small angle scattering theorem for Multiple Coulomb Scattering by Gottschalk [59] ($\sigma_{MCS}^2(d_{rad})$ is stored in the TPS database):

$$\sigma_{x/y}(d_{rad}) = \sqrt{\sigma_{0,x/y}^2 + \sigma_{MCS}^2(d_{rad})}$$
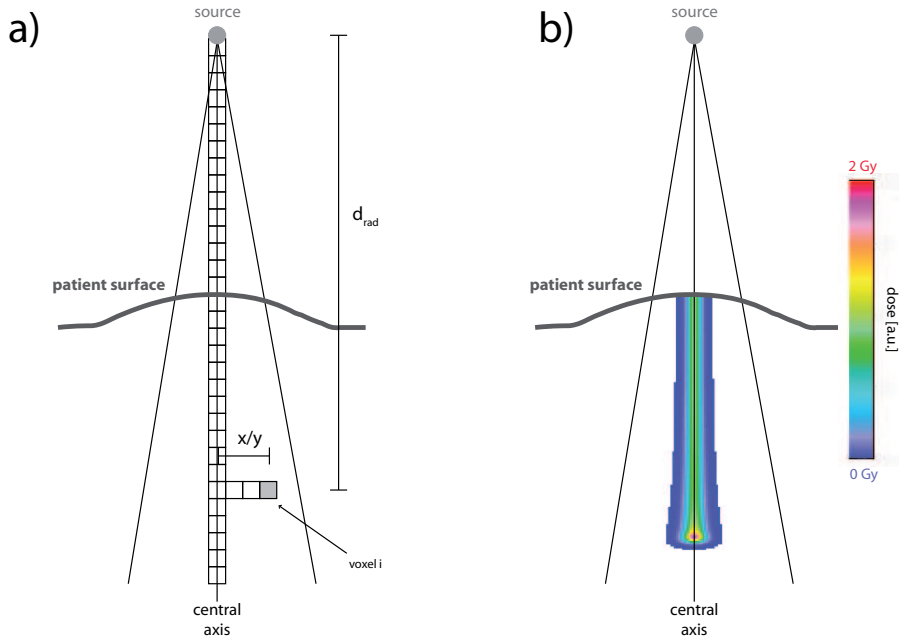
Figure 4.2: Schematic diagram representing the geometry used for the pencil beam algorithm. In a) the central axis of the pencil beam is illustrated. Along this central axis the depth dose can be computed for all voxels. To calculate the deposited dose in the voxel i (highlighted in gray), the dose in depth d_{rad} on the central axis is spread laterally to off-axis voxels in the same depth depending on the lateral displacement x and y. In b) the calculated dose distribution of a single (monoenergetic) pencil beam is illustrated. Figure a) was adapted from Schell [10].

The total dose at one point (x, y, d_{rad}) can then be computed using

$$D(x, y, d_{rad}) = D_{CAX}(d_{rad}) \cdot L(x, y, d_{rad})$$

Doing this for all voxels with given coordinates (x, y, d_{rad}) within the patient, a final pencil beam dose distribution is obtained. Such a pencil beam dose distribution is shown in figure 4.2b) for a monoenergetic proton beam.

This calculation is performed for every possible beam configuration j which means for every possible energy spectrum of a bunch coming from the defined beam directions. For each of these configurations j the dose delivered with one laser shot to each voxel i in the body of the patient is calculated and stored in the so called influence matrix D_{ij}. The computation of the D_{ij} matrix is referred to as dose calculation. By optimizing the corresponding weights ω_j of the single beam configurations the final dose D_i in each voxel i can be obtained via a simple matrix multiplication [60]

$$D_i = \sum_{j=1}^{N_j} D_{ij} \cdot \omega_j \tag{4.1}$$

with N_j being the total number of possible configurations. Since the entries of the D_{ij} matrix are normalized to the unit fluence of the corresponding beam configuration j, the weight ω_j directly represents the amount of laser shots of the respective configuration contributing to the dose D_i.

4.1.3 Optimization

To achieve the desired goals, like prescribed dose in the target and as low dose as possible in the OARs an optimization is performed. This optimization aims in finding the optimal weights ω_j of each beam configuration j and, hence, to find the optimal $D_i(\omega)$ in each voxel i as described with equation 4.1. To do this, a cost function is set up which is minimized during optimization. For laser-driven protons the utilized cost function is represented by a sum of least squares (cf. [10]):

$$F_0(\omega) = \sum_i p_i (D_i(\omega) - D_i^{pres})^2 = min$$

In this equation, p_i is the penalty factor and D_i^{pres} the prescribed dose for the voxel i which are both defined by the user. With high penalty factors the deviation of the actual dose to the prescribed dose $D_i(\omega) - D_i^{pres}$ contributes significantly to the overall sum, whereas for lower penalty factors these deviations contribute less. Since the deviation is squared and no restriction is possible for the deviation terms, only prescribed dose constraints can be utilized in this cost function. This means, a deviation from the prescribed dose is penalized independent on an overdosage or an underdosage. Therefore, the only possibility to achieve as low dose as possible within the OARs is to prescribe 0 Gy to these organs. Otherwise, when prescribing

the tolerance dose of the certain organ, the optimizer tries to achieve this dose in the organ even if a lower dose would be possible under the given conditions. The only way to steer the optimization in the desired direction, i.e. allowing more dose in a certain organ compared to another organ, is by varying the respective penalty factors. This turns out to be tough since not only the penalty values but also the amount of voxels belonging to certain OARs contribute to the optimization results. Hence, the appropriate penalty factors mainly have to be found by trail and error. With the penalty factors and prescribed doses assigned to various structures, the cost function is minimized iteratively to find the best possible solution for the given beam configurations.

The determined weights ω_j then define how many percent of a shot with configuration j contributes to this optimal solution. Since the beam configurations j are defined depending on their fixed particle number per bunch, the dose influence to one voxel is normalized to this proton number. Therefore, an optimized weight $\omega_j = 1$ corresponds automatically to one full laser shot of configuration j. Similarly, $\omega_j = 0.5$ corresponds to half a shot and $\omega_j = 2$ to two laser shots. This normalization is very important for the planning study later on, especially because the solver calculates floating point numbers for the weights which neither the laser nor the beam line can reproduce without any specific beam line modification.

4.1.4 Evaluation of plans

There are many ways to evaluate the quality of a treatment plan. In general, a medical doctor surveys the 3D dose distribution and decides whether the plan is clinically acceptable or where improvements are required. Besides the visual consideration of the dose, other evaluation criteria support the decision of the physician. Such criteria are the maximum, the minimum and the mean dose of the PTV and for instance the maximum dose in an organ. These parameters can be computed easily by just finding the voxel with the most or the least dose inside the structure or by calculating an arithmetic mean of all voxel doses of the analyzed VOI. Besides minimizing the dose to the OARs in the planning process the maximum dose of the PTV is minimized (to be lower than 110% or rather 105% of the prescribed dose, depending on the clinical case) and the minimum dose is maximized (to be higher than at least 90% or rather 95% of the prescribed dose, again depending on the clinical case). However in some cases, the absolute maximum or minimum dose in one voxel is not representing the plan quality. One example could be a very high dose in only one PTV voxel compared to other target voxels which receive a dose close to the prescribed dose. Therefore, evaluation criteria describing the dose to a certain volume of the PTV may represent the overall plan quality better than an absolute dose value in one voxel. Such criteria are for instance $D_{2\%}$, $D_{98\%}$, $D_{min}(1cm^3)$ and $D_{max}(1cm^3)$ which were implemented in LAP-CERR during this thesis. $D_{2\%}$ and $D_{98\%}$ refer to the dose that 2% or respectively 98% of the PTV volume is receiving. Hence, these values represent the minimum and maximum dose

closely and the extremums contribute only partly. Similar to that the $D_{min}(1cm^3)$ and $D_{max}(1cm^3)$ parameters are the minimum and maximum dose values at least $1\,cm^3$ of the target volume is receiving. Depending on the whole target volume one or the other parameter pair represents the dose to the PTV better than the other.

Besides the minimum and maximum dose values of the PTV there are additional criteria defining the plan quality. The medical doctor analyzes whether the target is irradiated homogeneously with dose, whether a certain amount of dose (mostly 95% of the prescribed dose) covers the whole PTV and how well the dose conforms to the target structure. This can be done by considering the dose distribution visually or by calculating respective quality indices. Various possible indices have been published in literature (e.g. [61, 62, 63] and references within), however for LAP-CERR the following were chosen and implemented: the Tumor Coverage (TC), the Conformation Number (CN) and the Homogeneity Index (HI):

$$TC = \frac{V_{T,p}}{V_T} \qquad CN = \frac{V_{T,p} \cdot V_{T,p}}{V_T \cdot V_p} \qquad HI = \frac{D_{max} - D_{min}}{D_{mean}} \qquad (4.2)$$

Figure 4.3 illustrates the utilized volumes, i.e. the target volume V_T (black), the whole volume receiving at least the prescribed dose V_p (purple) and the target volume receiving at least the prescribed dose $V_{T,p}$ (light blue). Note, the 'prescribed dose' was chosen to refer to the 95% isodose line basing on the clinical goal that at least 95% of the prescription dose is delivered to around 95% of the PTV (cf. [61]). This means, for a medical prescription of $2\,Gy$ per fraction the prescribed dose volumes for the quality indices enclose the voxels receiving at least $1.90\,Gy$ per fraction.

The TC index ranges from 0% to 100% and evaluates how many percent of the target receives the prescribed dose. The optimal coverage is achieved with the value TC=100%. The CN index as well ranges from 0% to 100% where CN=100% represents a perfect conformity. An optimal 2D dose distribution leading to a perfect TC and CN is depicted on the lower left in figure 4.3. The other two examples in the lower row of figure 4.3 demonstrate that both indices always have to be evaluated in parallel to clarify whether the irradiated volume is smaller or larger than the PTV. In the middle and on the right two different cases are illustrated yielding the same CN=90% but a different TC (either TC=90% or TC=100%). This means, the CN yields values smaller than 100% when the prescribed dose volume is either too small or too large. In such a case the simultaneously evaluated TC result has to be utilized to estimate the plan quality when only the indices are known but no 3D dose distribution. For the evaluation of the conformity other indices have been published in literature. However, the reason why this index was chosen is that the conformation number defined in equation 4.2 does not yield false positive or misleading results as other potential conformation indices do (explained by Lomax *et al.* [62]). The homogeneity index (HI) ranges from 0% to theoretically infinity with a perfect homogeneity at HI=0% meaning the minimum and the maximum dose
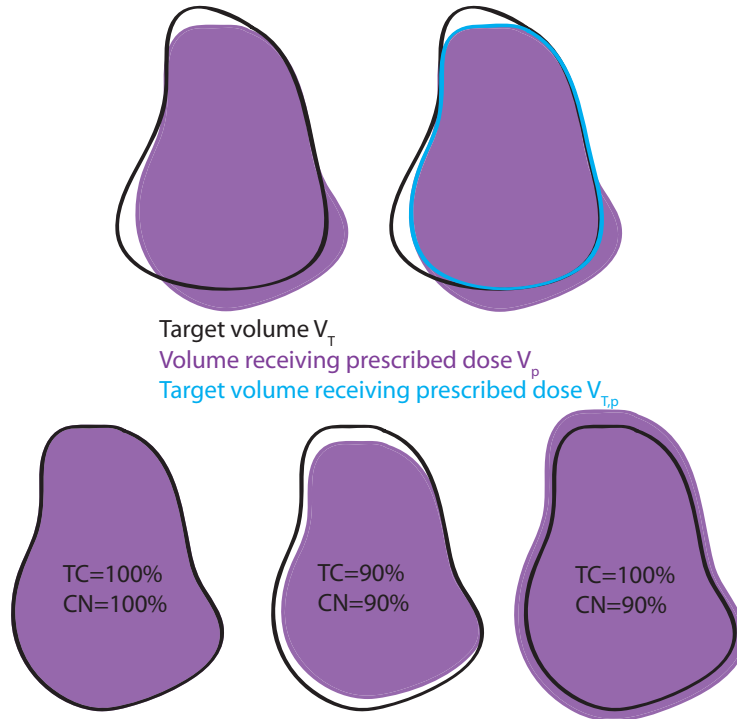
Figure 4.3: Description and example of the tumor coverage (TC) and the conformation number (CN). In the upper row the three utilized volumes are visualized in 2D to calculate TC and CN. In the lower row three examples are given with the corresponding TC and CN values. On the left an optimal dose distribution is shown compared to a case with a too small prescribed dose volume (middle) and a too large prescribed dose volume (right).

values are equal and the target is irradiated with the same dose in every voxel.

It should be mentioned that the three introduced indices are not (frequently) utilized in clinical routine, since a visual consideration of the 3D dose distribution is preferred. When analyzing multiple treatment plans at once, as done in the treatment planning study in this thesis, these indices simplify and speed up the evaluation of many plans in parallel. However, this index based evaluation needs pre-defined ranges or limits for each index defining the quality of a plan in general. These limits depend on the PTV and the patient anatomy and, therefore, have to be established precisely by a consideration of single 3D dose distributions and their respective indices. Since only two anatomies are utilized in the planning study presented in this work the elaboration of reasonable limits could be performed but these limits should only be applied for the selected cases.

Another indication for the plan quality can be the DVHs of different structures. Clinically utilized DVHs are mainly cumulative dose volume histograms and show the irradiated volume of the evaluated structure over the received dose. An example
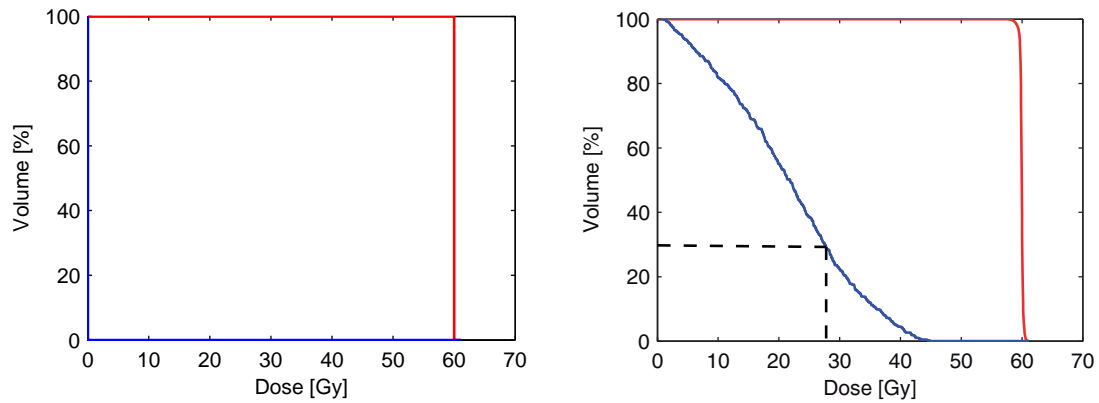
Figure 4.4: Cumulative dose volume histograms for a target structure (red) and an organ at risk (blue). The left DVH would represent an optimal dose distribution where the whole PTV receives exactly the prescribed dose of 60 Gy and the organ does not receive any dose at all. In the right DVH a more realistic scenario is shown where the organ receives some dose. The cumulative DVH states the relative volume of a structure receiving at least a certain dose, e.g. 30% of the organ receives a dose of at least 27 Gy (highlighted with dotted lines) in the right plan.

of an optimal and a realistic DVH for a PTV (red) and an OAR (blue) is provided in figure 4.4 for a prescribed dose of 60 Gy. The DVH curve represents the relative volume of a VOI receiving at least a certain dose. Therefore, for the PTV the optimal cumulative DVH is a step function decreasing from 100% to 0% at exactly the prescribed dose, meaning 100% of the PTV receives the 60 Gy and no part of the target receives a higher dose. For an OAR the optimal DVH would be represented by a delta distribution being 100% at 0 Gy. This would imply that 100% of the organ receives 0 Gy. However, since the organs often lie close to the target such an optimistic DVH cannot be expected. Typically the DVHs look like the right DVH in figure 4.4. In this, the whole PTV (100%) receives 57 Gy and around 60% of the target receive at least the prescribed dose of 60 Gy. The absolute maximum PTV dose is 61 Gy in this example. The organ which is shown in figure 4.4 has a maximum dose of approximately 45 Gy and only 30% of this OAR receives 27 Gy or more (highlighted with dotted lines). These 1D representations of a 3D dose distribution can be calculated easily and are frequently used for plan evaluations. However, the drawback of the DVHs is the loss of spatial information for which reason they should not be utilized without careful consideration of the 3D dose, at least for clinical cases.

4.2 Handling of specific laser-driven proton properties

In order to produce treatment plans for laser-driven protons modifications have to be performed in some TPS tools due to the specific properties of the laser-accelerated bunches.

For instance, this applies to the broad energy spectra. Even when the beam line filters smaller parts of the incoming proton spectrum, these spectra are still not monoenergetic. However, the pencil beam algorithm described above calculates the dose only for monoenergetic beams and, hence, this dose calculation has to be adapted. Therefore, Schell implemented a dedicated modification during his PhD thesis [10] which is presented in section 4.2.1. Additionally, he invented possible dose delivery schemes that are possible for laser-driven proton therapy (see chapter 2.2) and included algorithms in LAP-CERR that efficiently cluster certain spots to be irradiated together with one laser shot. In general, the clustering pre-selects certain beam configurations of all possible ones which reduces the number of decision variables for the optimization (less j's in the D_{ij} matrix) and potentially decreases the overall required laser shot number (since mostly more spots are irradiated with one shot). In the case of the axial-layer-based dose delivery which is utilized in the planning study in the next chapter, the clustering also decreases the amount of dumped protons by selecting energy spectra that are as broad as possible. This clustering certainly depends on the chosen delivery method but is only explained for the axial-layer-based delivery below. The processing algorithms for the other delivery schemes can be found in the PhD thesis of Schell [10].

Another issue in laser-driven proton therapy is the high and fixed proton number per bunch arriving over an extremely short time duration. In conventional proton therapy, the number of protons delivered to one spot can be adjusted to be any desired value. In this case, the beam widths (or spot sizes) are kept relatively small (approximately 5 mm FWHM [64]) to allow for a high intensity modulation in a certain area (for example one energy slice). Since the bunches produced with a laser contain an anticipated high number of protons (which cannot be down-regulated during the bunch duration) it might be necessary or helpful to spread the beam over a wider area within the target. This was already mentioned when discussing the possible dose delivery mechanisms for laser-driven protons and is addressed by the lateral-layer-based delivery. Another simpler option to decrease the fluence is to increase the beam width by varying the full width at half maximum (FWHM) of the Gaussian beam profile in the planning process. To investigate the optimal spot distance depending on the beam width a study was performed during this thesis analyzing the plan quality depending on the beam width and the spot distances. In this, the trade-off was addressed between dense spot grids leading to high quality plans with many spots (long computation and delivery time) and coarse spot grids impairing the homogeneity of the dose to the PTV (see section 4.2.2).

As mentioned above, LAP-CERR utilizes parallel beams for the dose calculation.

However, laser-driven proton beams exit the beam line with a certain divergence angle which is not included in the TPS. To analyze the impact of this approximation a Monte Carlo study was performed in the course of this thesis providing a comparison between parallel and divergent beams in a water phantom. For this analysis an existing Geant4 setup (version 9.3, [65]) was utilized and adapted to the requirements of this study. The setup as well as the results are shown and discussed in section 4.2.3.

4.2.1 Broad energy spectra

Dose calculation for broad energy spectra

The potential spectra which can be filtered with the beam line from the initial spectrum are still broader in energy than nearly monoenergetic beams (for which the dose calculation above is foreseen). Therefore, the dose calculation introduced in chapter 4.1.2 has to be modified. This is done by approximating the broad spectra coming from the beam line with a sum of thin Gaussians, i.e. by superimposing all involved energies [10] with their associated weight (i.e. contribution to the broad energy spectrum). These Gaussians have a pre-defined width (in range units, as the energies are converted into ranges in the TPS) of $\sigma_G = 0.05\,\mathrm{cm}$ and their centers have a pre-defined distance $\Delta d_{rad} = 2\sigma_G = 0.1\,\mathrm{cm}$. For these "monoenergetic" Gaussians the depth dose distribution D_{CAX} can be calculated as described in section 4.1.2. The final depth dose distribution $\overline{D_{CAX}}$ of the broad energy spectrum can then be computed by a superposition of the single depth dose distributions and their corresponding weight. Additionally one has to account for the depth dependent width $\sigma(d_{rad})$ of the single thin Gaussians. Since the Gaussians lie very close to each other one can use an approximated combined sigma $\overline{\sigma}(d_{rad})$ which can be calculated by a dose weighted sum of all $\sigma(d_{rad})$ at a given depth d_{rad} [10]. With this the dose to each point can be calculated for broad energy spectra:

$$D(x, y, d_{rad}) \approx \overline{D_{CAX}}(d_{rad}) \cdot \frac{1}{2\pi\overline{\sigma}^2(d_{rad})} \cdot exp(-\frac{x^2 + y^2}{2\overline{\sigma}^2(d_{rad})})$$

This dose calculation is done for every voxel i and each beam configuration j, however not all configurations j are committed to the optimizer. A pre-selection of curves is performed as mentioned before and only the selected configurations are stored in the D_{ij} matrix and are used as decision variables.

Clustering algorithm

Utilizing broad energy spectra, the high dose region of the depth dose distribution is not restricted to one depth, i.e one spot on the pencil beam, but more spots can be irradiated with a high dose. These spots are clustered axially, i.e. in depth along the pencil beam for the axial-layer-based dose delivery. Clustering refers to a grouping of spots together to be irradiated with one laser shot (of a broad energy spectrum)
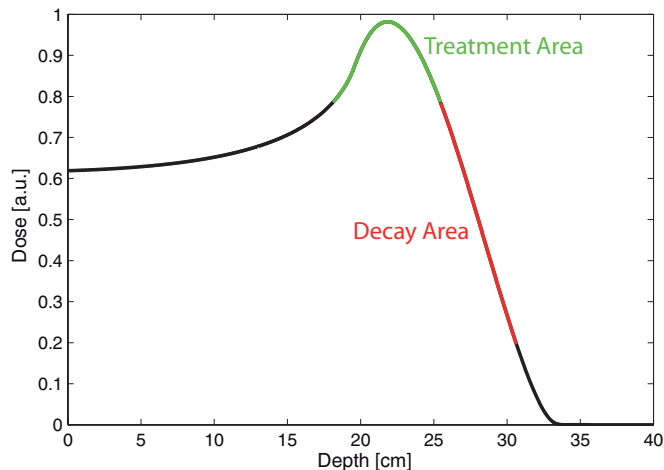
Figure 4.5: Graphical explanation of the treatment area and the decay area within one depth dose curve. All spots lying within the ranges of the treatment area (green) are clustered axially along one pencil beam. This cluster is utilized for the plan optimization when the decay area (red) lies completely within the target. If this is not the case, the clustering algorithm proceeds with the next narrower depth dose distribution. This sketch is similar to a figure from Schell [10].

and was developed by Schell [10, 66]. Depending on how broad an energy spectrum is, a different number of spots is clustered together. To avoid confusion, the word cluster is also utilized when only one spot is contained in the cluster, which actually means no clustering was performed and the spot is treated as a single spot because the depth dose curve is too narrow to treat more spots simultaneously.

For the clustering algorithm all depth dose distributions have to be computed beforehand. For all these depth dose curves, two areas are defined namely the treatment area and the decay area (see figure 4.5). In LAP-CERR the treatment area is defined as the part of the curve where the dose is higher than 80% of the maximum dose (highlighted in green in figure 4.5), however this value could be adapted if required. Depending on the width of the treatment area, all spots lying in these depths along one pencil beam are clustered in the first step. However, this is only meaningful if the target thickness is broader than or equal to this cluster length and if the distal dose decline does not reach into the region outside of the target. Therefore, in the second step, the decay area is analyzed. This decay area, illustrated in red in figure 4.5, is defined to be the distal region where the dose is 80% to 20% of the maximum dose (which can also be adapted). A cluster of a given treatment area is only built if the decay area lies completely within the target. This is mainly a failure criterion close to the distal edge of the target where it is very likely that the distal fall-off exceeds the target. If the broadest possible cluster cannot be built, the algorithm
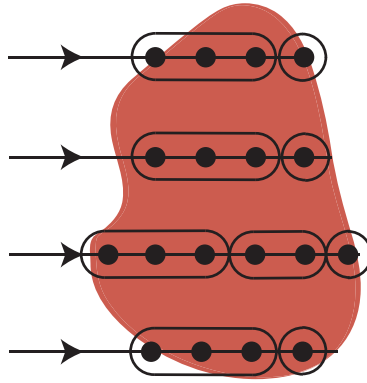
Figure 4.6: Sketch of axial clusters. Along the four pencil beams the spots which
           are clustered are surrounded by an ellipse highlighting that their are
           irradiated together within one laser shot. At the distal edges the clusters
           are smaller than at the proximal edges or in the middle of the target due
           to the broad dose fall-off of broad clusters.

tries for the next smaller cluster and so on. In summary, the algorithm tries to build
as broad clusters as possible inside the target and only decreases the cluster size if
the target extension is too small or if the distal dose fall-off extends to the normal
tissue (i.e. outside of the target). This leads to big clusters at the proximal target
edges and in the middle of the target and to very narrow clusters (up to only one
spot) at the distal edges as exemplary sketched in figure 4.6. The algorithm has to
be executed for each pencil beam individually. This increases the efficiency of the
utilized protons coming from the laser since only for few locations in the tumor the
energy bandwidths have to be reduced to nearly monoenergetic spectra.

After this clustering a fixed combination of several (non-overlapping) clusters with
their associated energy spectrum and contained proton number per bunch is com-
mitted to the optimizer where the respective weights contributing to the final 3D
dose distribution are optimized (referring to equation 4.1). This means, the clus-
ters are kept constant throughout the optimization process. As mentioned before,
the obtained weight is normalized to the dose delivered with one laser shot, i.e. a
weight of $\omega_j = 1$ denotes one full laser shot of the beam configuration j. To evaluate
the contribution of the various beam configurations to the whole treatment plan, a
new tool was implemented in LAP-CERR during this thesis which stores the exact
beam configuration for each column in the D_{ij} matrix. This allows for analyzing
the optimization results in terms of utilized cluster sizes.

4.2.2 High fluences

Since the particle number per proton bunch is pre-defined by the initial spectrum
and cannot be modulated over the short bunch duration a certain fixed dose is de-
livered to the target with such a bunch. This may compromise the plan quality for

high fluences per bunch as the delivered dose to a certain cluster may be higher than the required cluster dose per treatment fraction. One way to reduce the fluence, i.e. the number of particles delivered to a certain area, is spreading the beam with a fixed proton number over a wider area within the target. This can easily be realized in the utilized beam line by varying the magnetic field strength of the focusing quadrupoles leading to a variable beam width. In the TPS the beam width, i.e. FWHM is directly connected to the lateral spot distance and stays constant for one plan calculation. Certainly, variable beam widths within one plan would allow for more degrees of freedom, however, this was not integrated into LAP-CERR so far. The chosen beam width at patient entrance (FWHM converted into $\sigma_{0,x/y}$ assuming a Gaussian beam profile) not only determines the lateral spot distance but is utilized for the calculation of the lateral spread (see chapter 4.1.2) as well.

In conventional proton therapy the spot distance $\Delta = \Delta x = \Delta y$ is approximately $\Delta = \frac{1}{3} \cdot$FWHM (cf. [64]) leading to a dense spot grid and high quality proton plans. However, with the Matlab based LAP-CERR treatment plans with such a grid are computationally intensive and, therefore, Schell originally implemented a coarser spot grid. He derived a ratio of $\Delta/\sigma_0 = 2$ by setting the second derivative of the sum of two neighboring Gaussian beam profiles to zero at the central point yielding a homogeneous dose plateau between the two beams. With FWHM $= 2\sqrt{2ln(2)}\sigma \approx 2.3548\sigma$ this ratio converts into a spot distance of $\Delta = 0.85 \cdot$ FWHM. By evaluating the qualities of various plans with different distances depending on the beam widths the optimal distance-to-FWHM ratio g=Δ/FWHM can be found for the spot grid. Therefore, proton plans were generated for various initial FWHM for the same patient using the same optimization criteria for five different ratios:

- g = Δ/FWHM = 0.33
- g = Δ/FWHM = 0.45
- g = Δ/FWHM = 0.6
- g = Δ/FWHM = 0.725
- g = Δ/FWHM = 0.85

Figure 4.7 shows four exemplary resulting DVH comparisons for the target structure of the astrocytoma patient. The five analyzed ratios g are shown in different colors for the beam widths 0.7 cm, 1.0 cm, 1.5 cm and 2.0 cm respectively. A significant trend can be observed showing that all DVHs with a ratio of g=0.85 have a worsened quality compared to the other DVHs independent on the utilized FWHM. For a beam width of 0.7 cm as well as for 1.0 cm nearly no difference can be distinguished between the other analyzed ratios since they are all equally steep. In the lower plots of figure 4.7 it becomes apparent that the plan quality is decreased in general and that the single DVHs show a variable quality. For a FWHM of 1.5 cm the smallest ratios of g=0.33 and g=0.45 are relatively similar as well as the intermediate ratios
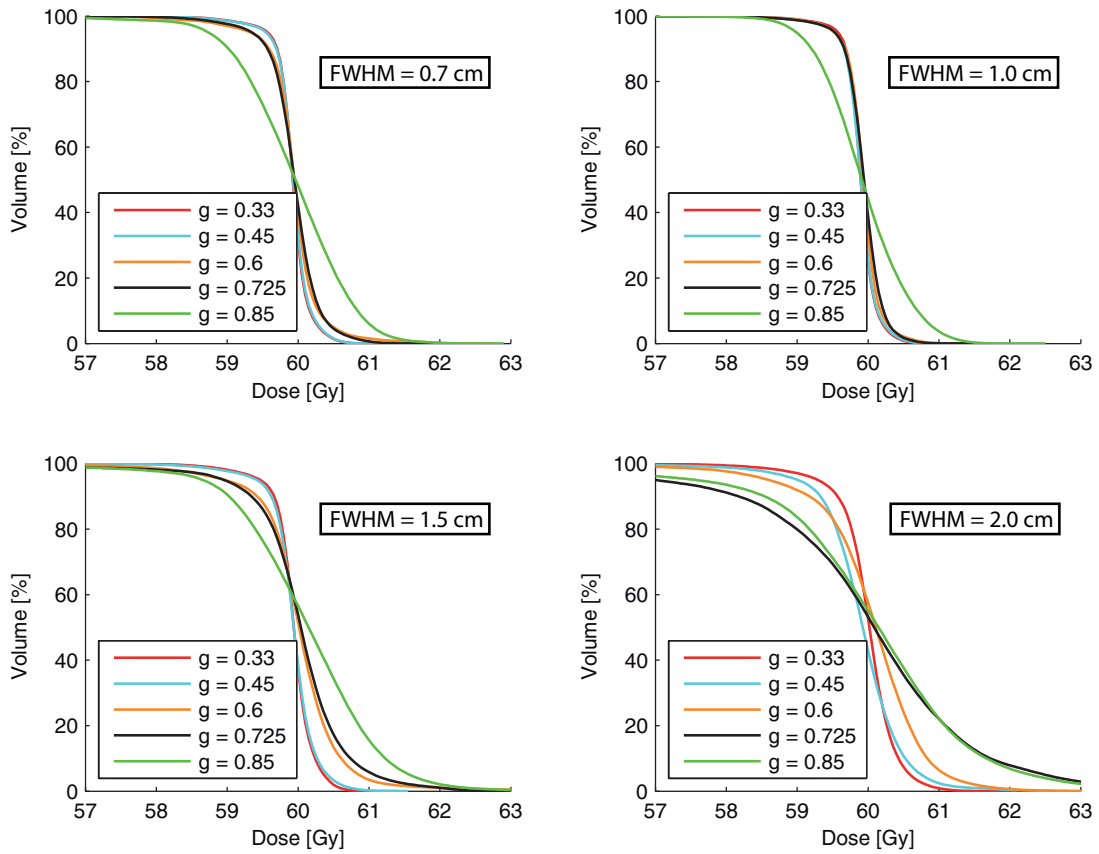
Figure 4.7: Target dose volume histograms for various plans with different beam
widths (FWHM) and different distance-to-FWHM ratios g. The ratio g
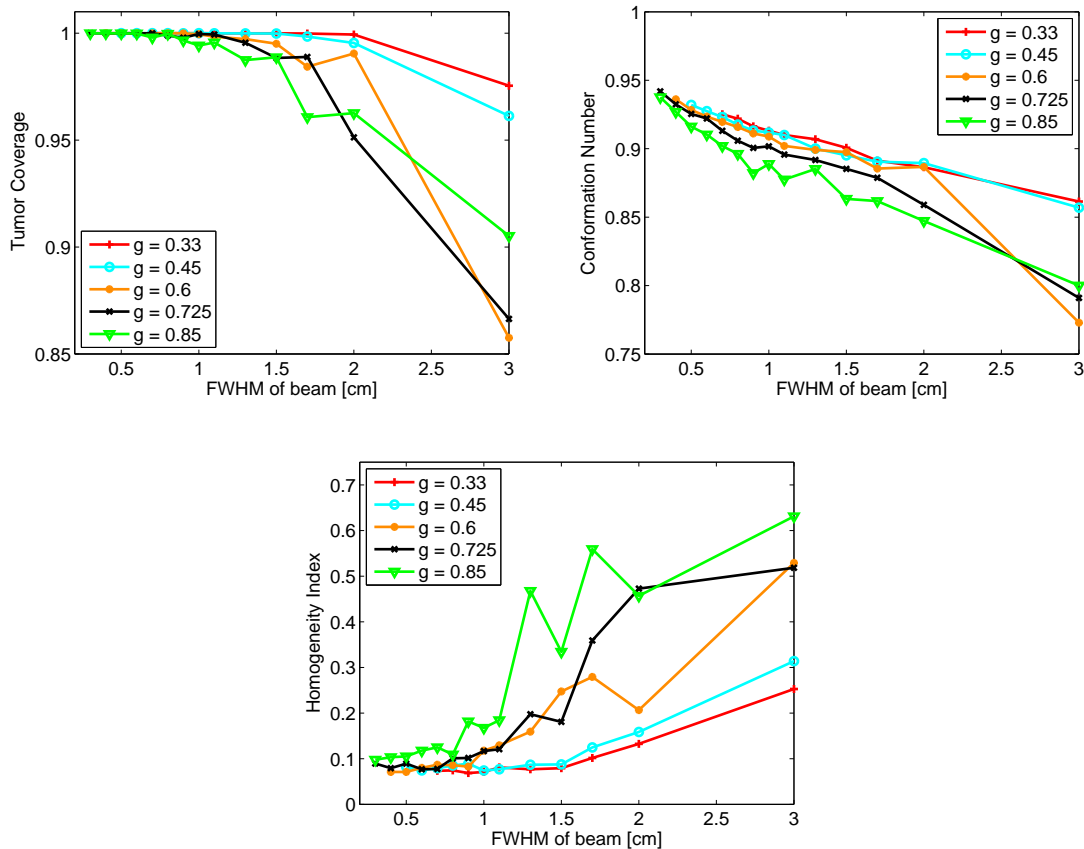represents the spot distance Δ divided by the FWHM of the beam.

Figure 4.8: Plan qualities for various beam widths and different distance-to-FWHM ratios g. The tumor coverage, the conformation number and the homogeneity are evaluated depending on the beam width (FWHM). The analyzed ratios are illustrated in different colors. The definitions of the evaluation criteria can be found in section 4.1.4.

with g=0.6 and g=0.725. Utilizing even larger beam widths (FWHM=2.0 cm) no DVH is comparable to another and only the one with g=0.33 or g=0.45 shows an acceptable steepness of the DVH curve.

The same plans can be evaluated by means of the previously introduced indices, the Tumor Coverage, the Conformation Number and the Homogeneity Index. The results are illustrated in figure 4.8. No significant difference can be found for the TC for FWHM < 0.75 cm. For larger beam widths the coverage stays closer to 100% for g=0.33 (red) and g=0.45 (cyan) and is worse for the other three ratios. Also for the conformation similar results can be observed. The differences in the CN index are not significant for narrow beams, however for larger beams, the best CN is obtained for g=0.33 and the worst for g=0.85 (green). Regarding the HI, there is nearly no difference between the first four ratios for FWHM < 0.75 cm but the plans

with g=0.85 do worse than all others even for these beam widths. For larger beams (FWHM > 0.75 cm) the same trend as discussed beforehand is visible where the ratios g=0.33 and g=0.45 lead to slightly better HI results than g=0.6 and g=0.725 and all four obtain better results than the plan with the ratio g=0.85.
In general, figure 4.8 indicates that the overall plan quality becomes worse for larger beam widths (especially for FWHM > 2 cm). This effect originates on the one hand from the decreased amount of spots inside the target due to the coarser grid. On the other hand, the quality is impaired due to the large PTV area which is irradiated simultaneously with one shot. This decreases the degrees of freedom for intensity modulation of the different PTV areas and, furthermore, leads to beam profiles exceeding the target edges.

All discussed evaluations stress that a spot distance of $\Delta = 0.85 \cdot$FWHM does not yield optimal plan qualities and should therefore not be used for treatment planning. When comparing the other four scenarios no large difference could be observed, however, with the combinations $\Delta = 0.33 \cdot$FWHM and $\Delta = 0.45 \cdot$FWHM slightly better results could be obtained. Since proton plans with more spots, i.e. denser grids take longer for the dose calculation and the optimization of the weights, a coarser grid may be preferred especially because many plan calculations are required for the treatment planning study in chapter 5. Hence, the best trade-off was chosen to be at $\Delta = 0.5 \cdot$FWHM. This fixed relation was implemented in LAP-CERR and utilized for all following plan calculations.

4.2.3 Divergency

The dose calculation in LAP-CERR bases on the approximation of parallel beams leaving the treatment head and entering the patient. However, due to the large initial divergence of the proton bunch coming from the laser target, the deliverable, filtered bunches exiting the beam line are divergent as well. The impact of this parallel-beam-approximation was investigated during this thesis by comparing the generated dose distributions and especially the lateral beam profiles of a parallel and a divergent beam with a Geant4 simulation (previously implemented by Kamp [65]). In this Monte Carlo calculation, the deposited energy per volume element was measured in three dimensions for a parallel and divergent beams. The order of magnitude of the relevant divergence angles was obtained by the particle tracking simulation of the compact gantry solution presented in chapter 3.2. An exemplary bunch with a nominal energy of 150 MeV (ranging from around 140 MeV to 160 MeV) was filtered in the beam line and its phase space was measured at the exit of the treatment nozzle. This measurement yielded polar angles of $0° \leq \Theta \leq 1°$ for all azimuthal angles between $0° \leq \varphi \leq 360°$. Hence, divergence angles in the order of $\Theta \leq 1°$ were investigated in the following as well as angles of $\Theta \leq 5°$ to compare the impact on the dose for two different divergency severities.
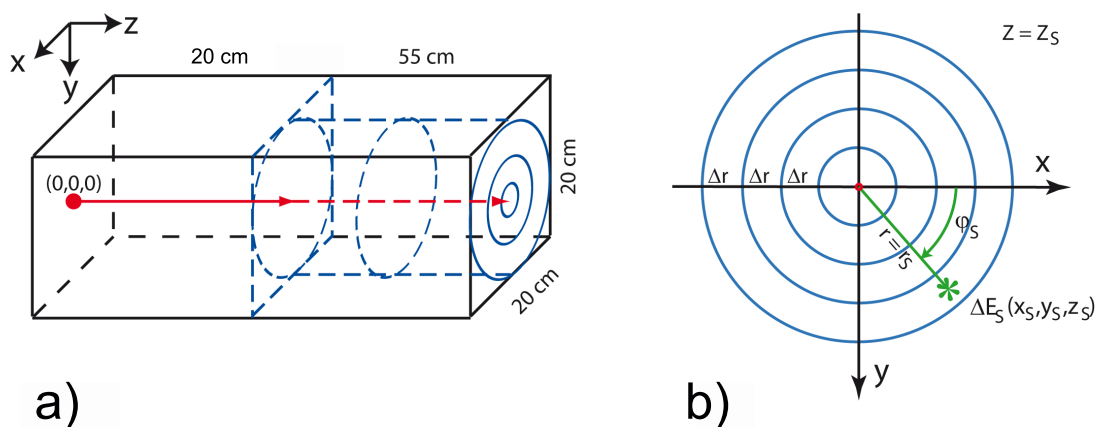
Figure 4.9: Geant4 simulation geometry. In a) the whole "world" is illustrated with the proton source (red) at the very left directed towards the cylindrical water phantom (blue) after a 20 cm air gap. The cylinder is divided in slice of thickness Δz. Figure b) depicts one of these slices with their ring geometry ($\Delta r = 0.01$ cm). The deposited energy per step $\Delta E_S(x_S, y_S, z_S)$ is stored in the respective bin (r_S, z_S) (green) depending on the radial distance to the central axis (red). These figures were taken from Kamp [65].

The phase space data generated with the particle tracker could not be utilized for the Monte Carlo simulation directly since too few protons have been tracked. Thus, a beam similar to this filtered bunch was implemented in Geant4. For simplicity, one million monoenergetic protons of 150 MeV were sent from the source at one end of the Geant4 "world" towards a water phantom as illustrated in figure 4.9a). The initial beam width of the circular beam was set to $\sigma = \sigma_x = \sigma_y = 1.40$ cm. Since the polar angle distribution of the tracked bunch could not be represented well with the phase space information due to the low proton number, an isotropic distribution was assumed for this study even if this probably does not represent the realistic angular distribution emitted from the laser target. Therefore, three different isotropically distributed polar angles were simulated, namely $\Theta = 0°$, $\Theta \leq 1°$ and $\Theta \leq 5°$ to compare a parallel beam to two different severities of divergency. As shown in figure 4.9a) the beam passes an air gap of 20 cm length (simulating the distance of the patient to the treatment head) and hits the water phantom afterwards where the deposited energy, i.e. the dose is measured. This water phantom has a radial symmetric cylindrical geometry with the central axis being the z-axis of the coordinate system. The cylinder is divided into slice with a thickness of $\Delta z = 0.01$ cm in depth and each slice (in the x-y-plane) is divided into rings of thickness $\Delta r = 0.01$ cm as depicted in figure 4.9b). Certainly, the innermost area is a circle with radius Δr. When an energy ΔE_S is deposited at a point (x_S, y_S, z_S) in one calculation step (compare to the green star in figure 4.9b)) this point is converted
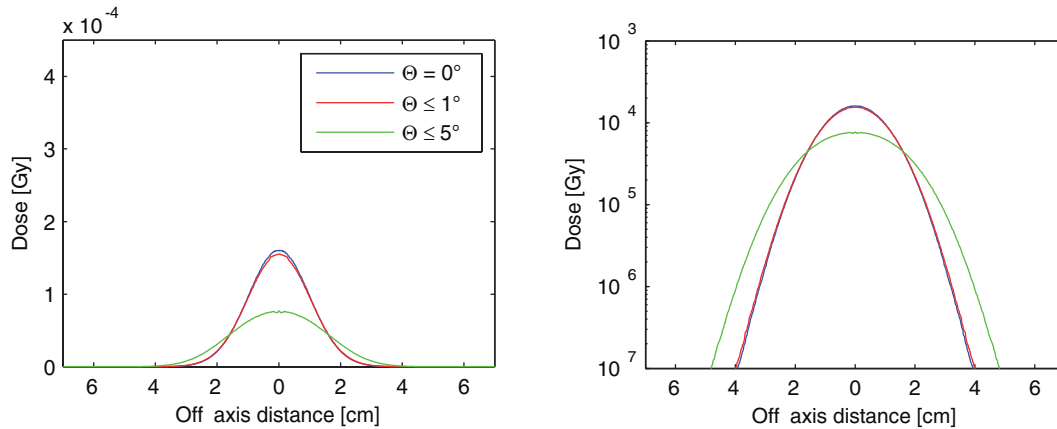
Figure 4.10: Lateral beam width comparison in a water depth of $1\,\mathrm{cm}$. The Gaussian
beam profiles are shown on a linear (left) and a logorithmic scale (right)
for a parallel beam (blue) and two divergent beams with an opening
angle of 1° (red) and an opening angle of 5°. The initial beam width
of all three beams is $\sigma_0{=}1.40\,\mathrm{cm}$.

into polar coordinates for the respective depth z_S and the cumulative deposited
energy is stored in the respective bin (r_S, z_S). The polar angle φ_S is not stored since
for the analysis of the lateral beam profile only the radial distance to the central axis
is relevant. With a simple calculation the measured energy in eV can be converted
into a dose (in Gy) in water

$$D(r,z)[Gy] = \frac{\Delta E_S}{\Delta m} = \frac{\Delta E_S[eV] \cdot 10^6 \cdot 1.6022 \cdot 10^{-19}}{\Delta V_{Ring}[cm^3] \cdot 10^{-3}[kg/cm^3]}$$

Figure 4.10 shows the lateral beam shapes of all three beams in $1\,\mathrm{cm}$ water depth
on a linear dose scale on the left and on a logarithmic scale on the right. When
comparing the parallel beam to the beam with a divergence angle of up to 1° nearly
no difference can be observed for the lateral beam profile. Both beams (illustrated
in blue and red) have a width of $\sigma_{0°} = 1.40\,\mathrm{cm}$ and $\sigma_{1°} = 1.43\,\mathrm{cm}$ which is close to
the original beam width at the source of $\sigma_0 = 1.40\,\mathrm{cm}$. Additionally, the dose on
the central axis of the divergent beam is similar compared to the central axis dose
of the parallel beam with a difference of about 3%. However, the beam profile for
angles $\leq 5°$ (green) shows a significant broader lateral extension ($\sigma_{5°}{=}2.10\,\mathrm{cm}$) and,
therefore, a significantly decreased dose on the central axis (approximately 50% of
the dose for a parallel beam). The difference in the width of the beam becomes even
more apparent in the logarithmic plot of figure 4.10. The broadening of the lateral
beam profile originates in this case nearly only from the geometrical broadening of
a divergent beam and insignificantly from the scattering of the beam in the $20\,\mathrm{cm}$
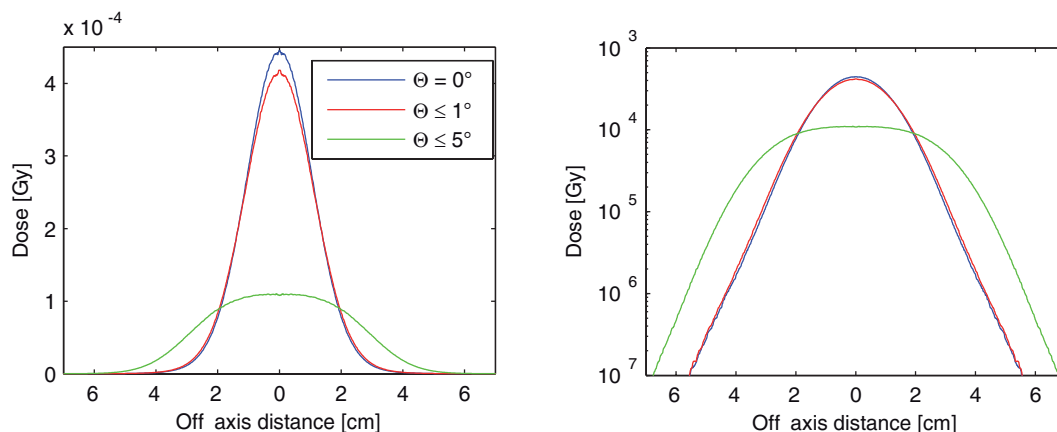air cavity in front of the water phantom.

Figure 4.11: Lateral beam width comparison in a water depth of $15\,\text{cm}$. The Gaussian beam profiles are shown on a linear (left) and a logarithmic scale (right) for a parallel beam (blue) and two divergent beams with an opening angle of 1° (red) and an opening angle of 5°. The initial beam width of all three beams is $\sigma_0 = 1.40\,\text{cm}$.

Figure 4.11 shows the same comparison in a depth of $15\,\text{cm}$. Certainly, the deposited dose is higher compared to figure 4.10 because these beam profiles were measured shortly in front of the Bragg peak. Moreover, the beams are slightly broader in general due to the Multiple Coulomb scattering inside the water phantom. The parallel beam has broadened to a width of $\sigma_{0°} = 1.52\,\text{cm}$ and the beam with angles of $\Theta \leq 1°$ to $\sigma_{1°} = 1.58\,\text{cm}$. Again, these beam profiles are comparable but the dose differences on the central axis increased to approximately 7%. Comparing the lateral profile for the most divergent beam with $\Theta \leq 5°$ to the parallel beam the differences are even more pronounced than before. The mentioned divergent beam is much broader and significantly different compared to the less divergent beam or the parallel beam. In this case, the lateral profile is not even a perfect Gaussian (nor a parabola in the logarithmic figure). Hence, the dose on the central axis is not comparable at all to the parallel beam.

These simulations demonstrated that the lateral beam profile of a divergent beam with $\Theta \leq 1°$ can be approximated well with the lateral profile of a parallel beam independent on the depth of the measurement. However, the dose on the central axis differs for both cases. Close to the entrance region of the beam these deviations are small, however, close to the Bragg peak they become relevant. Therefore, only in a first approximation the divergent beam can be handled as a parallel beam in the TPS. This holds only since the polar angles obtained by the particle tracking simulation are smaller than 1°. It was shown that for larger divergences even the first approximation fails and beams with polar angles of $\Theta \leq 5°$ cannot be approximated with parallel beams anymore.

Concerning the whole divergency study it has to be mentioned that more energies would have to be tested and not just one to investigate the difference of the impact on the dose for various energies. This could clarify whether all energies can be treated equally or if a low or a high energy beam is affected more by the divergency. Furthermore, the beam exiting the simulated beam line has a divergency which depends on the energy. This means, each energy contained in the filtered spectrum exits the nozzle with another polar angle. Therefore, in a future version of the TPS, the simulated phase space information should be imported and the divergency of the delivered bunches should be included into the dose calculation. However, for the following treatment planning study analyzing only the feasibility of laser-driven proton therapy in general it was decided to not implement divergent beams and approximate the filtered spectra with parallel beams.

5

A treatment planning study using a compact laser-driven proton gantry

Using the compact proton gantry introduced in chapter 3.2 a treatment planning study was performed to investigate the feasibility and limitations of the suggested design and to ascertain whether laser-driven radiotherapy in general can yield clinically relevant dose distributions. In this case, clinically relevant refers to a high quality of the generated dose distributions as well as to the time such a treatment plan would take to be delivered. On real patient data multiple laser-driven proton plans were calculated with the TPS presented in the previous chapter. These plans were analyzed with respect to dosimetric quality and required delivery time depending on different initial proton numbers contained in the laser-produced spectrum and various possible lateral beam widths. The proton number per bunch is critical since it is limited by a lower and an upper bound. If the proton number per bunch is low many laser shots are required to deliver the desired dose and, depending on the repetition rate of the system, this may cause an unacceptable overall delivery time. However, since the laser only can deliver full proton bunches a high initial proton number degrades the plan quality due to the high delivered dose per bunch. When spreading the beam over a wider area, this upper bound may be shifted towards higher proton numbers if this, in turn, does not degrade the plan quality again. The proton number could be decreased within the beam line, however, this would result in an undesirable extra amount of dumped particles. Even if this study does not deal with the number of blocked protons the bunches are tried to be utilized as efficient as possible. Therefore, proton plans were generated with LAP-CERR by applying the axial-layer-based delivery. The required laser shot number for one plan is directly calculated in the TPS and the associated delivery time can be estimated by assuming an optimistic repetition rate of the laser system of 10 Hz. For the whole study the absolute maximum acceptable treatment time was set to 30 min which is comparable to long photon treatment plans but by far longer than conventional proton delivery times. The clinical relevance and the critical parameters were investigated for a delivery of integer laser shots as well as for an intensity modulation from shot to shot. Additionally, the influence of the dose distributions originating from shot-to-shot fluctuations in the proton number was evaluated.

5.1 Bunch properties

The particle tracking simulation performed for the compact laser-driven proton gantry (introduced in chapter 3.2) relies on a measured TNSA spectrum which was scaled to therapy-relevant energies by conserving the total proton number in the bunch [53]. A fit of this scaled TNSA spectrum as well as fits for all spectra which can be produced with this beam line are taken similar to the ones presented in the paper by Masood *et al.* [53] and were imported into the TPS. The energy spectrum coming from the laser target into the beam line, from now on called "initial spectrum" can be represented by an exponentially decaying function:

$$\frac{dN}{dE}_{initial} = 1 \cdot 10^{10} MeV^{-1} \cdot e^{-0.0241 \cdot E/MeV}$$

In this equation dN/dE constitutes the proton number in the energy bin E of width dE. Assuming the initial spectrum to range from 0 MeV to a cut-off energy of 300 MeV this spectrum contains $N_0 = \int_{0\,MeV}^{300\,MeV} \frac{dN}{dE_{initial}} dE = 4.15 \cdot 10^{11}$ protons (in the following called "initial proton number"). The Integrated Shot-to-shot Energy Selection System in the gantry beam line filters desired smaller, parabolically approximated spectra that are then guided to the patient (cf. figure 5.1). These parabolic spectra can be centered on variable nominal energies E_{nom} ranging from 50 MeV to 250 MeV in 1 MeV steps and can have energy bandwidths ($\Delta E/E_{nom} = b$, measured on the energy axis, i.e. for dN/dE=0) from 4% to 24% in steps of 2%. With a transport efficiency of the whole beam line of $\eta = 22\%$ (referring to the transported proton number of the nominal energy: $\eta = N_{filtered}(E_{nom})/N_{initial}(E_{nom})$) the shape of the filtered energy spectrum as well as the contained proton number can be calculated:

$$\frac{dN}{dE}_{filtered} = a \cdot (E - E_{nom})^2 + \eta \cdot \frac{dN}{dE}_{initial}\bigg|_{E=E_{nom}}$$

with

$$a = \frac{-4\eta \frac{dN}{dE}_{initial}\big|_{E=E_{nom}}}{E_{nom}^2 \cdot b^2}$$

and

$$N_{filtered} = \int_{0\,MeV}^{300\,MeV} \frac{dN}{dE}_{filtered} dE$$

Six exemplary spectra produced within the beam line are illustrated in figure 5.1 for three different nominal energies and the 4% and 24% widths, respectively. Additional to the filtered spectra the initial spectrum which is sent into the beam line is shown. The offset between the height of each spectrum at its nominal energy to the initial spectrum corresponds to the transport efficiency of the beam line of $\eta = 22\%$.
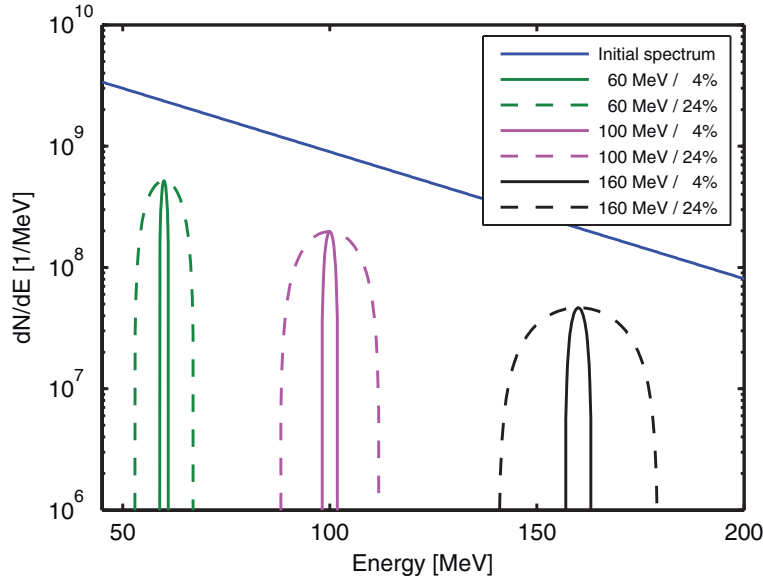
Figure 5.1: Exemplary spectra that can be filtered out from the initial TNSA proton spectrum (blue) with the Integrated Shot-to-shot Energy Selection System in the beam line. For each of the three nominal energies the minimum (4%) and the maximum (24%) energy width is shown.

To analyze the feasibility of such an initial energy spectrum for radiotherapy purposes, the initial proton number N_0 was varied from plan to plan. Therewith, the range of this proton number per bunch leading to high quality treatment plans can be investigated and a benchmark can be established of how many protons future laser-accelerated bunches (of the given type) should provide. Therefore, the shape of the initial spectrum was kept constant and the initial proton number was degraded successively from the anticipated $N_0 = 4.15 \cdot 10^{11}$ down to $N_0 = 10^7$.
Moreover, the beam width was changed from plan to plan to investigate a wider range of possible scenarios. Therefore, the widths were varied between FWHM=0.5 cm up to FWHM=6 cm. The increase of lateral width may be helpful in the case of a high fluence per bunch as discussed in section 4.2.2.

For one plan calculation, all 2211 spectra which can be generated with the utilized gantry (201 nominal energies each with 11 energy widths) are imported into the TPS with their corresponding proton number (depending on the initial proton number) and the respective lateral beam widths serving as a database for the dose calculation. When energies lower than 50 MeV are required for dose delivery (i.e. for spots or clusters that are close to the skin of the patient in a depth smaller than approximately 2 cm), the TPS integrates a virtual range shifter of required thickness into the beam path. This leads to a shift of the depth dose curve and the depth dependent beam width to lower depths as if a lower energy would have been used [10].

5.2 Considered patients and dosimetric evaluation

All plans were calculated on CT images of patients previously treated with photons
in the Department of Radiation Oncology, TU München. To cover a majority of
clinical scenarios three dose fractionation schemes were chosen to be studied on two
anatomies. An astrocytoma patient (figure 5.2a)) with a PTV of $274.4\,cm^3$ was
irradiated with $2\,Gy$ per fraction as a standard fractionation. The plan consisted
of two coplanar beams at an angle of $50°$ and $120°$ respectively. Furthermore, a
hypofractionation with $5\,Gy$ per fraction as well as a stereotactic radiosurgery ($24\,Gy$
at isocenter, $20\,Gy$ isodose enclosing PTV, delivered in one fraction) was examined
for another anatomy. Therefore, a metastasis patient (figure 5.2b)) was chosen with
a PTV of $3.9\,cm^3$ to be irradiated with two coplanar beams from $45°$ and $90°$. For
both anatomies and all plans, two beam directions were utilized to increase the
degrees of freedom for the dose delivery compared to one single beam direction and,
hence, to increase the dose coverage and conformity to the target structure. More
beam directions may improve the dosimetric aspects even more, however, the integral
dose is raised by adding additional angles and the required laser shot number will
probably be increased as well. Therefore, two angles were chosen reflecting a clinical
proton treatment plan having generally two to three beam directions [67]. Both
beams were optimized simultaneously as in the conventional IMPT optimization.
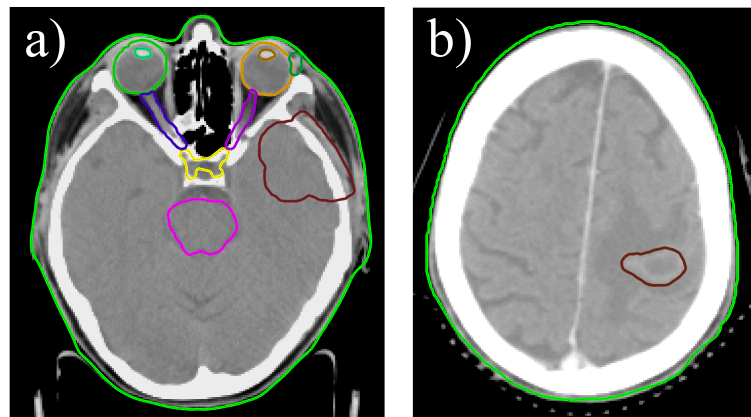
Figure 5.2: Transversal view of both patients used in the following studies including
the PTV structure (dark red). a) shows the astrocytoma patient with
OARs close to the PTV like the brain stem (magenta) and the left optical
nerve (purple) and b) displays the metastasis patient.

For all plans discussed in this chapter particular structures were chosen to be opti-
mized and, hence, contribute to the cost function in the TPS. For the astrocytoma
patient these structures are the target, the brain stem and the left optical nerve
and for the metastasis case only the PTV was chosen. The other OARs were not
included since they receive a low dose anyway. Moreover, more optimized structures
lead to longer computation times and may worsen the dose in the target as not all

	TC	CN	$D_{min}(1\,cm^3)$	$D_{max}(1\,cm^3)$
green	$\geq 98\%$	$\geq 87\%$	$\geq 95\%\cdot D_{pres}$	$\leq 105\%\cdot D_{pres}$
yellow	$\geq 95\%$	$\geq 82\%$	$\geq 92.5\%\cdot D_{pres}$	$\leq 107.5\%\cdot D_{pres}$
red	$< 95\%$	$< 82\%$	$< 92.5\%\cdot D_{pres}$	$> 107.5\%\cdot D_{pres}$

Table 5.1: Evaluation criteria tumor coverage (TC), conformation number (CN) and minimum (D_{min}) and maximum (D_{max}) dose of $1\,cm^3$ for the standard and hypofractionation. The minimum and maximum dose criteria depend on the prescribed dose D_{pres}. The categories green, yellow and red characterize the respective plan quality.

prescriptions can be fulfilled by the optimizer. Additionally to the delineated OARs illustrated in different colors in figure 5.2, a margin around the PTV was created for each patient to control and down-regulate the dose outside the PTV close to the target edges. Such a margin was generated by extending the whole target by the given length in three dimensions and by subtracting the PTV from this generated volume. For the large PTV of the astrocytoma patient the margin was chosen to be $1\,cm$ and for the small target of the metastasis a smaller margin of $0.5\,cm$ was created (both are not shown in figure 5.2). The assigned penalty factors for good optimization results are $p_{PTV} = 10$, $p_{Margin} = 0.006$, $p_{brainstem} = 0.003$ and $p_{leftopticalnerve} = 0.003$ for the astrocytoma patient and $p_{PTV} = 10$ and $p_{Margin} = 0.02$ for the metastasis.

Due to the large amount of generated proton plans not every plan and dose distribution could be analyzed individually. Therefore, depending on the fractionation scheme, selected dosimetric parameters were calculated and evaluated automatically. Depending on the results of these parameters the plans were grouped into three categories using a "traffic light system". This system indicates the clinical relevance of the obtained dose distributions. For instance, all "green" plans are of quite good quality and, hence, are clinically interesting. The "yellow" plans would need a detailed plan review to be categorized and the "red" plans are of no interest due to their bad quality. If only one dosimetric parameter from various evaluation criteria is violated the plan relegates to the next category. This color system enables an overview of many parameters at once together with the resulting overall plan quality. For the standard fractionation and the hypofractionation the evaluation bases on table 5.1. The analyzed dosimetric parameters are the Tumor Coverage (TC), the Conformation Number (CN) and the minimum ($D_{min}(1\,cm^3)$) and the maximum dose ($D_{max}(1\,cm^3)$) delivered to at least $1\,cm^3$ of the PTV (all parameters have been introduced in section 4.1.4). Due to their distinct clinical prescription in radiosurgery, different values have to be chosen. For these plans, the absolute maximum dose was evaluated as well as the volume inside the PTV receiving less than $20\,Gy$ and the volume within the $0.5\,cm$ margin around the PTV receiving more than $20\,Gy$ (see table 5.2). The boundary values of the dosimetric parameters for all categories were chosen in compliance with a detailed review of single plans. However, it should be

	D_{max}(Margin)	$V_{20\,Gy}$ (Margin)	$V_{20\,Gy}$ (PTV)
green	$\leq 22\,\text{Gy}$	$\leq 10\%$	$\geq 97\ \%$
yellow	$\leq 23\,\text{Gy}$	$\leq 12\%$	$\geq 95\ \%$
red	$> 23\,\text{Gy}$	$> 12\%$	$< 95\%$

Table 5.2: Evaluation criteria for the stereotactic radiosurgery. For the 0.5 cm margin around the PTV the absolute maximum dose and the volume receiving more than 20 Gy are evaluated. Within the PTV the volume percentage receiving less than 20 Gy is evaluated. The categories green, yellow and red characterize the respective plan quality.

mentioned that three or four parameters cannot represent the exact plan quality, especially when only one parameter degrades the treatment plan quality due to its decimal part for example. This is especially true since all evaluated parameters are rounded to two decimal points (with a floating point representation of the percentages of TC and CN). To enable a reliable evaluation the green category was designed to include only plans with a good quality and all plans close to the same quality are sorted into the yellow category. By this, one avoids a sharp distinction between acceptable and unacceptable plans and ensures that the green plans are clinically relevant even without a detailed analysis of the 3D dose.

5.3 Performed studies

To investigate the feasibility and limitations of laser-driven proton therapy with the chosen design three types of studies were performed. The key question was whether good proton plans could be achieved under given conditions and how long the treatment times would be. To assess the limits, the influence of the initial proton number was analyzed as well as fluctuations within this number. For this purpose the D_{ij} matrix was calculated as explained in chapter 4 for the given beam configurations and the axial-layer-based dose delivery scheme, depending on the particular initial proton number. The corresponding weights were optimized and post-processed before the final dose is calculated and evaluated. This post-processing is necessary since the optimizer calculates floating point weights which would correspond to undeliverable percentages of full shots like for instance 87.6% of a shot for $\omega_j = 0.876$. Neither the laser nor the beam line can deliver any floating point number and, therefore, the weights have to be rounded to the next deliverable value. For each study, this post-processing step is explained in the respective section. Afterwards, no additional optimization is performed and the specific adapted weights ω_j are multiplied with the D_{ij} matrix (see equation 4.1) to obtain the final 3D dose distribution. Then, the dosimetric quality of the generated plans was evaluated as described in section 5.2.

5.3.1 Integer shots

In the first study, the gantry design was used as presented by Masood *et al.* [53]. The laser hits the target and the bunch of protons is transported through the beam line. Since only integer shots can be performed with the laser and no device inside the beam line can modulate the amount of protons per bunch the proton number contained in the filtered outgoing spectrum is only dependent on the initial proton number (cf. section 5.1). Certainly, the proton number per delivered bunch is changed by varying the energy bandwidth for instance, however, a modulation of the proton number in this context refers to a variable particle number per bunch with the same energy settings. This means, for a given nominal energy and a fixed energy width the proton number is constant and cannot be decreased nor modulated within the beam line. Since the weights are normalized to a full bunch of the respective configuration, the scenario can be realized in the TPS by rounding all optimized weights in the post-processing step to the next integer. Thus, a weight of value $\omega_j = 1$ representing one full shot remains one full shot after the post-processing, but a weight of value $\omega_j = 0.5$ representing half of a shot is rounded to a full shot. Certainly, this changes the originally optimized 3D dose, however, the beam line is not designed to deliver any desired part of a full proton bunch and, therefore, this procedure is essential to obtain deliverable doses. To explore a wide range of possibilities and investigate the impact of this rounding procedure on the final dose distribution the beam widths as well as the initial proton number per bunch were varied from plan to plan. The beam width was increased from $0.5\,\mathrm{cm}$ FWHM to $6.0\,\mathrm{cm}$ FWHM and the initial proton number was regulated, as explained above, from 10^7 to $4.15 \cdot 10^{11}$. Since the weights correspond directly to the required laser shots of the certain beam configurations, the sum of all weights $N_{shots} = \Sigma_j \omega_j$ determines the overall laser shot number required for the whole plan to be delivered. For each plan this shot number is computed and evaluated.

5.3.2 Intensity modulation from shot to shot

In the second study, an additional pinhole collimator was added to the beam line to modulate the intensity (i.e. proton number) from shot to shot. The collimator was introduced behind the capturing solenoid in front of the first 90° bending magnet. For various circular apertures ranging from $1\,\mathrm{mm}$ radius to $15\,\mathrm{mm}$ radius the exiting intensity has been simulated for different nominal energies and energy widths. By choosing the appropriate aperture of this collimator it was found that the intensity of a bunch can be degraded on a linear scale from 100% to 10% in steps of 10%. Using the intensity modulation from shot to shot the difference to the integer shot scenario was studied for a fixed FWHM of $1\,\mathrm{cm}$ (to leave out one additional degree of freedom) depending on the number of intensity levels and the associated intensity values. The study was performed for the standard fractionation and the hypofractionation to determine dependencies on the dose per fraction and the target size. Therefore, the optimized weights were rounded to the next possible combination of

intensity values in the TPS. For instance, with an intensity level combination of 1, 0.5 and 0.1 (meaning shots can contain either 100%, 50% or 10% of the initial proton number) a weight of 2.84 would be delivered with two shots of 100%, one shot of 50% and three shots of 10%, leading to a delivered weight of 2.8 in six shots. This, obviously, leads to an improved dose but elongated delivery time compared to the integer shot delivery where 2.84 would be rounded to 3.0 and delivered in three shots.

The algorithm choosing the appropriate intensity levels that constitute a certain weight ω_j was developed during this thesis. For each possible intensity level, starting from the largest one, it is evaluated how often the respective intensity value fits into the weight ω_j. The contribution of the respective level is stored and the remaining intensity portion is processed with the next lower intensity level. For instance with intensity levels of 1, 0.5 and 0.1 a weight of 3.452 is processed as follows: The 100% intensity level fits three times into $\omega_j = 3.452$. Hence, the composition 3x1 is stored and the algorithm continues with the remaining weight $\omega_j = 0.452$. The 50% level does not fit into $\omega_j = 0.452$. Therefore, the combination 0x0.5 is saved and the next intensity is analyzed. The 0.1 level fits four times into $\omega_j = 0.452$. However, concerning the deviation to the original weight, the better choice would be to deliver the 10% intensity five times. Therefore, the algorithm evaluates the deviation to the original weight and increases the last intensity level by one shot if it decreases the error of the post-processed weight. This procedure leads to a weight of $\omega_j = 3.5$ delivered with three shots of 100% and five shots of 10%. Now, exactly the same weight could be delivered with four shots in total, three of 100% and one of 50% with the given level combination. Hence, the algorithm analyzes additionally whether the intensity portion delivered by the last level can be substituted by the next to last level with less shots. Then, finally the original weight of $\omega_j = 3.452$ is approximated by $\omega_j = 3.5$ and delivered with four shots. It should be mentioned that the post-processing algorithm for the intensity modulation can be either designed to find a deliverable weight which has the least error compared to the original weight or to find the deliverable weight with the least laser shots. The implemented algorithm aims in finding the composition of intensity levels which represents the original weight calculated by the optimizer as close as possible. In extrem cases this may lead to a high laser shot number delivering the optimized weight exactly. One example would be the delivery of the weight $\omega_j = 0.9$ with the intensity levels 1 and 0.1. For this scenario, the algorithm will come up with the solution to deliver the weight of $\omega_j = 0.9$ in nine shots. Depending on the goal of the performed study the delivery of the weight $\omega_j = 1$ in one shot might be the preferred solution since the deviation of the delivered weight to the optimized weight would only be 0.1. This demonstrates that the implemented algorithm leaves room for improvement, depending on the user requirements.

It should also be mentioned that such a down-regulating device implies an extra amount of protons to be dumped since, for instance, each bunch may require a blocking of up to 90% of its intensity. However, the modulation from shot to shot

may increase the plan quality as the optimized weights are delivered more exactly. Since the number of blocked protons is high anyway for an initial TNSA spectrum and since this thesis does not focus on the produced secondary radiation, the additional amount of dumped protons is not analyzed in the course of this study. By down-regulating the initial proton number inside the beam line to for example 10% a ten times higher initial proton number can be handled and yields good plan qualities. Therefore, this study does not aim mainly in increasing the possible range of the initial proton number but rather in increasing the clinical relevance of the produced plans.

5.3.3 Shot-to-shot fluctuations

The third analysis copes with the fluctuations in the proton bunch production from shot to shot and their influence on the dose distribution. Therefore, the shapes of the filtered spectra are assumed to be constant. This assumption is reasonable since the shape of the filtered spectra only depend on the beam line setup and hardly on the shape of the initial TNSA spectrum. Only if the shape of the initial spectrum would change significantly this would influence the shapes of the filtered spectra. Examples could be if some energies would not be present at all or if the cut-off energy would be shifted to lower energies. A variation in the inclination of the initial spectrum or fluctuations of the initial proton number would only affect the proton number contained in the filtered spectra. Therefore, the filtered proton numbers were chosen to be subject to random fluctuations in this study. Three severities of fluctuations were investigated, namely $\pm$ 100% which is the current status of single shot experiments, $\pm$ 30% which was measured by Kraft *et al.* [68] for shot-to-shot dose variations and $\pm$ 10% as a potential future condition. To simulate these fluctuations and to analyze the impact on the 3D dose the weights ω_j were randomly changed in the post-processing step. This weight variation corresponds to a variation in the proton number since the weights are normalized to the proton number per bunch of the respective beam configuration j. When multiplying the post-processed weights with the D_{ij} matrix, the calculated dose distribution represents the plan underlying shot-to-shot fluctuations in the specified range. This study was performed for the integer shot delivery described in section 5.3.1. Therefore, the post-processing of the weights starts with rounding all ω_j to the next integer. For each shot a random number is chosen from uniformly distributed values in the given range, i.e. $\pm$ 10%, $\pm$ 30% or $\pm$ 100%. For instance, a weight of $\omega_j = 2.96$ is rounded to $\omega_j = 3$ and these three shots are randomly assigned to deliver 115.7% in the first shot, 72.8% in the second shot and 94.3% in the third shot (for a fluctuation of $\pm$ 30%). The sum of these shots underlying proton number fluctuations lead to a delivered weight of $\omega_j = 2.828$ instead of the planned $\omega_j = 3$. The influence on the dose was analyzed for three exemplary plans, one with a high, one with a moderate and one with a low initial proton number and a fixed FWHM for both patient geometries. One hundred plans underlying shot-to-shot fluctuations were generated and the dosimetric parameters were studied and compared to the reference plan without fluctuations.

5.4 Results

5.4.1 Integer shots

For all three fractionation scenarios the resulting proton plans are presented here in overview plots. Only for the first patient all studied FWHM up to 6.0 cm are shown for a wide range of the initial proton number N_0, however not up to the highest analyzed number $N_0 = 4.15 \cdot 10^{11}$ since only plans of the red category are obtained in that region. For the metastasis patient, only the interesting N_0 and FWHM are shown and discussed. The manageable range of the critical initial proton number per bunch is determined by the maximum delivery time of 30 min (lower bound) and by plans of good quality (green category) with the highest number of initial protons per bunch.
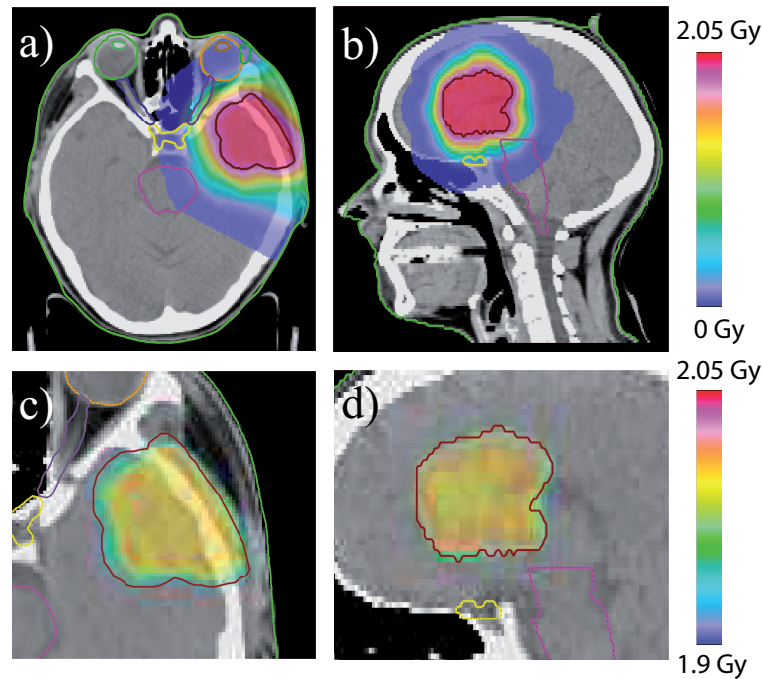
Figure 5.3: Dose distribution computed on the astrocytoma patient. In a) and c) a transversal view and in b) and d) a sagittal view illustrates the dose delivered per fraction (plan parameters: FWHM = 1.25 cm, $N_0 = 4 \cdot 10^7$, $6 \cdot 10^5$ laser shots). a) and b) show the whole dose range whereas c) and d) show the clinically relevant dose range for the PTV (dark red).

A representative, clinically relevant ("green") dose distribution of the astrocytoma patient (prescribed dose: D_{pres}=2 Gy) is given in figure 5.3. This plan bases on an initial proton number of $N_0 = 4 \cdot 10^7$ and would be delivered with $6 \cdot 10^5$ laser shots. The yielded dosimetric parameters are TC=100%, CN=90%, D_{min}=1.94 Gy (i.e. 97% of D_{pres}) and D_{max}=2.03 Gy (i.e. 101.5% of D_{pres}). Figure 5.3a) and b)
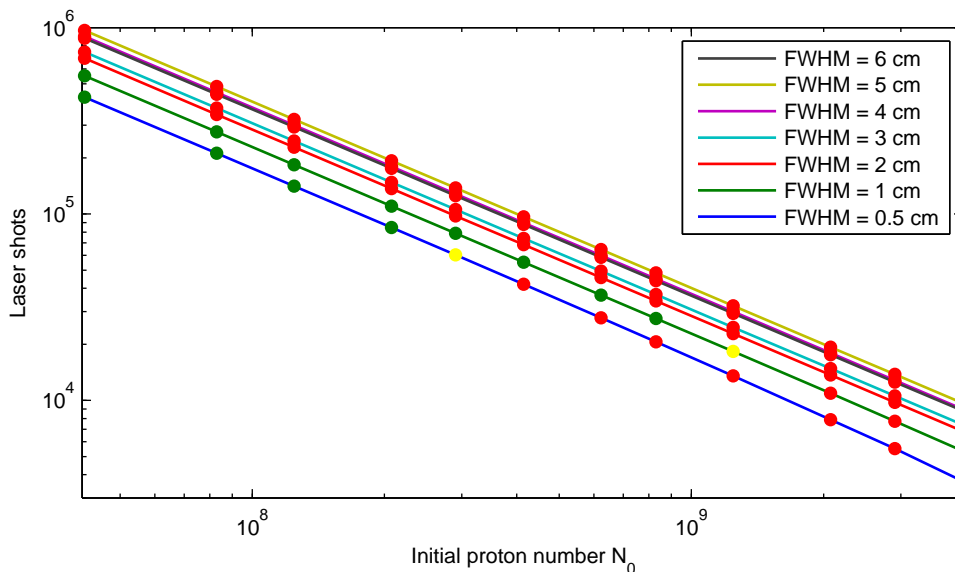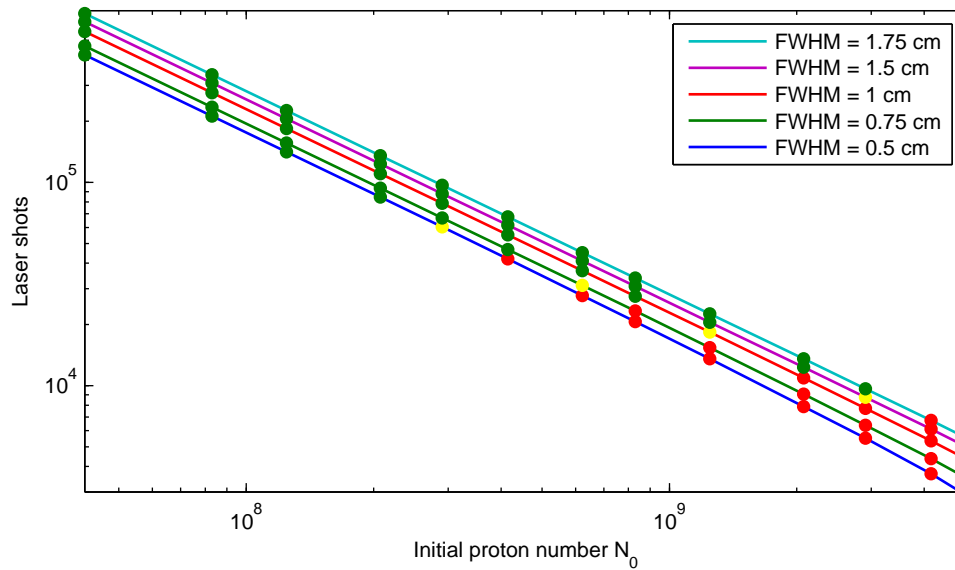
Figure 5.4: Treatment plans calculated for the astrocytoma patient for all studied beam widths. Green circles represent plans of good quality, yellow circles intermediate and red circles non-relevant plans according to table 5.1.

show a transversal and a sagittal slice of the patient CT for the full dose range whereas figure 5.3c) and d) represent an enlarged view of the PTV for the clinically relevant dose ranging from 95% of D_{pres} to the maximum dose. The color distribution illustrates that the target is covered well with at least 95% of the prescribed dose and nearly no normal tissue is irradiated with a dose higher than 1.9 Gy. Thus, this plan belongs to the green category according to table 5.1 and would therefore be represented with a green circle in an overview plot like figure 5.4 or figure 5.5. Both of these plots illustrate other obtained astrocytoma plans and their respective qualities for different analyzed beam widths and initial proton numbers. All circles represent one 3D dose distribution and are presented in the color of their category as the previously discussed green plan at a FWHM of 1.25 cm (not shown in the mentioned figures).

The overview plot in figure 5.4 shows a wide range of beam widths and initial proton numbers and highlights the restrictions for good quality plans. For beam widths equal to or larger than 2 cm only red plans, i.e. non-relevant dose distributions can be obtained. Furthermore, figure 5.4 indicates that the higher the initial proton number N_0 the rarer are the good quality proton plans. If this proton number per bunch is higher than $N_0 \approx 10^9$ no green or yellow plans can be generated at all as too much dose would be delivered with one shot or the beam width is too large to produce target conform dose distributions. Note that the order of the colored lines in figure 5.4 representing different FWHM is not well-sorted. There is not only one reason since many plan parameters influence the total required shot number. A

Figure 5.5: Treatment plans calculated for the astrocytoma patient for interesting beam widths. Green circles represent plans of good quality, yellow circles intermediate and red circles non-relevant plans according to table 5.1.

combination of the spot grid and, hence, the spot number, the different clustering depending on the geometrical spot locations and the resulting diverse optimization may lead to the wrong sorting of some beam width lines.

Due to the few good proton plans generated in this large FWHM range, smaller beam widths have been analyzed with a finer step size leading to figure 5.5. Using these parameters more green plans can be obtained. It is shown that for initial proton numbers smaller than around $2 \cdot 10^8$ good plans are produced independent on the beam width. Since one cluster needs several laser shots ($\gg 1$) to yield a dose of $2\,\text{Gy}$ the errors made by rounding to the next integer weight are not huge and insignificant. However, the number of laser shots to deliver such a plan is high (above 10^5). Going to larger initial proton numbers the green plans become rarer again, as only few or actually partial shots per spot are required ($\omega_j \approx 1$ or $\omega_j < 1$). Hence, the rounding errors are more relevant and change the final dose perceivable compared to the optimized dose. For initial proton numbers above 10^9, green plans can only be obtained when spreading the protons over a wider area within the patient, i.e. for larger FWHM. This fluence reduction per shot however is only useful for FWHM $\approx$ 1-2 cm since only red proton plans are obtained for FWHM $> 2\,\text{cm}$ (see figure 5.4). The most efficient plan for this patient, regarding dosimetric quality and delivery time, is the one with an initial proton number of $2.9 \cdot 10^9$ and a FWHM of $1.75\,\text{cm}$, if no yellow plans are regarded. To deliver this plan, 9653 laser shots are required which corresponds to a delivery time of about $16\,\text{min}$ (for a repetition rate of $10\,\text{Hz}$). The quality parameters of this plan are TC=100%, CN=90%, D_{min}=1.90 Gy (i.e. 95% of D_{pres}) and D_{max}=2.07 Gy (i.e. 103.5% of D_{pres}). When comparing this plan
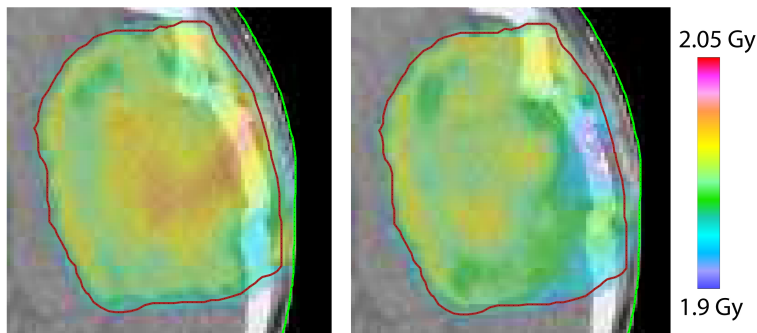
Figure 5.6: Dose comparison between a green and a yellow plan for the astrocytoma patient. On the left the green plan is shown and on the right the yellow plan with the small region on the left edge of the PTV (right side in the CT image) close to the skin receiving less than 1.9 Gy.

to the yellow plan with the same initial proton number it turns out that the PTV of the yellow plan (FWHM=1.5 cm) is not completely covered with 1.9 Gy since the dosimetric parameters are TC=97%, CN=90%, D_{min}=1.85 Gy (i.e. 92.5% of D_{pres}) and D_{max}=2.06 Gy (i.e. 103% of D_{pres}). This lack of dose can also be highlighted when comparing the dose distributions in the clinically relevant range as exemplarily demonstrated with one transversal slice in figure 5.6. On the left, the green plan is shown whereas the right figure represents the dose in the same slice for the yellow plan. In this comparison it is clearly visible that the PTV is not covered completely in the yellow plan (as already indicated with the TC and the D_{min} value). In this case, the medical doctor would have to decide whether a coverage of the PTV with about 92.5% of the prescribed dose is satisfactory as the minimum dose to at least 1 cm^3 is 1.85 Gy. Therefore, this plan reasonably belongs to the yellow and not to the green category. Additionally, the delivery time would not be decreased significantly when choosing the yellow plan with 8772 laser shots corresponding to around 15 min. Considering 30 min ($1.8 \cdot 10^4$ laser shots) as an absolute maximum limit of delivery time, the initial proton number per bunch must stay in the range of $1.4 \cdot 10^9$ - $2.9 \cdot 10^9$ when treating the astrocytoma patient with the given TNSA spectrum and the given beam line independent whether the green or the yellow plan is chosen.

The results for the metastasis patient are shown in figure 5.7 and figure 5.8. Concerning the quality dependence on the initial proton number, these plots are equivalent to the astrocytoma overview plots. However, the overall laser shot numbers are reduced. Furthermore, it is shown that beam widths larger than 1.25 cm are too large to produce relevant dose distributions in such a small PTV. Therefore, only the small beam widths are shown even if larger FWHM (up to 3.0 cm) have also been tested for this anatomy. The most efficient plan for the hypofractionation (figure 5.7) is calculated for $6.2 \cdot 10^9$ initial protons requiring 463 laser shots at a FWHM of 0.75 cm. This corresponds to a delivery time below 1 min when utilizing a 10 Hz system. A good proton plan can also be produced with $8.3 \cdot 10^9$ initial protons with
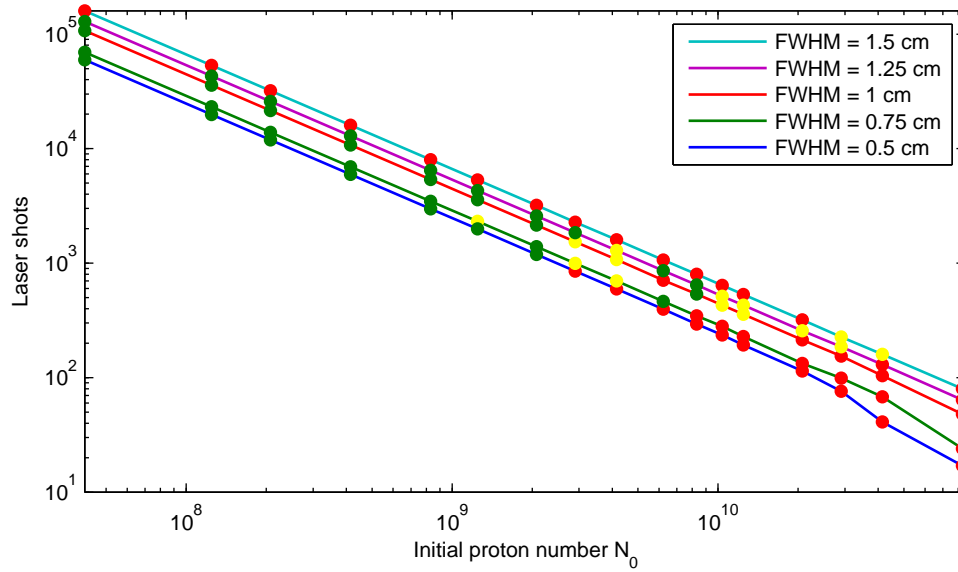
Figure 5.7: Treatment plans calculated for the metastasis patient receiving 5 Gy per fraction. Green circles represent plans of good quality, yellow circles intermediate and red circles non-relevant plans according to table 5.1.
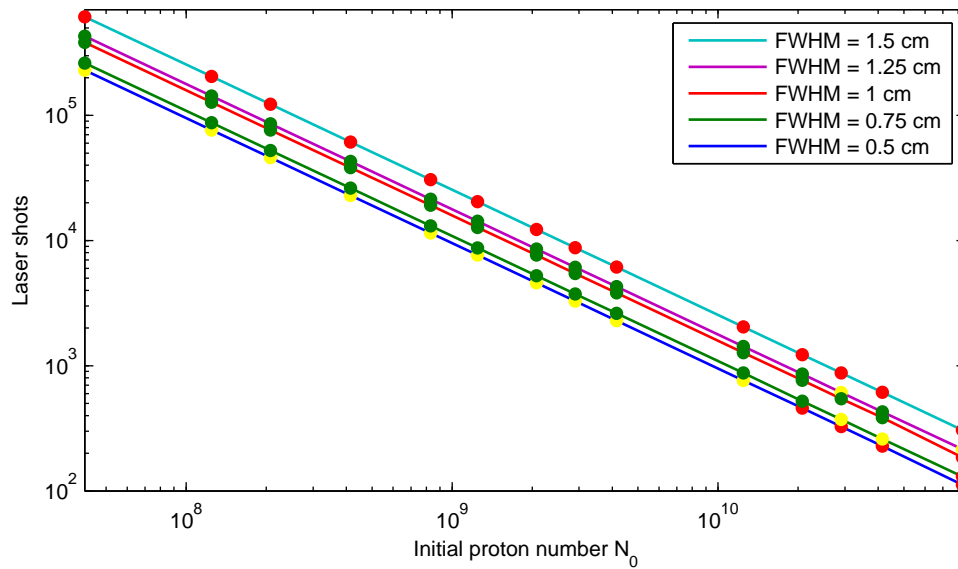

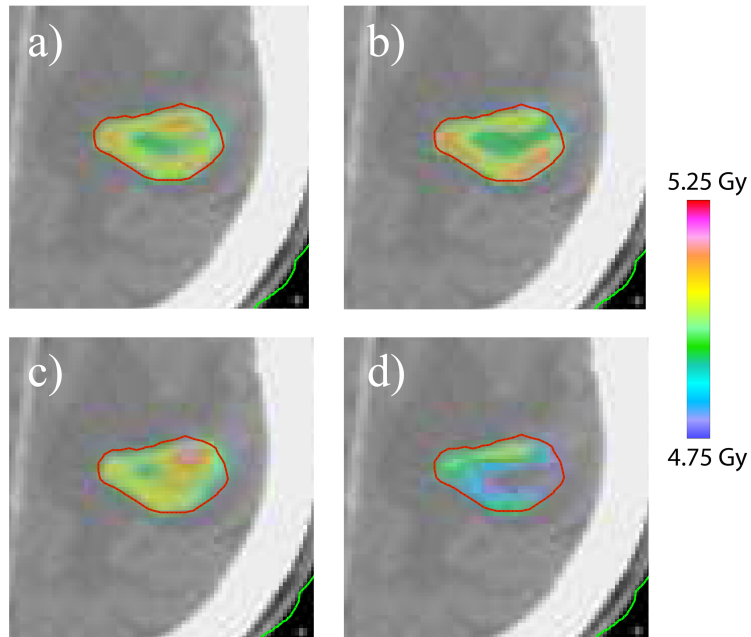Figure 5.8: Treatment plans calculated for the metastasis patient receiving 20 Gy in one fraction. Green circles represent plans of good quality, yellow circles intermediate and red circles non-relevant plans according to table 5.2.

Figure 5.9: Dose comparison between four hypofractionationed plans. a) represents a green plan, b) a yellow plan, c) another green plan and d) a red plan. The relevant dose to the PTV is shown for the same transversal slice in all figures.

537 shots and a FWHM of $1.0\,\mathrm{cm}$ increasing the manageable proton number per bunch slightly. The widest useful range of the initial proton number per bunch is determined to range from $1.4 \cdot 10^8$ to $8.3 \cdot 10^9$ for the green plans. This range is one order of magnitude wider than for the astrocytoma patient mainly due to the smaller target volume but also because a higher dose per bunch is acceptable for $5\,\mathrm{Gy}$ per fraction in total. When $20\,\mathrm{Gy}$ are prescribed within one fraction to the metastasis patient at least 385 laser shots are required as shown in figure 5.8 which also corresponds to a delivery time below $1\,\mathrm{min}$. This number is even smaller than the smallest shot number for the hypofractionation even if the prescribed dose is four times higher than the prescribed dose for the hypofractionation. The reason is that again a higher proton number per bunch can be utilized. Considering the plan quality and the maximum delivery time the initial proton number must stay between $6.0 \cdot 10^8$ and $4.1 \cdot 10^{10}$ for the delivery of $20\,\mathrm{Gy}$ in one fraction.

In figure 5.7 as well as in figure 5.8 it can be observed that yellow plan qualities may be obtained followed by another green plan for a higher initial proton number for the same beam width (e.g. see FWHM=$1.0\,\mathrm{cm}$ curve). This may originate from one dosimetric parameter that violates an evaluation criteria just slightly and, therefore, relegates a certain plan to the yellow category. The following green plan may yield an insignificantly better parameter value for which reason this plan belongs to the

N_0	category	TC [%]	CN [%]	$D_{min}(1\,\text{cm}^3)$ [Gy]	$D_{max}(1\,\text{cm}^3)$ [Gy]
$4.2 \cdot 10^7$	green	98	87	4.95	5.04
$4.2 \cdot 10^9$	yellow	99	85	4.96	5.07
$6.2 \cdot 10^9$	green	98	87	4.94	5.07
$8.3 \cdot 10^9$	red	89	78	4.82	5.04

Table 5.3: Comparison of four metastasis plans based on the evaluation criteria tumor coverage (TC), conformity number (CN) and the minimum (D_{min}) and maximum dose (D_{max}) to at least $1\,\text{cm}^3$. The dose distributions are shown in figure 5.9 and the DVHs in figure 5.10.

green category (e.g. TC_1=97.5% vs. TC_2=97.4% which are rounded to TC_1=98% vs. TC_2=97%). Another reason may be the unprofitable rounding of optimized weights to the next integer which may be more pronounced in one special plan (in this case, the yellow plan "between" the green plans). Both reasons also serve as an explanation why no green plan can be obtained for a FWHM of 0.5 cm which, in general, is not necessarily reasonable. Both facts suggest that the evaluation of a plan by only utilizing certain parameters may not be the best way to report about its clinical quality (which was already stated when introducing the evaluation criteria in section 4.1.4).

Certainly, the fact is even more pronounced for the small PTV of the metastasis patient since one voxel represents a larger relative portion of the target volume than for the astrocytoma PTV and, hence, one voxel dose contributes more strongly to the calculated indices. To analyze this, a comparison between four hypofractionated metastasis proton plans (all planned with FWHM=0.75 cm) is shown in figure 5.9. All subfigures illustrate the same transversal slice of the PTV and the planned dose in the relevant range (95% to 105% of D_{pres}). Figure 5.9a) illustrates a green plan at a low proton number per bunch ($N_0 = 4.2 \cdot 10^7$) which is compared to a yellow plan ($N_0 = 4.2 \cdot 10^9$) in 5.9b), to another green plan with a higher initial proton number ($N_0 = 6.2 \cdot 10^9$) in 5.9c) and to a red plan ($N_0 = 8.3 \cdot 10^9$) in 5.9d). One 2D slice is not representative for the whole plan, however, these 2D views as well as a 3D consideration of the dose using the TPS yielded nearly no difference between the first three doses, at least concerning the coverage and conformity. This means, no clear distinction can be found between a yellow plan and two green plans with different initial proton numbers (see table 5.3). In contrast to this, it can be clearly seen that the PTV is not covered completely with sufficient dose in the red plan shown in figure 5.9d). Considering the PTV DVHs of these four plans (shown in figure 5.10) similar results can be stated. The red DVH corresponding to the red plan does worse than the other DVHs, but no significant difference can be found when comparing the green DVHs to the yellow DVH. In this comparison, the yellow plan is relegated to the yellow category because of its conformation index being CN=85%. The other evaluation criteria stay in the green ranges as listed in table 5.3.
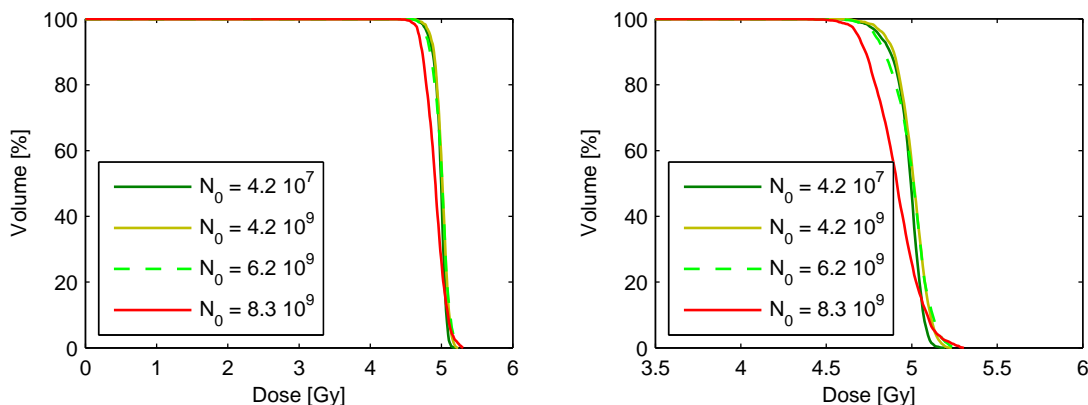
Figure 5.10: DVH comparison of the four plans of figure 5.9. The right DVH shows a zoom of the left DVH. The colors of the respective DVHs correspond to their category.

The detailed consideration of the 3D doses stresses that single yellow plans can have clinically relevant qualities as well and only the red plans are of no interest for this study. For instance, the yellow plan for the hypofractionation at a FWHM of $1.5\,\mathrm{cm}$ at an initial proton number of $N_0 = 4.2 \cdot 10^{10}$ shows a clinically interesting dose distribution as well as the radiosurgery plan at a FWHM of $1.25\,\mathrm{cm}$ and $N_0 = 8.3 \cdot 10^{10}$. Both plans do not exactly meet the evaluation criteria but may increase the possible range for the initial proton number and decrease the laser shots slightly depending on the clinical goals which may vary from patient to patient.

In the context of the integer shot study, the proportion of the different bandwidths $\Delta E/E_{nom}$ contributing to the final plans was evaluated. By storing the beam configurations j and their respective bandwidths (ranging from 4% to 24%) and by adding up all shots delivering a certain bandwidth, the mean frequency of occurrence was found for all plans with beam widths between FWHM=$0.5\,\mathrm{cm}$ and FWHM=$2.0\,\mathrm{cm}$. This mean occurrence is displayed in figure 5.11 for the astrocytoma patient. It is demonstrated that the smallest energy window of 4% contributes with nearly 50% on average to the optimized plans. The broadest bandwidth of 24% contributes more than the others but only with about 15%. However, when weighting the bandwidths of the spectra with the delivered number of protons contained per bunch the contribution of the energy widths is changed significantly as displayed in figure 5.12. The frequency of occurrence is shown for one representative plan with $N_0 = 4.2 \cdot 10^7$ and a FWHM of $1.5\,\mathrm{cm}$ such that the shots contributing to this plan could be weighted with the delivered particle number per bunch. It becomes apparent that the broadest bandwidths of 24% contribute the most (about 46%) to the whole dose distribution whereas all other widths contribute significantly less. This analysis highlights that the pre-selection of curves in the TPS worked well and that the broad, efficient spectra contribute to the plans to a large extend.
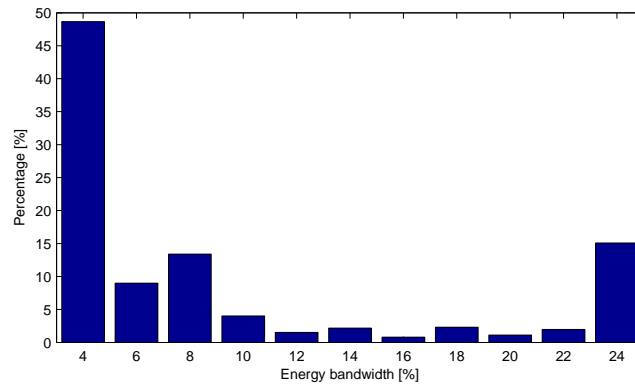
Figure 5.11: Frequency of occurrence of all possible energy bandwidths. The given percentages refer to all astrocytoma patient plans with $0.5\,\mathrm{cm} \leq \mathrm{FWHM} \leq 2.0\,\mathrm{cm}$ on average independent on the nominal energy.
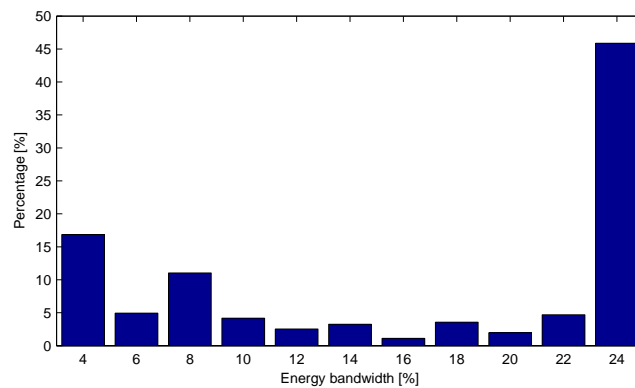
Figure 5.12: Percentage of all possible energy bandwidths contributing to the final dose of one representative plan with $N_0 = 4.2 \cdot 10^7$ and $\mathrm{FWHM}{=}1.5\,\mathrm{cm}$. The delivered spectra have been weighted with the contained proton number to obtain the dosimetric contribution of the bandwidths to the final plan.
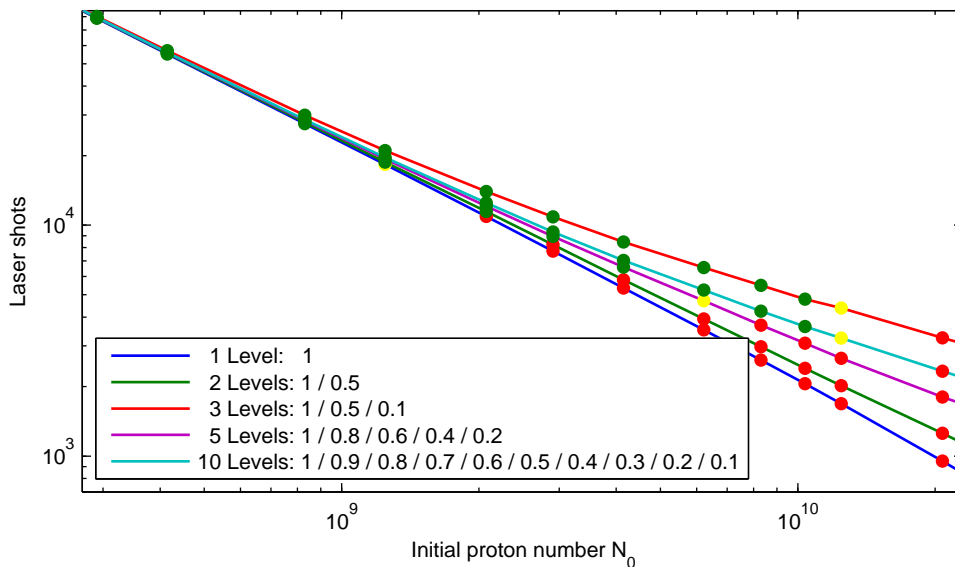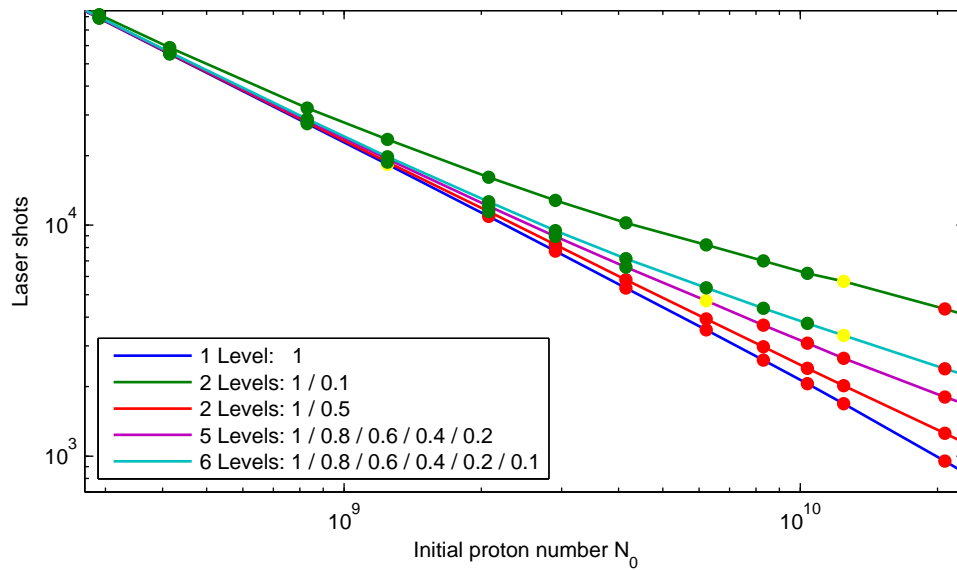
Figure 5.13: Treatment plans and plan qualities (according to table 5.1) for the astrocytoma patient using an intensity modulation from shot to shot for interesting intensity levels. All plans are computed with a fixed beam width of FWHM=1.0 cm. The number of levels and their intensity values are listed in the legend. Green circles represent plans of good quality, yellow circles intermediate and red circles non-relevant plans.

5.4.2 Intensity modulation from shot to shot

By introducing an intensity modulation from shot to shot an increase of plan quality was expected, especially for low-shot plans. This is caused by the fact that the optimized weights can be realized more accurate, i.e. the deviation of the delivered weight to the optimized weight is smaller than in the integer shot scenario. Different combinations of available intensity levels were tested such as ten levels of equally spaced intensities from 100% to 10% in steps of 10% or only a two level scenario with the intensities 100% and 50% for instance. For the astrocytoma patient all investigated scenarios are shown in two plots in figure 5.13 and figure 5.14. For the metastasis patient receiving 5 Gy per fraction only the interesting level combinations are presented in figure 5.15. In all three overview plots, the studied intensity modulations from shot to shot are compared to the integer shot version which is equivalent to only one level of 100%.

For all potential level combinations and each patient, nearly no difference can be observed concerning the obtained plan quality or the required shot numbers when low initial proton numbers are contained in one bunch. The weights per cluster are higher in these cases and, hence, the integer part of these weights determines the shot number primarily. For example, a weight of 100.74 would be delivered with

Figure 5.14: Treatment plans and plan qualities (according to table 5.1) for the astrocytoma patient using an intensity modulation from shot to shot comparing similar intensity level combinations. All plans are computed with a fixed beam width of FWHM=1.0 cm. The number of levels and their intensity values are listed in the legend. Green circles represent plans of good quality, yellow circles intermediate and red circles non-relevant plans.

around 100 laser shots (101 for one level of 100% and 103 for three levels of 100%, 50% and 10%) but would not show a remarkable dosimetric error compared to the optimized weight of 100.74 since for the one level case 101.0 and for the three level case 100.7 would be delivered. Therefore, the plan qualities are similar and the green circles lie close to each other in all overview plots. On the contrary, for higher initial proton numbers one can observe a more pronounced increase of required laser shots compared to the integer scenario (shown in blue in all three plots). This is caused by the small weights per cluster in these plans. Since not only the integer part but also the decimal part is delivered via laser shots, the total shot number is mainly determined by these decimal points. In the integer scenario a weight of 1.75 would for example be delivered with two shots, but in the three level scenario used above, with five shots, where four of them are required to deliver the decimal digit (one shot of level 100%, one shot of level 50% and three shots of level 10%, leading to a delivered weight of 1.8). However, since the optimized weights can be delivered more precisely using a shot-to-shot intensity modulation (delivered weight of 1.8 versus 2.0 (integer shots) for an optimized weight of 1.75), the plan qualities can be improved as well. This is more pronounced for the astrocytoma patient as shown in figure 5.13 and figure 5.14. In the case of the metastasis patient the produced doses are improved as well but the categories of the plans are mainly improved from red

to yellow but not to green.

Analyzing figure 5.13 in more detail, the red and cyan level combination with five and ten possible levels show the largest increase in shot numbers but also yield plans of good qualities for higher initial proton numbers compared to the integer scenario (blue). The last green plan for the ten intensity level scenario requires $3.6 \cdot 10^3$ shots which is about twice the shot number for the same N_0 and the one level case ($2.1 \cdot 10^3$ shots). However, this green plan for the ten levels requires less shots compared to the last green plan without intensity modulation (1 level: $2.8 \cdot 10^4$ shots). This shows that the quality improvement effect is more pronounced than the increase of shots for which reason an overall decrease of laser shots can be achieved by an intensity modulation from shot to shot. In figure 5.13 the red case with five intensity levels yields a similar result which suggests that the 10% intensity level is important for the plan quality. The other two scenarios in this figure illustrate only a slight increase in quality and, therefore, only a slight decrease in the shot number. Therefore, other combinations have been studied depicted in figure 5.14. Again, four intensity modulations are compared to the integer shot case. In this figure two different combinations of the two level case are compared, one with the intensities 100% and 50% and the other with 100% and 10%. Furthermore, the previously presented five level combination ranging down to 20% was compared to the same combination with an additional 10% level, i.e. six levels in total. Figure 5.14 demonstrates that indeed the 10% intensity level improves the quality since the two level scenario with the 10% level as well as the six level combination yield the best plans for high initial proton numbers. Comparing the five and the six level case (magenta and cyan) no big difference can be observed concerning the shot numbers since these combinations are relatively similar. However, when comparing both two level cases (green and red) the difference is more pronounced. The plan qualities when only using 100% and 50% levels are not significantly better than the integer shot scenario and, therefore, also the shots numbers are similar for each N_0. In contrast to this, the two level plans with the 10% intensity option require much more shots for a given N_0. The reason for this has already been introduced in section 5.3.2 with the example of $\omega_j = 0.9$ which is delivered with nine shots for the intensity modulation with a 10% intensity level compared to just one shot in the integer scenario.

The trend for the metastasis patient is similar to the astrocytoma patient, however, as mentioned before, the quality increase is not that pronounced as shown in figure 5.15. In this plot, the last green plan for the integer scenario can be found at $N_0 = 1.8 \cdot 10^9$ requiring 537 laser shots. The only plans yielding a green quality with a reduced shot number can be produced with the five and the ten level combination at $N_0 = 2.7 \cdot 10^9$ requiring 379 laser shots. However, as discussed in the section before, especially in the case of the metastasis patient the yellow category does not only include unacceptable plans qualities. With a detailed analysis the yellow plans in figure 5.15 with an initial proton number larger than $3 \cdot 10^9$ may potentially have acceptable 3D dose distributions as well and, therefore, may decrease the required
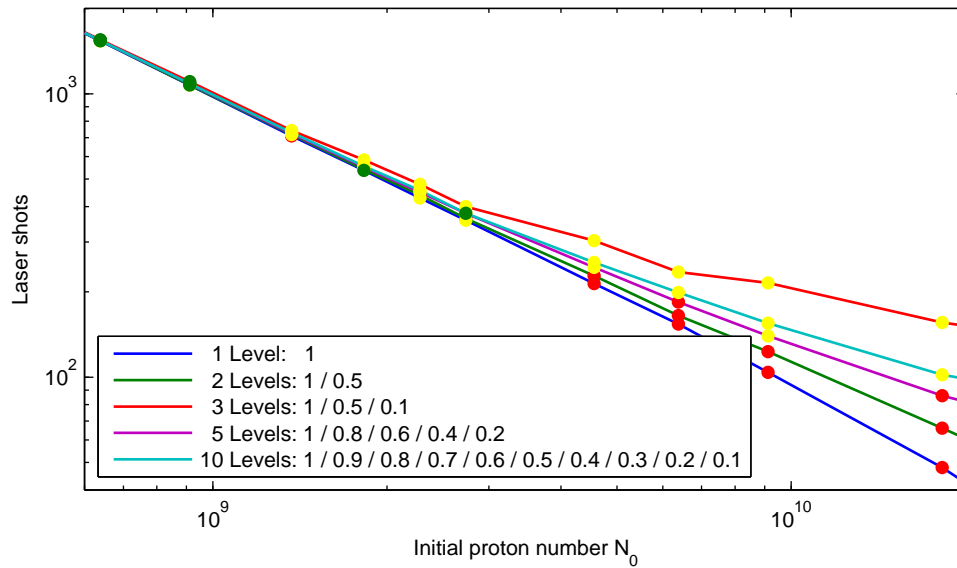
Figure 5.15: Treatment plans and plan qualities (according to table 5.1) for the metastasis patient using an intensity modulation from shot to shot for interesting intensity levels. All plans are computed with a fixed beam width of FWHM=1.0 cm. The number of levels and their intensity values are listed in the legend. Green circles represent plans of good quality, yellow circles intermediate and red circles non-relevant plans.

laser shot numbers for clinically interesting plans further. However, due to the low shot number for the hypofractionation even without an intensity modulation, the shot reduction for yellow plans is not analyzed in detail at this point.

In general, for both patients the most efficient intensity modulation turns out to be the one with ten equidistant levels. For the astrocytoma patient good plans qualities can be found requiring only 3641 shots (about 6 min delivery time) compared to the integer shot case with the least laser shot number of 9653. For the metastasis patient the shot number could be decreased from 463 to 379. This corresponds to a shot reduction to about 38% in the case of a large PTV and to about 82% for the small PTV. However, in the case of the small PTV, the delivery time was already low for the integer bunches and, hence, the astrocytoma patient offered a greater potential for improvement anyway. Again, the main reason why the shot number can be reduced extremely in this case is the presence of the 10% intensity level together with the most available number of levels. By rounding the weights either up or down to a multiple of 0.1, the error compared to the optimized weight is 0.05 at the most. Therefore, the dose distributions of low-shot plans are still of quite good quality.
The quality degradation created by rounding the optimized weights to deliverable weights is displayed in figure 5.16. For four initial proton numbers the target DVHs

76

for the astrocytoma patient are illustrated for the integer shot scenario (black) and two intensity modulations (IM), namely the case with ten (green) and five (magenta) equidistant levels. All these DVHs are generated with the post-processed weights of the respective modulation scheme and are compared to the original DVH (blue). This original DVH bases on the dose distribution obtained by multiplying the optimized weights directly with the D_{ij} matrix as if the beam line could deliver any desired amount of protons of a given beam configuration. In the case of a lower initial proton number ($N_0 = 8.3 \cdot 10^8$) both intensity modulated DVHs lie above the original DVH meaning that with both intensity level combinations the original weights can be assembled very well. By rounding the weights to the next integer the quality of the optimized dose is decreased since the black DVH is less steep than the others. However, for this initial proton number, even the integer shots lead to a green plan quality according to the evaluation criteria. Going to higher initial proton numbers the integer delivery leads to relegated plans (yellow for $N_0 = 1.3 \cdot 10^9$ and red for $N_0 = 2.1 \cdot 10^9$ and $N_0 = 1.0 \cdot 10^{10}$) as shown in the DVHs in figure 5.16. Both intensity modulations can represent the original dose still well and belong to the green category, however, the modulation using five levels is slightly worse than the ten level scenario. For an initial proton number of $N_0 = 2.1 \cdot 10^9$ it becomes obvious why the integer shot plan is unacceptable (red) but the intensity modulation plans are still of a good quality (green) and comparable to the originally optimized plan. When increasing N_0 by another order of magnitude, the five level scenario relegates to the red category and only the ten level modulation yields an acceptable dose distribution which, however, is worse compared to a delivery where any desired weights could be provided by the beam line. This comparison explains well the quality degradation due to the post-processing of weights, but also shows that nevertheless the "best" post-processing with ten intensity levels is not as good as the results obtained by the optimizer.

Additional to the plan quality, the optimized and post-processed weights were analyzed in detail for the last green plan of the ten level intensity modulation, i.e. for a FWHM=1 cm and an initial proton number of $N_0 = 10^{10}$ (compare to the lower right plot in figure 5.16). For the given plan parameters 4642 beam configurations j have been committed to the optimizer in total but 1667 were optimized to not contributed to the final dose distribution ($\omega_j = 0$). The other 2975 configurations were assigned with weights between $\omega_j = 10^{-4}$ and $\omega_j = 17.0$. The mean value of all optimized weights is $\overline{\omega_j} = 0.74$ which explains why a rounding to the next integer value leads to an unacceptable red plan quality (shown in black in figure 5.16 for $N_0 = 10^{10}$). The absolute deviations of the post-processed weights to the optimized weights have been calculated for each beam configuration j contributing to the plan for the integer bunches and the ten level intensity modulation. Certainly, for the integer shot case the maximal error is $\Delta\omega_{j,max} = 0.5$ whereas the maximal error for the intensity modulation is $\Delta\omega_{j,max} = 0.05$, as mentioned before. The mean value of all plan relevant absolute errors was found to be $\overline{\Delta\omega_{j,integer}} = 0.08$ for the integer shot delivery but only $\overline{\Delta\omega_{j,IM}} = 0.01$ for the intensity modulation. The approxi-
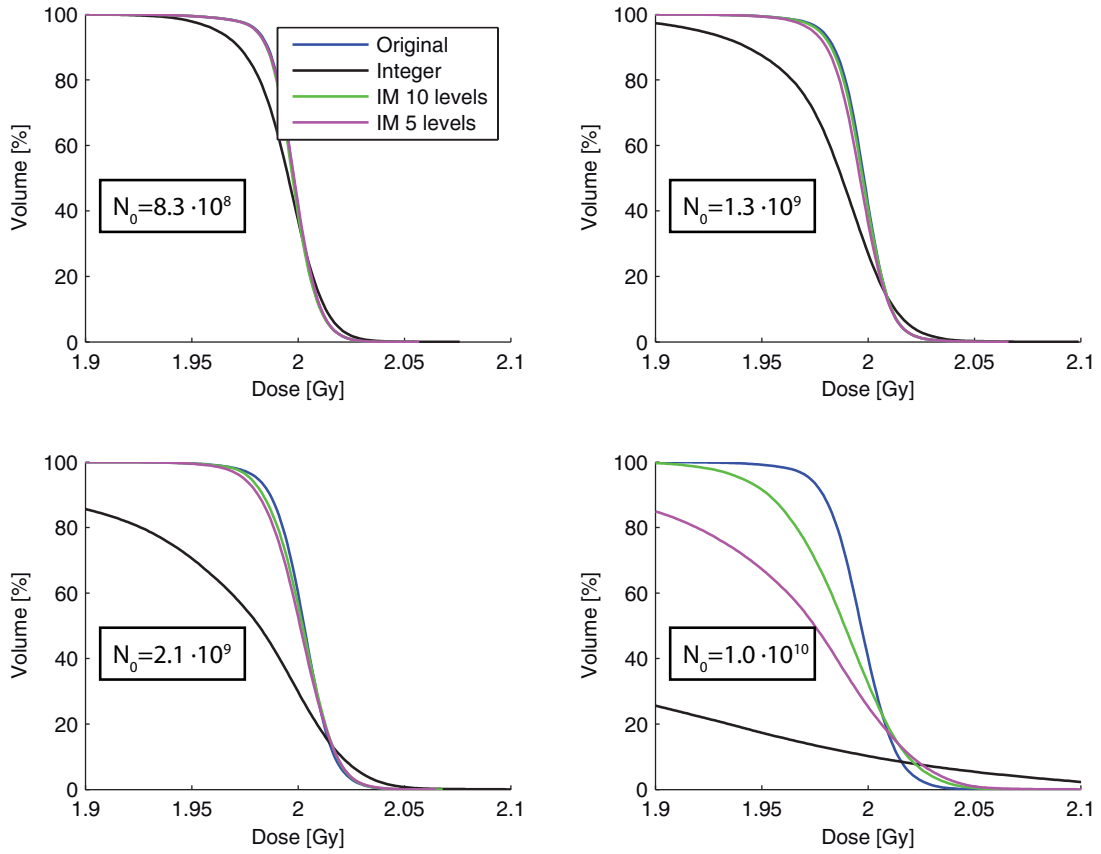
Figure 5.16: DVH comparison for the astrocytoma patient for four different post-processings and four initial proton numbers N_0. The integer shot scenario (black) is compared to two intensity modulations (IM) from shot to shot with either 10 equidistant (green) or 5 equidistant (magenta) levels. The blue DVHs named "Original" refer to the original dose without a post-processing step, i.e. to the dose distribution that would be obtained when the optimized floating point weights would be delivered exactly. All plans rely on a FWHM of 1 cm and the corresponding plan categories are mentioned in the text.
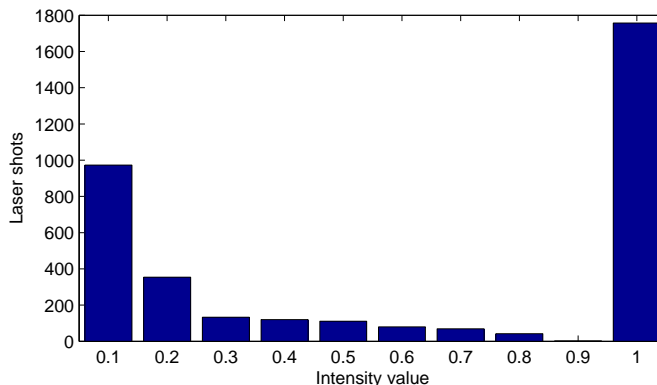
Figure 5.17: Evaluation of the contribution of each intensity level to the generated astrocytoma treatment plan. To deliver this plan (FWHM of 1 cm and $N_0 = 10^{10}$) 3641 laser shots are required whereof 1757 are full shots and 973 are shots of 10% of the original intensity.

mately ten times decreased mean error of the deliverable weights compared to the optimized weights illuminates the distinct degrees of deviations of the DVHs from the originally optimized DVH.

Moreover, the contribution of each of the ten intensity levels to the final dose distribution was evaluated and is depicted in figure 5.17. To deliver this plan 3641 laser shots are required in total. The largest portion of this shot number is delivered with full shots (1757 shots) and the second largest portion with the 10% intensity level (973 shots). All other levels contribute less to the overall shot number. This demonstrates again the importance of the 10% intensity level since around 27% of the delivered laser shots are down-regulated to deliver only 10% of the initial fluence. Compared to this around 48% of all required shots are 100% intensity shots and only one quarter of the delivered shots contains another intensity value.

5.4.3 Shot-to-shot fluctuations

To analyze the impact of shot-to-shot fluctuations one hundred plans were calculated for each studied N_0 and each severity of fluctuations and were compared to the reference plan. This reference plan refers in each case to the integer shot plan with no fluctuations, i.e. when assuming the dose would be delivered exactly as planned. For the comparison at a first glance, DVHs of the PTV were utilized. Figure 5.18 illustrates all obtained DVHs for the astrocytoma patient calculated with a FWHM of 1.75 cm. The four subfigures show a low and a high initial proton number, i.e. $N_0 = 8 \cdot 10^7$ and $N_0 = 3 \cdot 10^9$, and fluctuations in the range of $\pm 10\%$ and $\pm 30\%$. In red, the DVH of the reference plan is highlighted and in blue all hundred plans underlying shot-to-shot fluctuations are shown. It directly appears, that the two reference plan qualities differ depending on N_0, however, both plans belong to the green category. Table 5.4 additionally contains an intermediate proton number per
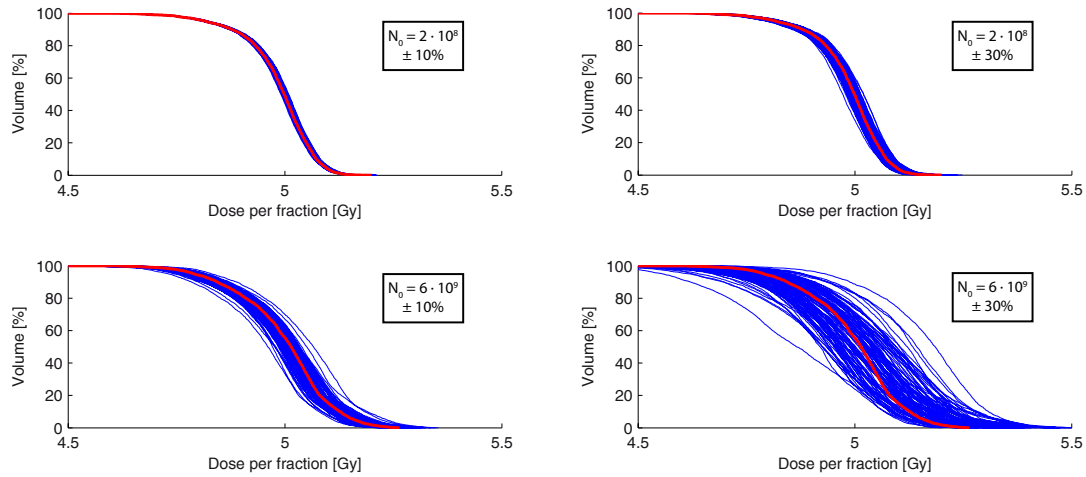
79
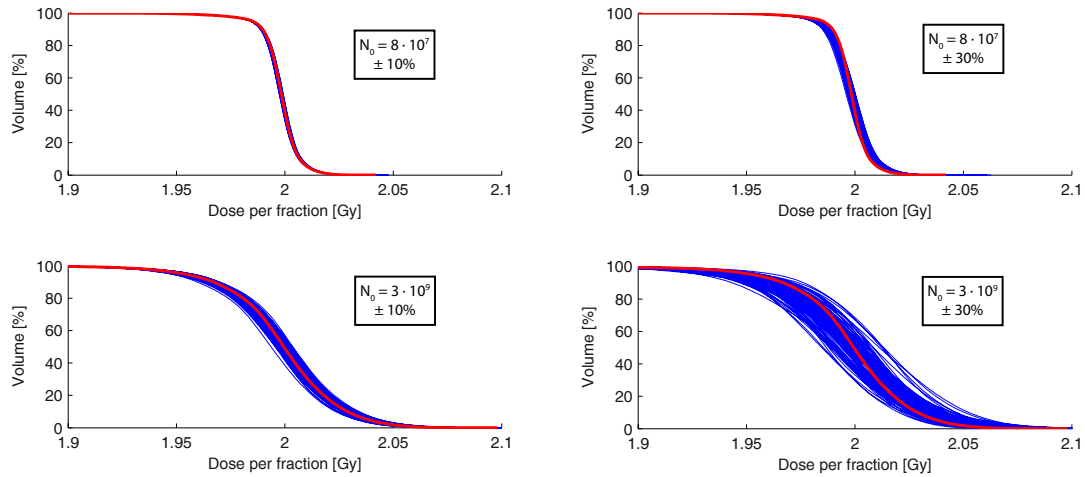
Figure 5.18: Dose volume histograms of the PTV of the astrocytoma patient for
shot-to-shot fluctuations. A reference plan (red) is compared with 100
plans underlying random fluctuations (blue) of different severities for
different initial proton numbers N_0. All plans have been calculated
for a FWHM of 1.75 cm. The reference plan relies on the integer shot
delivery.

bunch and the extreme case of fluctuations in the range of $\pm 100\%$. In this table the
evaluation criteria of the reference plan are compared to the minimum, mean and
maximum obtained criteria of the respective hundred plans with fluctuations.

Figure 5.18 demonstrates that for the lower initial proton number, i.e. the plans
requiring more laser shots, an averaging effect of shots with too high and too low dose
takes place due to the randomness of the fluctuations. Thus, a fluctuation of $\pm 30\%$
does not result in an over- or underdosage of $\pm 30\%$ in the single plans. The DVHs are
clinically acceptable for all plans with $8 \cdot 10^7$ initial protons and $\pm 10\%$ since nearly no
difference can be observed between the red and the blue DVHs. When additionally
analyzing the minimum, mean and maximum values for the evaluation criteria for
this N_0 (table 5.4) it turns out that even the $\pm 30\%$ and the $\pm 100\%$ fluctuations
lead to hundred acceptable, green plans for such a low proton number. In the case
of a higher N_0 the deviations in the DVHs are more pronounced, especially for the
$\pm 30\%$ fluctuation range. Since for these plans only one or few shots are required to
deliver the dose to one cluster, the fluctuations cannot cancel out so well anymore.
Dependent on the location of the cluster and whether it receives too few or too many
protons, the DVHs can look quite similar or completely different compared to the
reference DVH. In this case, not even all generated plans with fluctuations of $\pm 10\%$
would be acceptable with respect to the dosimetric quality of the actually delivered
plan, since the smallest minimum dose to $1\,\mathrm{cm}^3$ is only $1.89\,\mathrm{Gy}$ as shown in table
5.4. This too low D_{min} relegates the certain plan(s) to the yellow category. Table 5.4
additionally includes an intermediate N_0 for which fluctuations of $\pm 10\%$ and $\pm 30\%$

Table 5.4: Dosimetric parameters obtained for shot-to-shot fluctuations of certain severities for the astrocytoma patient. In red the reference plan quality is given for the different initial proton numbers N_0 and the obtained minimum (min), mean and maximum (max) values for the certain evaluation criteria are listed depending on the fluctuation range.

Parameter		TC [%]	CN [%]	$D_{min}(1\,cm^3)$[Gy]	$D_{max}(1\,cm^3)$[Gy]
$N_0 = 8 \cdot 10^7$	Reference	100	89	1.92	2.05
±100%	min mean max	100 100 100	89 89 90	1.91 1.92 1.93	2.04 2.05 2.08
±30%	min mean max	100 100 100	89 90 90	1.92 1.92 1.92	2.04 2.05 2.05
±10%	min mean max	100 100 100	89 89 90	1.92 1.92 1.92	2.04 2.05 2.05
$N_0 = 8 \cdot 10^8$	Reference	100	98	1.92	2.05
±100%	min mean max	98 99 100	88 89 91	1.84 1.89 1.92	2.05 2.10 2.15
±30%	min mean max	100 100 100	89 90 90	1.90 1.92 1.93	2.04 2.05 2.07
±10%	min mean max	100 100 100	89 90 90	1.92 1.92 1.92	2.04 2.05 2.05
$N_0 = 3 \cdot 10^9$	Reference	100	90	1.90	2.07
±100%	min mean max	86 94 100	78 85 90	1.70 1.81 1.90	2.07 2.17 2.29
±30%	min mean max	99 99 100	89 90 91	1.87 1.89 1.90	2.06 2.08 2.11
±10%	min mean max	99 100 100	90 90 90	1.89 1.90 1.90	2.06 2.07 2.08

Figure 5.19: Dose volume histograms of the PTV of the metastasis patient for shot-to-shot fluctuations. A reference plan (red) is compared with 100 plans underlying random fluctuations (blue) of different severities for different initial proton numbers N_0. All plans have been calculated for a FWHM of $0.75\,cm$ and a prescribed dose per fraction of $5\,Gy$. The reference plan relies on the integer shot delivery.

lead to hundred acceptable plans. In this case, the shot numbers are high enough to cancel out for the mentioned severities, however not for the highest severity of $\pm 100\%$ where the average minimum dose to the target is too low. This means not only single plans but a larger portion of the hundred plans show a too low dose in the PTV. For the highest N_0 many plans relegate to the yellow category (for $\pm 10\%$ and $\pm 30\%$) or even to the red category (for $\pm 100\%$). Thus, for this patient it can be concluded that for low and intermediate proton numbers per bunch fluctuations of $\pm 10\%$ and $\pm 30\%$ would still yield acceptable plans. However, by keeping the shot numbers as low as possible, i.e. for high initial proton numbers, even a fluctuation of $\pm 10\%$ would not yield acceptable dose distributions anymore.

For the metastasis irradiation with $5\,Gy$ per fraction similar results can be seen in figure 5.19 however with a greater impact on the clinical relevance. For the low initial proton number and the smallest fluctuation range the blue DVHs are similar to the reference DVH and the evaluation criteria of all hundred plans underlying shot-to-shot fluctuations stay in the green category (see table 5.5). However, for the same N_0 but a shot-to-shot fluctuation of $\pm 30\%$ some single plans are relegated to the yellow category due to their TC or CN index (TC_{min}=97% and CN_{min}=86%, see table 5.5). These few plans cannot be distinguished in the DVH plot in figure 5.19 but demonstrate that for the small PTV where in general less laser shots are delivered than in the astrocytoma case already for around 10^8 initial protons the intermediate fluctuation severity may impair the overall plan quality. For higher

proton numbers and even lower shot numbers more and more plans are influenced and relegated to a worse plan category. With an intermediate proton number per bunch not only the $\pm 100\%$ fluctuations lead to unacceptable plan qualities on average but also the $\pm 30\%$ fluctuations. And even the $\pm 10\%$ range relegates at least single plans to the yellow category since the mean values still belong to the green category but some plans yield a conformation number of only 85%. Certainly, this plan degradation is even more pronounced for the highest initial proton number where on average all plans underlying shot-to-shot fluctuations are downgraded to the red category and, therefore, yield DVHs mostly not comparable to the reference DVH as shown in figure 5.19. Thus, when treating a smaller PTV with some hundred up to around one thousand shots the plan quality is influenced strongly by shot-to-shot fluctuations of the proton number even when these fluctuations can be kept in a small range of $\pm 10\%$. To achieve a sufficient averaging effect as for the large PTV it seems that at least some thousand shots are required in total.

This means, when comparing both patients and the obtained results, certainly the impact of the fluctuations on the dose is more relevant for the metastasis patient with the much smaller target volume. This is caused by the slightly worsened reference plan quality compared to the astrocytoma patient, but even more, the significant lower amount of required laser shots for all plans. As demonstrated in the sections before, the small PTV of the metastasis patient needs only 10^3 - 10^4 shots in total to receive the prescribed dose whereas the astrocytoma target requires at least 10^4 - 10^5 shots. Therefore, it is reasonable why the metastasis dose distributions are influenced to a stronger extend than the astrocytoma plans.

5.5 Discussion

The studies demonstrate that it is feasible to produce clinically relevant plans with laser-driven proton beams. However, some limitations were ascertained which depend on the applied assumptions like the utilized initial spectrum or the beam line. These limitations mainly concern the proton number contained in one bunch as well as the required delivery time for a good proton plan. However, the established values should not be taken too strictly and more as an orientation concerning the order of magnitude. This is not only because of the assumptions all these values rely on but also due to the coarse sampling of the data points in the multi-parameter overview plots. For the integer shot study a finer sampling of the initial proton number N_0 was tested and did not yield significantly increased manageable initial proton numbers nor significantly decreased shot numbers, however, it does not demonstrate that good quality proton plans cannot be achieved at all in the ranges were the planning study yielded only unacceptable plans. Additionally, all ranges and shot numbers rely on the evaluation of defined clinically relevant parameters. However, during the study it was found that these parameters do not obligatory represent the quality of the whole 3D dose distribution and particularly not only the generated

Table 5.5: Dosimetric parameters obtained for shot-to-shot fluctuations of certain severities for the metastasis patient (5 Gy/fraction). In red the reference plan quality is given for the different initial proton numbers N_0 and the obtained minimum (min), mean and maximum (max) values for the certain evaluation criteria are listed depending on the fluctuation range.

Parameter		TC [%]	CN [%]	$D_{min}(1\,cm^3)$[Gy]	$D_{max}(1\,cm^3)$[Gy]
$N_0 = 2 \cdot 10^8$	Reference	98	87	4.95	5.04
±100%	*min mean max*	92 97 99	81 86 90	4.85 4.94 5.04	4.97 5.04 5.15
±30%	*min mean max*	97 98 99	86 87 88	4.92 4.95 4.97	5.01 5.04 5.06
±10%	*min mean max*	98 98 99	87 87 88	4.94 4.95 4.96	5.03 5.04 5.05
$N_0 = 2 \cdot 10^9$	Reference	98	87	4.96	5.05
±100%	*min mean max*	56 89 100	52 75 87	4.67 4.89 5.15	4.90 5.11 5.35
±30%	*min mean max*	94 98 99	81 86 89	4.87 4.95 5.04	4.97 5.06 5.15
±10%	*min mean max*	98 98 99	85 87 88	4.93 4.96 4.99	5.03 5.05 5.08
$N_0 = 6 \cdot 10^9$	Reference	98	87	4.94	5.07
±100%	*min mean max*	28 76 100	22 59 87	4.37 4.80 5.47	4.77 5.19 5.89
±30%	*min mean max*	79 95 100	73 83 87	4.78 4.92 5.07	4.95 5.09 5.21
±10%	*min mean max*	94 97 99	85 87 88	4.89 4.94 4.98	5.01 5.07 5.12

green plans but also some yellow plans may yield clinically relevant doses. Thus, the established ranges might be broadened and the required shot numbers might be lowered with a detailed plan review of single yellow plans which also emphasizes that the resulting ranges or shot numbers should only be taken as an orientation. Nevertheless, it should be mentioned that the presented parameter based evaluation allowed for an analysis of multiple proton plans at once. Hence, for investigating the general feasibility of laser-driven proton therapy this fast and basic evaluation covering a wide range of plan and bunch parameters was optimal and sufficient. In this context it should be mentioned that the plan qualities only rely on the dose distribution concerning the target volume. For none of the plans the organ doses have been evaluated even if some organs have been taken into account during the optimization (cf. chapter 5.2). Certainly, the decision whether the plans are of clinical relevance should include the OAR, however, all doses to organs close to the target were found to be acceptable and below the tolerance doses. Furthermore, the whole study focuses on the general feasibility of laser-driven proton therapy which in the first step necessitates a high quality dose distribution concerning the target volume rather than a good sparing of normal tissue. For future studies the doses to the organs should be involved as well as dosimetric comparisons to conventional proton plans for example (cf. chapter 6).

Before discussing the elaborated restrictions, it shall be pointed out that all generated doses rely on broad energy spectra up to a bandwidth of $\Delta E/E_{nom} = 24\%$. It has been analyzed how much these broad spectra contribute to the final dose distribution of a high quality, clinically acceptable proton plan. Considering all green plans with a FWHM from $0.5\,\mathrm{cm}$ up to $2.0\,\mathrm{cm}$ on average about 49% of all shots for one plan are delivered with the smallest bandwidth (4%) and approximately 15% of all shots with the broadest widths of 24%. Weighting the spectra with their contained proton number, i.e. contribution to the final dose it turns out that around 17% of the dose is delivered with 4%-bandwidths and about 46% of the dose with bandwidths of 24% (all other bandwidths contribute less, around 1%-10%). This means half of the dose is delivered with the broadest possible energy widths which certainly originates from the pre-selection of these broad spectra within the TPS. Certainly, this may be different when all potential deliverable spectra would be committed to the optimizer, however, this would increase the number of decision variables a lot and, therefore, would be computationally expensive. Furthermore, when committing all potential spectra to the optimizer the cost function would have to be adapted to favor broad spectra over narrow spectra. Hence, the implemented pre-selection is a clever solution avoiding this cost function change and yielding good dose distributions originating from broad energy bunch spectra.

To use laser-driven protons for radiotherapy one important investigated restriction which was established is the initial proton number per bunch yielding clinically relevant dose distributions. The number is critical since it determines the dose delivered to a certain area within the target with one laser shot. For the analyzed prescribed

doses and PTV sizes it must stay at least in the range of $1 \cdot 10^8$ - $4 \cdot 10^{10}$ when assuming that the intensity cannot be reduced within the beam line and that beam widths in the order of 1-2 cm shall be delivered. The investigated prescribed doses ranged from standard doses per fraction of 2 Gy up to 20 Gy for a stereotactic radiosurgery. Additionally, a standard PTV size as well as a small metastasis volume was studied to cover a wide range of clinical scenarios. However, it shall be mentioned that in a typical proton therapy fractions around 2 Gy will be delivered to a target volume comparable to the astrocytoma PTV for the majority of patients. In this case the initial proton number is even more restricted to be in the order of $2 \cdot 10^9$ without a large range. This confinement applies essentially to the bunch production with the laser and may serve as a feedback for future laser-acceleration research. As mentioned before, this range strongly depends on the initial spectrum assumption and the filtering process of the beam line. Therefore, the established ranges have to be adapted when the laser-produced spectrum changes or the beam line will be of a different design. Note, that the utilized beam widths for the discussed ranges are larger than the beam widths in conventional proton therapy using synchrotrons since the high fluence needs to be spread over a larger area within the target. If these beam widths are undesired for therapy (i.e. when small PTVs should be irradiated) or if the beam line cannot handle such broad beams the stated initial proton numbers per bunch adapt accordingly as well.

Another established limitation directly connected to the proton number is the required number of laser shots since it determines the delivery time of the proton plan. For a typical tumor volume at least 10^4 shots are necessary to deliver 2 Gy to the PTV. Although the shot number can be reduced a lot for smaller targets, the overall mean shot number of different indications and sizes of the PTV will probably be in this order. Assuming a repetition rate of 10 Hz, 10^4 shots correspond to a beam-on time of 17 min, without the consideration of patient set-up or in-room imaging. Therefore, the calculated shot numbers leading to good proton plans are barely at the limit of clinical relevance, especially when comparing these times to conventional (proton or photon) treatment times of 1-3 min. This result stresses the importance of high repetition rates of the laser system as well as the need to reduce the required shot numbers for standard plans. Otherwise, even with 10 Hz systems laser-driven proton therapy would be restricted to few indications with small targets at rigid locations (to avoid drifts of the target over the long treatment time).

Both discussed limitations can be weakened when utilizing an intensity modulation from shot to shot within the beam line, especially for typical targets and doses per fraction. Given such a modulation device, the dosimetric quality can be improved for plans with higher proton numbers per shot and the required laser shot numbers can be decreased from for instance 10^4 to around 3600 (for the standard fractionation). With an appropriate delivery time of six minutes such a plan would be clinically acceptable but still not comparable to delivery times of conventional proton plans. For the smaller target and higher doses per fraction the already shorter

delivery times without an intensity modulation could be reduced as well however to a lesser extend. It was shown that this shot reduction bases on the increased plan quality for higher N_0 as the optimized weights can be delivered more accurate with an intensity modulation from shot to shot. Especially when a down-regulation to only 10% of the original bunch intensity can be utilized, the deliverable plan with its rounded weights still yields acceptable dose distributions. Having more diverse intensity values allows a better reduction of shot numbers and the obtained dose matches the optimized one. Therefore, the most efficient combination found was the one with ten equally spaced levels ranging from 100% down to 10%. However, it was found that for higher initial proton numbers, i.e. lower shot numbers, even the intensity modulation allowing for a delivery of 10% of the original bunch yielded worse dose distributions compared to the optimized one. Therefore, one idea to even lower the deviation to the optimized dose and also lower the delivery time would be the implementation of an intensity modulation on a logarithmic scale. For example with levels of 100%, 10%, 1%, 0.1% and so. The deliverable doses could be even closer to the optimized doses and, hence, the quality would be improved for plans with yet lower shots which would consequentially decrease the overall required shot number. However, such a device might be complicated to build and integrate into the beam line. Another solution of how to decrease the delivery time and get rid of the post-processing procedure would be an integer-optimization. When the TPS would directly come up with an optimal solution of only integer weights, the rounding would not lead to a quality degradation compared to the optimized plan. Then, low-shot plans could have slightly better dose distributions and might need less laser shots. Such an integer optimization (or at least the rounding to the next integer weight) would furthermore not additionally increase the amount of dumped protons like the shot-to-shot intensity modulation does. In section 5.4.2 an exemplary plan was analyzed where around one third of the total delivered shots would have to be down-regulated to deliver only 10% of the original intensity and another quarter to another portion below 100%. This implies an additional extra amount of generated secondary particles beside the amount which is produced anyway due to the broad initial incoming spectrum. Therefore, depending on the final initial energy spectrum and the available repetition rate of the whole system the optimal trade-off between a shot reduction and the additional blocking of protons needs to be analyzed when the initial spectrum will be known.

One key result regarding the shot-to-shot fluctuations of the proton number is that a random fluctuation in the order of ±30%, for instance, does not result in a dose deviation of ±30%. The reason for this is that shots with too much and too few protons cancel out well for a high laser shot number. For lower shot numbers and small targets these random fluctuations do not compensate each other so well anymore and even ±10% fluctuations may lead to unacceptable qualities because the target is not covered well (TC and D_{min} is affected) or the normal tissue receives an overdosage (CN is affected). However, also in these cases the dose deviations are not in the same order of magnitude as the severity of the fluctuations. Independent

on this result a system with fluctuations in the investigated ranges would not be utilized in clinical routine. Since currently measured fluctuations are in the range of $\pm 30\%$ [68] this study demonstrated that an improvement of the reproducibility of the laser output is essential. Depending on the treated target volumes and the overall required laser shot numbers the shot-to-shot fluctuations have to be controlled to be at least in the range of $\pm 10\%$ or even lower to ensure a correct dose delivery. Moreover, these results stress the need for a beam monitoring device to check the delivered fluence and potentially also the energy spectrum of the delivered bunch in real time.

In general, all studies emphasize the trade-off between the initial proton number per bunch and the required delivery time and how this trade-off influences the dose to the patient. For a lower initial proton number more laser shots are needed, i.e. the delivery takes longer. However, in this case fluctuations are not influencing the dose that much and a device modulating the proton intensity from shot to shot is not urgently necessary. When going to higher initial proton numbers, the required laser shots become less but the quality decreases as well. This could be handled by the use of an intensity modulation device, but even then small fluctuations can vary the dose considerably. Since the studies have been performed for different target sizes and different doses per fraction, it can be stated that larger PTVs certainly increase the shot numbers compared to small PTVs and the prescribed dose per fraction determines the maximal manageable initial proton number per bunch. Hence, laser-driven proton therapy is feasible in future when the proton numbers per bunch are in an acceptable range which certainly depends on the shape of the initial laser produced spectrum. Another open question is whether the high quality laser-driven proton plans can be delivered in short times comparable to conventional proton treatment times or whether the required laser shot numbers constitute a further challenge that may either restrict the patient group or demand for higher repetition rates or other solutions shortening the treatment times.

6

Discussion and perspectives

The results of the planning study have been discussed in section 5.5. This chapter discusses the general feasibility of laser-driven proton therapy including the required beam lines and challenges that came up during the presented thesis additionally to the challenges discussed in chapter 2.3 (e.g. currently low repetition rates of the whole acceleration system, low cut-off energies of the generated proton energy spectra). Since the bunch properties of therapy-relevant laser-accelerated proton spectra are not finally known to date neither an optimal beam line design nor the final dosimetric quality or clinical relevance of laser-driven proton treatments can be stated, yet. However, the presented work aimed to analyze or estimate the feasibility of laser-driven proton therapy in general and potentially provide a feedback for further research either concerning the proton acceleration itself or the development of dedicated beam line designs.

6.1 Discussion

As discussed in section 2.3 laser-driven proton acceleration may offer a compact and cost-efficient acceleration unit for proton therapy, if future laser systems producing therapy-relevant energies can be kept compact as well. Whether this will be achievable has to be demonstrated in the future. Another advantage of laser-driven proton therapy next to its compactness may be given by an optical gantry design guiding the laser through the gantry to the laser target in the treatment head. Given such an optical gantry, heavy bending magnets could be avoided and the laser-driven proton gantry could be kept light and flexible and may fit into conventional treatment bunkers in the clinics. The flexibility of a laser-driven gantry might even be comparable to the robotic CyberKnife system [69] or the gimbaled Vero system with its tilt functions of the treatment head [70] providing a higher number of degrees of freedom for the dose delivery compared to a conventional proton gantry. Besides being flexible and light, the optical gantries may additionally provide benefits concerning tumor motion management (cf. [11]). For example, in a tumor tracking intensity modulated proton therapy session, the scanning motion could be separated from the tracking motion by performing one beam movement with the scanning magnets inside the particle beam line and the other by moving the whole treatment head

of the gantry as described in chapter 3 ("gantry scanning"). This would lead to a simplified control software of the motion adaptation and may constitute advantages for complicated target motions due to the high degrees of freedom of a robotic-like system.

However, to allow for an optical gantry all required beam line elements must be realized in the short treatment head preparing the beam for therapy. Whether this will be practicable depends on the future proton bunches, since the bunch properties determine the required beam line elements (as discussed in chapter 3). Additionally to the mandatory beam line elements, currently it seems likely that an energy selection system (ESS) will be needed to filter desired smaller energy parts of the broad laser-accelerated energy spectrum. Even if the proton bunches will be produced via the radiation pressure acceleration (RPA) scheme yielding quasi-monoenergetic spectra compared to target normal sheath accelerated (TNSA) spectra, an energy selection will be necessary for a high quality proton treatment. Generally, it would be desirable to have a simple beam line with not too much and not too complicated elements. Therefore, it would be ideal to exclude the ESS because of the particles to be dumped and the resultant secondary radiation. An ESS compromises the efficiency of the whole system and requires a good shielding, especially for neutrons. Hence, the optimal proton beam to be generated by the laser should be nearly monoenergetic allowing one to skip the whole ESS. Then, the possibility of having a flexible, light optical gantry would be even more realistic. On the other hand when utilizing the generated spectra directly for treatment, i.e. without any filtering in an ESS, shot-to-shot fluctuations in the bunch creation would imply relevant dose deviations in the patient. In such a case not only the amount of dose may be altered but also the depth dose distribution since the whole energy spectrum may be modified due to the fluctuations. This would require an on-line measurement of the whole energy spectrum of each delivered bunch additional to the measurement of the particle number per bunch which probably will be required anyway. This discussion stresses that for listing the necessary beam line elements including the beam verification devices, the final laser-accelerated bunch properties have to be known as well as the overall reproducibility of the acceleration unit. By then, the feasibility of an optical laser-driven gantry design can be stated and potential benefits concerning motion management can be investigated.

Since the laser acceleration of protons and the development of dedicated beam line designs is still in the early research stage the whole presented feasibility study bases on assumptions like the laser-generated spectrum as well as the utilized beam line and its potential to filter deliverable spectra. Therefore, the carried out treatment planning study represents the beginning of an investigation process where many further steps have to be performed until the feasibility of a laser-driven proton therapy unit can be stated finally. To accomplish this goal the final therapy-relevant spectrum has to be known and a beam line tailored to the exact properties has to be investigated. Given these details and the resulting, deliverable spectra exiting the beam line, a more sophisticated treatment planning study will have to be performed

to finally bring laser-accelerated protons into clinics. To do this, the treatment planning system (TPS) introduced in chapter 4 has to be improved or the whole study needs to be performed with a clinical system. To assimilate LAP-CERR to clinically utilized systems, for example, the implemented optimization should be upgraded by additional clinically used constraints and the option to adapt these constraints in real time during the planning process. Then, even better dose distributions might be obtained. Additionally, the exact phase space information of the deliverable bunches should be included in the TPS. Then, the energy spectra would not have to be approximated and, what is even more relevant, the energy dependent divergence would be incorporated. Certainly, not only the divergency of the incoming bunch should be imported into the TPS but additionally to that the dose calculation should account for divergent beams. With these implemented improvements an advanced planning study could be performed including more patients and more clinical scenarios than the study reported in chapter 5. For instance, one could analyze the resulting plan quality and the required laser shot number depending on the number of utilized beam angles or even test various spot grids for the dose delivery. Since parameters like these were fixed in the performed planning study, plans with even better doses and less shot might be obtained by varying such relevant settings. In the future planning study, not only the planning target volumes but also the organs at risk should be taken into account and the clinical relevance should be developed with a 3D consideration of the plans instead of using generalized evaluation criteria. Moreover, a further planning study could be performed including a dosimetric comparison between laser-driven and conventional proton plans to evaluate the differences and investigate respective advantages. Not until such studies have been performed the final feasibility or clinical relevance of laser-driven proton therapy can be identified. However, such studies are not possible so far since the knowledge about the final spectrum and the final beam line is not existent. Therefore, a first basic treatment planning study was performed in chapter 5 to investigate whether broader energy spectra can yield clinically comparable dosimetric plan qualities at all. Additionally, the study offers a basic orientation about restrictions laser systems for proton therapy must comply with at least when the final conditions resemble the utilized assumptions.

The treatment planning study in this thesis showed that clinically relevant dose distributions can be obtained with the system under consideration for clinical cases. Even when utilizing a TNSA-like broad initial spectrum the deliverable broad energy spectra do not necessarily impair the proton plan quality. It was shown that the broadest possible spectra indeed contributed with approximately 50% to the final dose distribution demonstrating that good proton plans comparable to clinically treated proton plans could be achieved. However, the required delivery times were found to be relatively long even under the assumption of a 10 Hz laser system and, hence, are not comparable to state-of-the-art proton treatment times. Certainly, the elaborated treatment times as well as the established manageable ranges of the initial proton number depend strongly on the assumed laser-produced spectrum,

and therefore, may change for a different initial spectrum. However, the deliverable spectra used for the actual study were mainly defined by the beam line and especially by the ESS. If in future a RPA spectrum will be imported into a similar beam line the shapes of the filtered spectra will not change significantly but only the contained proton number would adapt accordingly. Consequently, the ranges of the initial proton number established in this treatment planning study would also adjust depending on the integral proton number contained in one bunch.

However, the amount of dumped protons would change by utilizing a narrower laser-accelerated bunch spectrum. This would be beneficial on the one hand when considering the shielding material that has to be integrated in the beam line. On the other hand, less neutrons or secondary particles would be produced decreasing the extra amount of radiation for the patient in the treatment room. Concerning the secondary radiation, a proton spectrum as narrow as possible would always be preferable and the utilized TNSA-like spectrum represents the worst case scenario. Therefore, the amount of protons to be dumped is high anyway for such a broad initial spectrum, and hence, the exact proton number to be dumped is not analyzed at all in this thesis. When the future spectrum reaching therapy-relevant energies is known such an analysis is essential for the feasibility of laser-driven proton therapy not only to account for the required shielding material but also to estimate whether an additional intensity modulation from shot to shot may be possible concerning the extra amount of blocked particles (as discussed in chapter 5.5). Nevertheless, all produced laser-driven proton plans in this thesis rely on the axial-layer-based dose delivery (introduced in section 2.2) being efficient in terms of utilizing as broad as possible spectra for the treatment and resulting in less protons to be dumped compared to a delivery of only nearly monoenergetic Bragg peaks. However, such a dose delivery represents a new challenge for the future beam line design which could be solved with the gantry design used for this study in theory. This challenge concerns the transport of a broad energy spectrum (in this study bandwidths up to $\Delta E/E = 24\%$ could be transported) through the beam line to the patient. This is certainly more complicated than the transport of monoenergetic beams, especially when the beam line should be designed to transport various desirable nominal energies with different bandwidths and to focus all filtered energies to the same focal spot (achromatic beam line). When the future beam line could only transport bandwidths of, for instance, up to 10%, this would not affect the resulting plan quality but the overall required delivery time since the dose delivered per shot is reduced for a narrower energy spectrum. This means, delivering broad energy spectra to the patient not only decreases the produced amount of secondary radiation but additionally may reduce the overall required laser shot number to a certain extend. Another challenge may be the delivery of larger beam widths (up to about 2 cm FWHM). In chapter 5 it was demonstrated that a variation of the lateral beam width could be utilized to handle high proton numbers per bunch to down-regulate the delivered fluences. If this is required in the future, the beam line must provide an active beam shaping via changing the magnetic field strengths of quadrupoles to vary the fluence and the beam width. If such a beam shaping would be performed passively by blocking

parts of the beam it would not reduce the fluence in the center of the field and, therefore, would not result in the delivery of the same amount of protons to another area within the target.

Therefore, the treatment planning study demonstrated that high quality proton plans can be obtained by laser-driven protons when specific restrictions can be met. From the laser point of view, the proton number per bunch has to be controlled as well as the reproducibility of the whole system. Furthermore, a high repetition rate of at least 10 Hz seems to be required to keep the treatment times low. The beam line must cope with broad energy spectra and an active beam width manipulation would be necessary depending on the final energy spectrum. From the therapy point of view it seems likely that the total shot number has to be decreased or low shot proton plans have to yield a better dose distribution to shorten the delivery times for future proton therapy. This could be achieved for example by introducing an intensity modulation from shot to shot, but it has to be proven whether the shots can be reduced sufficiently in the final design. However, as mentioned many times before, the feasibility and the final beam line strongly depend on the generated laser-driven bunches and it may happen that all stated values or ranges may be alleviated or even strengthened. Otherwise, the found restrictions are no strict arguments against laser-driven proton therapy but only demand for a clever way of handling them since the presented dose distributions yielded with laser-driven protons promise a good quality comparable to conventional proton therapy qualities.

6.2 Perspectives

Since neither the laser-driven proton therapy unit nor the final optimal dose delivery is settled so far new concepts might be developed or investigated to potentially bring laser-accelerated protons closer towards cancer therapy. In this section potential perspectives are given for further investigations which could not be elaborated in detail during this thesis but which may improve particular issues of a laser-driven proton therapy unit.

It was discussed that the ESS has to be compact and light to fit in the short treatment head of an optical gantry. One way to realize this could be by utilizing two magnetic quadrupoles and an additional pinhole collimator. Such a quadrupole doublet represents a magnetic lens focusing a certain energy of a divergent polyenergetic proton beam to a focal point behind the second quadrupole. By arranging a pinhole collimator at the location of the focal point a small energy window can be selected with such a system. Given a fixed field gradient of the quadrupoles different energies can be focused to different focal spots by modifying the distance between the quadrupoles and adapting the location of the pinhole collimator. Thus, by installing the second quadrupole and the collimator on a motor-driven mount the required distances can be chosen and the desired energies can be selected. The

bandwidth of the filtered spectrum can be adjusted by adapting the aperture size of the collimator. Depending on the initial spectrum such an ESS might be sufficient to constitute a simple and compact solution for an optical gantry beam line.

The other presented concepts target on reducing the required overall shot number per proton plan. One simple way, already mentioned before, is the use of variable beam widths per plan. Especially when the fluence per bunch is high a part of the whole dose could be delivered with large beams to a large volume of the tumor and by decreasing the beam width smaller parts of the tumor could be irradiated separately with additional laser shots to perform a form of an intensity modulation. This means for example, a fundamental dose might be delivered to the whole target and the areas with underdose might be filled-up with dose by utilizing smaller beams. Especially for big tumors, this might require less laser shots compared to a delivery with a fix beam width.

Concerning the dose delivery another way to decrease the shot number might be the delivery of more spots or clusters on the same pencil beam within one laser shot. If the gantry position is fixed and the scanning magnets are adjusted to deliver the protons to a certain area in the target, in general more shots are delivered with this setting since usually various spots in different depths have been placed along the pencil beam with the given beam direction. If the whole dose for this pencil beam or at least a larger part of this dose could be delivered with one laser shot the total required shot number can be reduced. One example would be the delivery of three filtered spectra at three different nominal energies which would be delivered with three laser shots but the same gantry and scanning magnets configuration. If the ESS could select all three spectra from the same initial spectrum the whole dose could be delivered within one shot instead of three. This would not only save delivery time but also decrease the produced secondary radiation since a larger portion of the initial spectrum is utilized for treatment and less protons are dumped in general by utilizing less shots. To do this, the filtering of spectra has to be performed with a special type of an ESS. One solution could be the chicane ESS with four static dipole fields (presented in chapter 3) and an multileaf collimator in the center of the ESS [71]. This multileaf collimator can select more parts than just one from the central plane and, hence, more small spectra are filtered and guided to the patient. On the one hand this concept used the undesirable chicane ESS dumping a high proton number, however, on the other side by filtering more parts than just one, the amount of secondary radiation produced there might be decreased a lot. By additionally modulating the proton number per filtered energy in the central plane of the ESS (e.g. by introducing scattering material of variable thickness dependent on the position) a spread out Bragg peak can be produced with such an ESS which will be delivered to the patient within one laser shot [50].

Summary and conclusion

7.1 Summary

The purpose of this thesis was to investigate the feasibility of laser-driven proton therapy and to optimize the composition of the required beam lines tailored to the specific properties of laser-accelerated protons. The beams which are generated when a high power laser impinges onto a thin target are pulsed with very short bunch durations. These bunches probably have a broad energy spectrum (broader than monoenergetic) and contain a high proton number. Therefore, new challenges arise for transporting such a proton beam to the patient and prepare it for therapy. Depending on the final bunch properties, which remain unclear at this point, specific beam line elements have to be used to realize this goal. Diverse devices have been discussed that may be necessary in a laser-driven beam line for therapy such as an energy selection system, for instance, filtering a smaller part of the spectrum to allow for a high quality treatment. Another beam preparation device is a fluence selection system that might be required to down-regulate the proton number delivered to a certain area within the tumor if the proton number per bunch is higher than neces-sary to deliver the prescribed dose. These two devices represent the most important ones for the beam modification, however, are the most crucial ones as well. The mentioned devices rely on blocking of portions of the beam and thus demand a good shielding of the produced secondary radiation, which may constitute a challenge for future designs. The shielding as well as the need to include many elements in the beam line may restrict the feasibility of a flexible optical gantry design, guiding the laser to the short treatment head at the end of the gantry where the whole beam line composition is installed. Since the final beam properties are not established neither the required devices nor the required amount of shielding material can be stated at this point and, therefore, the feasibility of an optical laser-driven gantry remains questionable. However, it was shown in this work that in theory a compact gantry beam line based on pulsed powered magnets can capture, process and trans-port laser-driven proton bunches to perform high quality radiation therapy. With this theoretical beam line guiding the proton beam through the whole gantry design (instead of the laser) a treatment planning study was performed using a planning system designed for laser-driven beams and real clinical patient data. It was found

that when only full laser shots, i.e. full proton bunches, can be delivered to the patient, the accelerated proton number per bunch yielding good quality proton plans is strongly restricted. A too high proton number delivers too much dose with one shot but with a too low proton number per bunch many laser shots are required to accumulate the prescribed dose in the tumor leading to unacceptable long delivery times. By modulating the intensity, i.e. the proton number per bunch, from shot to shot, a higher initial proton number can be handled with the beam line and leads to clinically acceptable treatment plans as the modulation device in the beam line can down-regulate the proton number in the delivered bunches. This shows that the accelerated proton number per bunch has to be kept under control and must stay within a certain range. The manageable range to allow for high quality proton therapy depends not only on the generated energy spectrum of the bunch but also on the final beam line, the tumor sizes to be treated and the prescribed doses per treatment fraction. Besides the bunch properties, the obtained proton plan parameters have been analyzed and especially the required treatment times. To deliver standard doses (2 Gy per fraction) to standard tumor sizes the integer shot proton plans require about 16 min to deliver the dose to the tumor when assuming an optimistic repetition rate of 10 Hz. Such a delivery time is barely at the limit of clinical relevance since it is far longer compared to conventional proton delivery times (in the order of 3 min). When the bunch intensity can be modulated in the beam line from shot to shot, the treatment times could be reduced for the clinical standard case to approximately 6 min. This points out that a modulation of the bunch intensity might be necessary to yield acceptable treatment times comparable to conventional treatment times. An additional analysis showed that the currently existing shot-to-shot fluctuations ($\pm 30\%$ up to $\pm 100\%$) in the produced bunches impair the plan quality significantly when proton plans with few shots, i.e. short delivery times, would be delivered. Since the future goal is to reduce the required laser shots per plan, the reproducibility of the proton bunches has to be warranted in such a way that the proton number fluctuations are at least in the order of $\pm 10\%$ or even lower to allow for a reproducible and safe, high quality proton treatment.

7.2 Conclusion

To conclude, this work demonstrates that the feasibility of laser-driven proton therapy strongly depends on the final beam properties and the future beam lines tailored to these beams. It was shown, however, that the investigated example utilizing a broad, exponentially decaying energy spectrum and a compact pulsed powered gantry beam line yielded clinically relevant, high quality proton plans comparable to conventional proton plan qualities. This means, broad energy spectra do not necessarily impair the dose distribution optimized for real patient anatomies but only the delivery times in laser-accelerated proton therapy might be longer than in conventional proton therapy. As soon as a beam line is developed for the finally established proton beam the issue concerning the delivery time can be addressed along with the final amount of produced secondary radiation yielding potentially a way of decreasing the time for a laser-driven treatment fraction further.

In order to bring laser-driven proton therapy into the clinics further research has to be performed focusing on a reproducible energy spectrum of therapy-relevant energies with, at best, a narrow bandwidth to decrease the produced secondary radiation within the beam line. Additionally, the accelerated proton number per bunch has to be controlled and the repetition rate of the whole system has to be in the order of 10 Hz or higher to keep the delivery times acceptable. If this is the case, the required elements which are necessary to prepare the beam for therapy can be elaborated finally and further dosimetric studies can be carried out adjudicating on the feasibility of the final therapy unit. Finally, this work demonstrated that further research in this field is worthwhile since in theory laser-driven proton therapy can be comparable to state-of-the-art proton therapy. Thus, laser acceleration of protons might offer proton therapy to more cancer patients in the future by installing and operating potentially compact and less expensive proton (or ion) beam therapy units in more facilities worldwide.

Appendix

A

Lists

A.1 List of Figures

A.2 List of Tables

B

Bibliography

[1] R. R. Wilson. Radiological use of fast protons. *Radiology*, 47(5):487–491, 1946.

[2] A. J. Lomax, T. Bortfeld, G. Goitein, J. Debus, C. Dykstra, P.-A. Tercier, P. A. Coucke, and R. O. Mirimanoff. A treatment planning inter-comparison of proton and intensity modulated photon radiotherapy. *Radiotherapy and Oncology*, 51(3):257–271, 1999.

[3] H. Paganetti. Relative biological effectiveness (RBE) values for proton beam therapy. Variations as a function of biological endpoint, dose, and linear energy transfer. *Physics in Medicine and Biology*, 59(22):R419–R472, 2014.

[4] A. R. Smith. Proton therapy. *Physics in Medicine and Biology*, 51(13):R491–R504, 2006.

[5] A. Lomax. Intensity modulation methods for proton radiotherapy. *Physics in Medicine and Biology*, 44(1):185–205, 1999.

[6] A. R. Smith. Vision 20/20: Proton therapy. *Medical Physics*, 36(2):556–568, 2009.

[7] J. M. Schippers and A. J. Lomax. Emerging technologies in proton therapy. *Acta Oncologica*, 50(6):838–850, 2011.

[8] D. L. Friesel and T. A. Antaya. Medical cyclotrons. *Reviews of Accelerator Science and Technology*, 2(01):133–156, 2009.

[9] G. J. Caporaso, Y.-J. Chen, and S. E. Sampayan. The dielectric wall accelerator. *Reviews of Accelerator Science and Technology*, 2(01):253–263, 2009.

[10] S. Schell. *Dose delivery and treatment planning methods for efficient radiation therapy with laser-driven particle beams*. PhD thesis, Technische Universität München, 2011.

[11] K. M. Hofmann, S. Schell, and J. J. Wilkens. Laser-driven beam lines for delivering intensity modulated radiation therapy with particle beams. *Journal of Biophotonics*, 5(11-12):903–911, 2012.

[12] E. Clark, K. Krushelnick, M. Zepf, F. N. Beg, M. Tatarakis, A. Machacek, Santala M. I. K., I. Watts, P. A. Norreys, and A. E. Dangor. Energetic heavy-ion and proton generation from ultraintense laser-plasma interactions with solids. *Physical Review Letters*, 85(8):1654–1657, 2000.

[13] R. A. Snavely, M. H. Key, S. P. Hatchett, T. E. Cowan, M. Roth, T. W. Phillips, M. A. Stoyer, E. A. Henry, T. C. Sangster, M. S. Singh, S. C. Wilks, A. MacKinnon, A. Offenberger, D. M. Pennington, K. Yasuike, A. B. Langdon, B. F. Lasinski, J. Johnson, M. D. Perry, and E. M. Campbell. Intense high-energy proton beams from petawatt-laser irradiation of solids. *Physical Review Letters*, 85(14):2945–2948, 2000.

[14] A. Macchi, M. Borghesi, and M. Passoni. Ion acceleration by superintense laser-plasma interaction. *Reviews of Modern Physics*, 85(2):751–793, 2013.

[15] K. W. D. Ledingham, P. R. Bolton, N. Shikazono, and C.-M. Ma. Towards laser driven hadron cancer radiotherapy: A review of progress. *Applied Sciences*, 4(3):402–443, 2014.

[16] M. Borghesi. Laser-driven ion acceleration: State of the art and emerging mechanisms. *Nuclear Instruments and Methods in Physics Research Section A: Accelerators, Spectrometers, Detectors and Associated Equipment*, 740:6–9, 2014.

[17] M. S. Schollmeier. *Optimization and control of laser-accelerated proton beams.* PhD thesis, Technische Universität Darmstadt, 2008.

[18] A. Henig. *Advanced Approaches to High Intensity Laser-Driven Ion Acceleration.* PhD thesis, Ludwig-Maximilians-Universität Müchen, 2010.

[19] S. C. Wilks, A. B. Langdon, T. E. Cowan, M. Roth, M. Singh, S. Hatchett, M. H. Key, D. Pennington, A. MacKinnon, and R. A. Snavely. Energetic proton generation in ultra-intense laser–solid interactions. *Physics of Plasmas*, 8(2):542–549, 2001.

[20] T. Tajima, D. Habs, and X. Yan. Laser acceleration of ions for radiation therapy. *Reviews of Accelerator Science and Technology*, 02(01):201–228, 2009.

[21] J. Fuchs, P. Antici, E. d'Humières, E. Lefebvre, M. Borghesi, E. Brambrink, C. A. Cecchetti, M. Kaluza, V. Malka, M. Manclossi, P. Meyroneinc, P. Mora, J. Schreiber, T. Toncian, H. Pépin, and P. Audebert. Laser-driven proton scaling laws and new paths towards energy increase. *Nature Physics*, 2(1):48–54, 2006.

[22] A. P. L. Robinson, M. Zepf, S. Kar, R. G. Evans, and C. Bellei. Radiation pressure acceleration of thin foils with circularly polarized laser pulses. *New Journal of Physics*, 10(1):013021, 2008.

[23] T. Esirkepov, M. Borghesi, S. V. Bulanov, G. Mourou, and T. Tajima. Highly efficient relativistic-ion generation in the laser-piston regime. *Physical Review Letters*, 92(17):175003, 2004.

[24] A. Henig, S. Steinke, M. Schnürer, T Sokollik, R. Hörlein, D. Kiefer, D. Jung, J. Schreiber, B. M. Hegelich, X. Q. Yan, J. Meyer-ter Vehn, T. Tajima, P. V. Nickles, W. Sandner, and D. Habs. Radiation-pressure acceleration of ion beams driven by circularly polarized laser pulses. *Physical Review Letters*, 103(24):245003, 2009.

[25] S. Kar, K. F. Kakolee, B. Qiao, A. Macchi, M. Cerchez, D. Doria, M. Geissler, P. McKenna, D. Neely, J. Osterholz, R. Prasad, K. Quinn, B. Ramakrishna, G. Sarri, O. Willi, X. Y. Yuan, M. Zepf, and M. Borghesi. Ion acceleration in multispecies targets driven by intense laser radiation pressure. *Physical Review Letters*, 109(18):185006, 2012.

[26] B. M. Hegelich, D. Jung, B. J. Albright, M. Cheung, B. Dromey, D. C. Gautier, C. Hamilton, S. Letzring, R. Munchhausen, S. Palaniyappan, R. Shah, H.-C. Wu, L. Yin, and J. C. Fernández. 160 MeV laser-accelerated protons from CH2 nano-targets for proton cancer therapy. *arXiv:1310.8650*, 2013.

[27] B. M. Hegelich, I. Pomerantz, L. Yin, H. C. Wu, D. Jung, B. J. Albright, D. C. Gautier, S. Letzring, S. Palaniyappan, R. Shah, K. Allinger, R. Hörlein, J. Schreiber, D. Habs, J. Blakeney, G. Dyer, L. Fuller, E. Gaul, E. Mccary, A. R. Meadows, C. Wang, T. Ditmire, and J. C. Fernandez. Laser-driven ion acceleration from relativistically transparent nanotargets. *New Journal of Physics*, 15(8):085015, 2013.

[28] M. Goitein, A. J. Lomax, and E. S. Pedroni. Treating cancer with protons. *Physics Today*, 55(9):45–50, 2002.

[29] S. V. Bulanov and V. S. Khoroshkov. Feasibility of using laser ion accelerators in proton therapy. *Plasma Physics Reports*, 28(5):453–456, 2002.

[30] E. Fourkal, B. Shahine, M. Ding, J. S. Li, T. Tajima, and C.-M. Ma. Particle in cell simulation of laser-accelerated proton beams for radiation therapy. *Medical Physics*, 29(12):2788–2798, 2002.

[31] U. Linz and J. Alonso. What will it take for laser driven proton accelerators to be applied to tumor therapy? *Physical Review Special Topics - Accelerators and Beams*, 10(9):094801, 2007.

[32] A. Peeters, J. P. C. Grutters, M. Pijls-Johannesma, S. Reimoser, D. Ruysscher, J. L. Severens, M. A. Joore, and P. Lambin. How costly is particle therapy? Cost analysis of external beam radiotherapy with carbon-ions, protons and photons. *Radiotherapy and Oncology*, 95(1):45–53, 2010.

[33] S. E. Combs, O. Jäkel, T. Haberer, and J. Debus. Particle therapy at the Heidelberg Ion Therapy Center (HIT) – Integrated research-driven university-hospital-based radiation oncology service in Heidelberg, Germany. *Radiotherapy and Oncology*, 95(1):41–44, 2010.

[34] E. Pedroni, R. Bearpark, T. Böhringer, A. Coray, J. Duppich, S. Forss, D. George, M. Grossmann, G. Goitein, C. Hilbes, M. Jermann, S. Lin, A. Lomax, M. Negrazus, M. Schippers, and G. Kotrle. The PSI gantry 2: A second generation proton scanning gantry. *Zeitschrift für Medizinische Physik*, 14(1):25–34, 2004.

[35] C.-M. Ma, I. Veltchev, E. Fourkal, J. S. Li, W. Luo, J. Fan, T. Lin, and A. Pollack. Development of a laser-driven proton accelerator for cancer therapy. *Laser Physics*, 16(4):639–646, 2006.

[36] J. Bin, K. Allinger, W. Assmann, G. Dollinger, G. A. Drexler, A. A. Friedl, D. Habs, P. Hilz, R. Hoerlein, N. Humble, S. Karsch, K. Khrennikov, D. Kiefer, F. Krausz, W. Ma, D. Michalski, M. Molls, S. Raith, S. Reinhardt, B. Röper, T. E. Schmid, T. Tajima, J. Wenz, O. Zlobinskaya, J. Schreiber, and J. J. Wilkens. A laser-driven nanosecond proton source for radiobiological studies. *Applied Physics Letters*, 101(24):243701, 2012.

[37] A. Yogo, T. Maeda, T. Hori, H. Sakaki, K. Ogura, M. Nishiuchi, A. Sagisaka, H. Kiriyama, H. Okada, S. Kanazawa, T. Shimomura, Y. Nakai, M. Tanoue, F. Sasao, P. R. Bolton, M. Murakami, T. Nomura, S. Kawanishi, and K. Kondo. Measurement of relative biological effectiveness of protons in human cancer cells using a laser-driven quasimonoenergetic proton beamline. *Applied Physics Letters*, 98(5):053701, 2011.

[38] K. Zeil, M. Baumann, E. Beyreuther, T. Burris-Mog, T. E. Cowan, W. Enghardt, L. Karsch, S. D. Kraft, L. Laschinsky, J. Metzkes, D. Naumburger, M. Oppelt, C. Richter, R. Sauerbrey, M. Schürer, U. Schramm, and J. Pawelke. Dose-controlled irradiation of cancer cells with laser-accelerated proton pulses. *Applied Physics B*, 110(4):437–444, 2013.

[39] T. Bortfeld, S. B. Jiang, and E. Rietzel. Effects of motion on the total dose distribution. *Seminars in Radiation Oncology*, 14:41–51, 2004.

[40] W. Leemans, W. Chou, and M. Uesaka. Beam Dynamics Newsletter: No. 56, December 2011. http://icfa-usa.jlab.org/.

[41] P. R. Bolton, M. Borghesi, C. Brenner, D. C. Carroll, C. de Martinis, A. Flacco, V. Floquet, J. Fuchs, P. Gallegos, D. Giove, J. S. Green, S. Green, B. Jones, D. Kirby, P. McKenna, D. Neely, F. Nuesslin, R. Prasad, S. Reinhardt, M. Roth, U. Schramm, G. G. Scott, S. Ter-Avetisyan, M. Tolley, G. Turchetti, and J. J. Wilkens. Instrumentation for diagnostics and control of laser-accelerated proton (ion) beams. *Physica Medica*, 30(3):255–270, 2014.

[42] E. Fourkal, J. S. Li, M. Ding, T. Tajima, and C.-M. Ma. Particle selection for laser-accelerated proton therapy feasibility study. *Medical Physics*, 30(7):1660–1670, 2003.

[43] W. Luo, E. Fourkal, J. Li, and C.-M. Ma. Particle selection and beam collimation system for laser-accelerated proton beam therapy. *Medical Physics*, 32(3):794–806, 2005.

[44] T. Toncian, M. Borghesi, J. Fuchs, E. d'Humières, P. Antici, P. Audebert, E. Brambrink, C. A. Cecchetti, A. Pipahl, L. Romagnani, and O. Willi. Ultra-fast laser-driven microlens to focus and energy-select mega-electron volt protons. *Science*, 312(5772):410–413, 2006.

[45] J. H. Bin, W. J. Ma, K. Allinger, H. Y. Wang, D. Kiefer, S. Reinhardt, P. Hilz, K. Khrennikov, S. Karsch, X. Q. Yan, F. Krausz, T. Tajima, D. Habs, and J. Schreiber. On the small divergence of laser-driven ion beams from nanometer thick foils. *Physics of Plasmas*, 20(7):073113, 2013.

[46] S. Kar, K. Markey, P. T. Simpson, C. Bellei, J. S. Green, S. R. Nagel, S. Kneip, D. C. Carroll, B. Dromey, L. Willingale, E. L. Clark, P. McKenna, Z. Najmudin, K. Krushelnick, P. Norreys, R. J. Clarke, D. Neely, M. Borghesi, and M. Zepf. Dynamic control of laser-produced proton beams. *Physical Review Letters*, 100(10):105004, 2008.

[47] T. Burris-Mog, K. Harres, F. Nürnberg, S. Busold, M. Bussmann, O. Deppert, G. Hoffmeister, M. Joost, M. Sobiella, A. Tauschwitz, B. Zielbauer, V. Bagnoud, T. Herrmannsdoerfer, M. Roth, and T. E. Cowan. Laser accelerated protons captured and transported by a pulse power solenoid. *Physical Review Special Topics - Accelerators and Beams*, 14(12):121301, 2011.

[48] I. Hofmann, J. Meyer-ter Vehn, X. Yan, A. Orzhekhovskaya, and S. Yaramy-shev. Collection and focusing of laser accelerated ion beams for therapy applications. *Physical Review Special Topics - Accelerators and Beams*, 14(3):031304, 2011.

[49] M. Schollmeier, S. Becker, M. Geißel, K. A. Flippo, A. Blažević, S. A. Gaillard, D. C. Gautier, F. Grüner, K. Harres, M. Kimmel, F. Nürnberg, P. Rambo, U. Schramm, J. Schreiber, J. Schütrumpf, J. Schwarz, N. A. Tahir, B. Atherton, D. Habs, B. M. Hegelich, and M. Roth. Controlled transport and focusing of laser-accelerated protons with miniature magnetic devices. *Physical Review Letters*, 101(5):055004, 2008.

[50] S. Schell and J. J. Wilkens. Modifying proton fluence spectra to generate spread-out bragg peaks with laser accelerated proton beams. *Physics in Medicine and Biology*, 54(19):N459–N466, 2009.

[51] S. Schell and J. J. Wilkens. Dosimetric effects of energy spectrum uncertainties in radiation therapy with laser-driven particle beams. *Physics in Medicine and Biology*, 57(5):N47–N53, 2012.

[52] S. Faby and J. J. Wilkens. Assessment of secondary radiation and radiation protection in laser-driven proton therapy. *Zeitschrift für Medizinische Physik*, 2014. doi:10.1016/j.zemedi.2014.09.002.

[53] U. Masood, M. Bussmann, T. E. Cowan, W. Enghardt, L. Karsch, F. Kroll, U. Schramm, and J. Pawelke. A compact solution for ion beam therapy with laser accelerated protons. *Applied Physics B*, 117:41–52, 2014.

[54] J. O. Deasy, A. I. Blanco, and V. H. Clark. CERR: A computational environment for radiotherapy research. *Medical Physics*, 30(5):979–985, 2003.

[55] F. Kamp. *Uncertainties in biological dose response models and their integration in treatment planning of carbon ion therapy*. PhD thesis, Technische Universität München, 2015.

[56] S. Nill. *Development and application of a multi-modality inverse treatment planning system*. PhD thesis, Universität Heidelberg, 2001.

[57] R. L. Siddon. Calculation of the radiological depth. *Medical Physics*, 12(1):84–87, 1985.

[58] T. Bortfeld. An analytical approximation of the bragg curve for therapeutic proton beams. *Medical Physics*, 24(12):2024–2033, 1997.

[59] B. Gottschalk, A. M. Koehler, R. J. Schneider, J. M. Sisterson, and M. S. Wagner. Multiple coulomb scattering of 160 MeV protons. *Nuclear Instruments and Methods in Physics Research Section B: Beam Interactions with Materials and Atoms*, 74(4):467–490, 1993.

[60] S. Nill, T. Bortfeld, and U. Oelfke. Inverse planning of intensity modulated proton therapy. *Zeitschrift für Medizinische Physik*, 14(1):35–40, 2004.

[61] M. A. Chanrion, F. Ammazzalorso, A. Wittig, R. Engenhart-Cabillic, and U. Jelen. Dosimetric consequences of pencil beam width variations in scanned beam particle therapy. *Physics in Medicine and Biology*, 58(12):3979–3993, 2013.

[62] N. J. Lomax and S. G. Scheib. Quantifying the degree of conformity in radiosurgery treatment planning. *International Journal of Radiation Oncology*Biology*Physics*, 55(5):1409–1419, 2003.

[63] A. Grzadziel, A.-L. Grosu, and P. Kneschaurek. Three-dimensional conformal versus intensity-modulated radiotherapy dose planning in stereotactic radiotherapy: Application of standard quality parameters for plan evaluation.

International Journal of Radiation Oncology*Biology*Physics, 66(4):S87–S94, 2006.

[64] M. Krämer, O. Jäkel, T. Haberer, G. Kraft, D. Schardt, and U. Weber. Treatment planning for heavy-ion radiotherapy: Physical beam model and dose optimization. *Physics in Medicine and Biology*, 45(11):3299–3317, 2000.

[65] F. Kamp. Comparison of the lateral dose fall-off for proton and ion beams in radiation therapy. Master's thesis, Technische Universität München, 2011.

[66] S. Schell and J. J. Wilkens. Advanced treatment planning methods for efficient radiation therapy with laser accelerated proton and ion beams. *Medical Physics*, 37(10):5330–5340, 2010.

[67] A. J. Lomax, T. Böhringer, A. Bolsi, D. Coray, F. Emert, G. Goitein, M. Jermann, S. Lin, E. Pedroni, H. Rutz, O. Stadelmann, B. Timmermann, J. Verwey, and D. C. Weber. Treatment planning and verification of proton therapy using spot scanning: Initial experiences. *Medical Physics*, 31(11):3150–3157, 2004.

[68] S. D. Kraft, C. Richter, K. Zeil, M. Baumann, E. Beyreuther, S. Bock, M. Bussmann, T. E. Cowan, Y. Dammene, W. Enghardt, U. Helbig, L. Karsch, T. Kluge, L. Laschinsky, E. Lessmann, J. Metzkes, D. Naumburger, R. Sauerbrey, M. Schürer, M. Sobiella, J. Woithe, U. Schramm, and J. Pawelke. Dose-dependent biological damage of tumour cells by laser-accelerated proton beams. *New Journal of Physics*, 12(8):085003, 2010.

[69] J. R. Adler Jr., S. D. Chang, M. J. Murphy, J. Doty, P. Geis, and S. L. Hancock. The Cyberknife: A frameless robotic system for radiosurgery. *Stereotactic and Functional Neurosurgery*, 69(1-4):124–128, 1997.

[70] Y. Kamino, K. Takayama, M. Kokubo, Y. Narita, E. Hirai, N. Kawawda, T. Mizowaki, Y. Nagata, T. Nishidai, and M. Hiraoka. Development of a four-dimensional image-guided radiotherapy system with a gimbaled X-ray head. *International Journal of Radiation Oncology* Biology* Physics*, 66(1):271–278, 2006.

[71] G. Kraft, U. Weber, S. Kraft, and S. Kraft. Energy filter device. US Patent 7,482,605.

List of publications

Papers in journals

First author

- <u>K. M. Hofmann</u>, U. Masood, J. Pawelke, J. J. Wilkens: "A treatment planning study to assess the feasibility of laser-driven proton therapy using a compact gantry design", Med. Phys. *tentatively accepted*, 2015.

- <u>K. M. Hofmann</u>, S. Schell, J. J. Wilkens: "Laser-driven beam lines for delivering intensity modulated radiation therapy with particle beams", J. Biophotonics 5(11,12), 903-911, 2012.

Coauthor

- U. Masood, <u>K. M. Hofmann</u>, M. Bussmann, T. E. Cowan, W. Enghardt, L. Karsch, F. Kroll, U. Schramm, J. J. Wilkens, J. Pawelke: "A compact proton therapy system with a novel short-throw beam scanning system for laser accelerated beams", Phys. Med. Biol. *in preparation*, 2015.

Papers in books and conference proceedings

First author

- <u>K. M. Hofmann</u>, U. Masood, J. Pawelke, J. J. Wilkens: "A treatment planning study to assess the feasibility and the limitations of laser-driven proton therapy", in: S. Klöck (ed.) Joint Conference of the SSRMP, DGMP, ÖGMP: Dreiländertagung der Medizinischen Physik (Zurich/Switzerland), ISBN 978-3-9816508-5-3, p. 29, 2014 (oral presentation).

- <u>K. Hofmann</u>, U. Masood, J. Pawelke, J. Wilkens: "Feasibility and Limitations of Laser-Driven Proton Therapy: A Treatment Planning Study", Med. Phys. 41(6), p. 112, 2014 (oral presentation).

- <u>K. M. Hofmann</u>, S. Schell, J. J. Wilkens: "Laser-driven beam lines for delivering intensity modulated radiation therapy with particle beams", in: D. Margarone, P. Cirrone, G. Cuttone, G. Korn (eds.): 2nd ELIMED Workshop and Panel 2012, AIP Conference Proceedings, Vol. 1546, ISBN 978-0-7354-1171-5 (American Institute of Physics Publishing LLC: Melville, New York), 81-83, 2013 (oral presentation).

- <u>K. Hofmann</u>, A. Krauss, S. Nill, U. Oelfke: "A Comparison of Step-And-Shot and DMLC IMRT-Delivery for Real-Time Tumor Tracking", Med. Phys. 38(6), pp. 3782-3783, 2011 (oral presentation given by A. Krauss).

Coauthor

- M. Gotz, M. Baumann, W. Enghardt, <u>K. Hofmann</u>, L. Karsch, F. Kroll, U. Masood, U. Schramm, M. Schürer, J. J. Wilkens, J. Pawelke: "Status report on compact laser driven ion beam therapy facility development via a pulse powered gantry system", Annual Conference of the Particle Therapy Co-Operative Group, 2015 (poster).

- U. Masood, M. Baumann, M. Bussmann, T.E. Cowan, W. Enghardt, T. Herrmannsdörfer, <u>K. M. Hofmann</u>, L. Karsch, F. Kroll, U. Schramm, M. Schürer, J. J. Wilkens, J. Pawelke: "Development of a novel laser-driven ion beam therapy system with pulsed compact gantry", Space Radiation and Heavy Ions in Therapy Symposium, 2015 (poster).

- U. Masood, M. Baumann, M. Bussmann, T.E. Cowan, W. Enghardt, T. Herrmannsdörfer, <u>K. M. Hofmann</u>, L. Karsch, F. Kroll, U. Schramm, M. Schürer, J. J. Wilkens, J. Pawelke: "Development of the first pulse powered compact gantry system for a novel laser driven ion beam therapy", International Congress of Radiation Research, 2015 (poster).

- U. Masood, M. Baumann, M. Bussmann, T. E. Cowan, W. Enghardt, T. Herrmannsdörfer, <u>K. M. Hofmann</u>, L. Karsch, F. Kroll, U. Schramm, M. Schürer, J. J. Wilkens, J. Pawelke: "Development of the first pulse powered radiotherapy gantry system for a novel compact laser driven ion beam therapy", Radiotherapy & Oncology 115 (Suppl. 1) p. S127, 2015 (oral presentation).

- U. Masood, M. Bussmann, T. E. Cowan, W. Enghardt, T. Herrmannsdörfer, <u>K. M. Hofmann</u>, L. Karsch, F. Kroll, U. Schramm, M. Schürer, J. J. Wilkens, J. Pawelke: "Development of the pulse powered gantry system for laser driven proton therapy", in: SPIE 2015 Optics+Optoelectronics 9514-53, p. 166, 2015 (oral presentation).

- U. Masood, M. Bussmann, M. Baumann, T. E. Cowan, W. Enghardt, T. Herrmannsdörfer, <u>K. M. Hofmann</u>, M. Kaluza, L. Karsch, F. Kroll, U. Schramm, M. Schürer, J. J. Wilkens, J. Pawelke: "Development of a Compact Particle Therapy Facility with Laser-driven Ion Beams via Novel Pulse Powered Gantry Systems", in: S. Klöck (ed.) Joint Conference of the SSRMP, DGMP, ÖGMP: Dreiländertagung der Medizinischen Physik (Zurich/Switzerland), ISBN 978-3-9816508-5-3, pp. 27-8, 2014 (oral presentation).

- U. Masood, M. Baumann, M. Bussmann, T. Cowan, W. Enghardt, T. Herrmannsdoerfer, <u>K. Hofmann</u>, M. Kaluza, L. Karsch, F. Kroll, U. Schramm, M. Schuerer, J. Wilkens, J. Pawelke: "Development of a Novel Compact Particle Therapy Facility With Laser Driven Ion Beams via Gantry Systems Based on Pulsed Magnets", International Journal of Radiation Oncology, Biology, Physics 90(1, Suppl.), S914-S915, 2014 (poster).

- U. Masood, M. Baumann, M. Bussmann, T. E. Cowan, W. Enghardt, T. Herrmannsdoerfer, <u>K. Hofmann</u>, M. C. Kaluza, L. Karsch, F. Kroll, U. Schramm, M. Schuerer, J. J. Wilkens, J. Pawelke: "Development of a Compact Particle Therapy Facility with Laser driven Ion Beams via Novel Pulse Powered Gantry Systems", in: Abstracts of the 53rd Annual Conference of the Particle Therapy Co-Operative Group (PTCOG), 8-14 June 2014, Shanghai/China, P204, p. 299, 2014 (poster).

Lebenslauf

KERSTIN MIRIAM HOFMANN
Geburtsdatum: 10.03.1986
Geburtsort: Aschaffenburg
Staatsangehörigkeit: deutsch

10/2011 - 07/2015	Technische Universität München *Doktorarbeit* am Klinikum rechts der Isar Vorraussichtliche Abgabe: Mai 2015
06/2012 - 05/2013	Technische Universität München Ausbildung zum *Medizinphysik-Experten* am Klinikum rechts der Isar Klinik für RadioOnkologie und Strahlentherapie
03/2010 - 03/2011	Universität Heidelberg *Diplomarbeit* am Deutschen Krebsforschungszentrum Titel: "Implementation of a dose delivery modality using dynamic multileaf collimation and its application for real-time tumor tracking"
02/2009 - 07/2009	Universität Valencia, Spanien Auslandssemester im Rahmen von ERASMUS
10/2005 - 03/2011	Universität Heidelberg *Diplom* in Physik Wahlfach: Medizinische Physik, Nebenfach: Physiologie
09/1996 - 06/2005	Friedrich-Dessauer-Gymnasium Aschaffenburg *Abitur* mit den Leistungskursen: Physik, Mathematik

Acknowledgements